AD-A198 829

Acoustic Bottom Reflectivity

Prepared by
Ole F. Hastrup

1 December 1986

Naval Underwater Systems Center
Newport, RI / New London, CT

SACLANT ASW Research Centre
La Spezia, Italy

DTIC
ELECTE
AUG 2 4 1988
S   D
H

88 8 19 059

TABLE OF CONTENTS

LIST OF ILLUSTRATIONS

LIST OF ILLUSTRATIONS (Cont'd)

LIST OF ILLUSTRATIONS (Cont'd)

LIST OF TABLES

CHAPTER 1

INTRODUCTION

The acoustic reflectivity from the sea floor is often an important factor for the performance of ASW systems in different environments, such as in deep water when using the bottom bounce paths, and in general for sound propagation in shallow water. Furthermore, it plays a role in the degradation of towed array operations due to reflected tow ship radiated noise and in certain weapon systems and with the frequency range of interest which spans over a large band from a few Hz to tenths of kHz. Therefore there is a need to be able to accurately measure the reflectivity or predict it from known or assumed geoacoustical data.

At several national naval research laboratories as well at the SACLANT ASW Research Center, La Spezia, work has been pursued in this field for more than 20 years making a significant improvement in our knowledge in this field. During this period, the experimental techniques have changed from the use of analog to digital acquisition, yielding higher resolution and accuracy, and the subsequent use of computers to analyze the data results in faster and more flexible ways of reporting. Furthermore, today we have a much better, though not complete, understanding and knowledge of the geoacoustical parameters for the bottom, including deeper layers.

The results from the SACLANTCEN activity has appeared in several published and unpublished reports and articles. [1],[2] However, to make this more accessible for potential users, it was felt worthwhile to update the material and issue some of it as a single report.

Special emphasis has been put into combining the theoretical results, with results obtained not from model tank experiments but from experiments in the real ocean environment where the action takes place. For this reason experimental and

digital analysis techniques are included in the report. Furthermore, due to the wide introduction of microcomputers, a set of algorithms for the IBM-PC computer family has been developed to enable the user to carry out "experiments" either in the office or on board to study the effect of the bottom layering on the reflectivity. Instructions for using these programmed algorithms are contained in appendix A.

It is hoped that this summary report will be useful especially for operators and scientists new to this field. However, it should be stressed that only the plane wave reflection coefficient will be considered in this report. For information concerning the complete wave solution, readers should look into new algorithms such as the Fast Field or SAFARI models.

This work has been sponsored by the Office of Naval Research and the Naval Underwater Systems Center and was done as a visiting scientist during an interesting and stimulating stay at the Naval Underwater Systems Center Code 10 in New London.

CHAPTER 2

GENERAL EQUATIONS

From the classical theory of elasticity, we know that a wave propagating through a homogeneous media is determined by the compressional wave potential and the shear wave potentials satisfying the following wave equations:

$$\nabla^2\phi = \frac{1}{\alpha^2}\frac{\partial^2\phi}{\partial t^2}$$

$$\nabla^2\psi_i = \frac{1}{\beta^2}\frac{\partial^2\psi_i}{\partial t^2} \qquad (2-1)$$

$$i = 1, 2, 3$$

with α as the compressional wave velocity and β as the shear wave velocity.

The displacement $\overline{U}$ which completely determines a plane wave is expressed as:

$$\overline{U} = \overline{\text{grad } \phi} + \overline{\text{curl } \overline{\psi}} \qquad (2-2)$$

Introducing an orthogonal coordinate system with the displacement u in the x direction and w in the z direction, equation (2) simplifies to:

$$u = \frac{\partial\phi}{\partial x} - \frac{\partial\phi}{\partial z}$$

$$w = \frac{\partial\phi}{\partial z} + \frac{\partial\phi}{\partial x} \qquad (2-3)$$

By the use of the two elastic constants (Lame'), the stresses can also be related to the potentials through u and w as:

$$\sigma_x = \lambda\left(\frac{\partial u}{\partial x} + \frac{\partial w}{\partial z}\right) + 2\mu\frac{\partial u}{\partial x}$$

$$\sigma_z = \lambda\left(\frac{\partial u}{\partial x} + \frac{\partial w}{\partial z}\right) + 2\mu\frac{\partial w}{\partial z} \qquad (2-4)$$

$$\tau_{xz} = \mu\left(\frac{\partial u}{\partial z} + \frac{\partial w}{\partial x}\right)$$

The relationship between the Lame' constants, density, and compressional and shear wave velocity is the following:

$$\alpha = \sqrt{\frac{\lambda + 2\mu}{\rho}} \quad \beta = \sqrt{\frac{\mu}{\rho}}$$

Analogous to the theory of electricity, we can introduce the concept of an impedance Z defined as the ratio between pressure and the normal component of the particle velocity:

$$Z = p/\dot{w} = -\sigma/\dot{w} \tag{2-5}$$

where p is the pressure, σ the normal stress, and w the particle velocity. The minus sign is due to the difference of defining pressure and stress.

In the case where the medium is a liquid, it cannot sustain shear which means that $\beta = 0$. This reduces equation (2-1) to:

$$\frac{\partial^2 \phi}{\partial x^2} + \frac{\partial^2 \phi}{\partial z^2} = \frac{1}{\alpha^2} \frac{\partial^2 \phi}{\partial t^2} \tag{2-6}$$

With the use of equations (2-1), (2-3) and (2-4), one obtains for σ:

$$\sigma = \rho \frac{\partial^2 \phi}{\partial t^2}$$

Using Bernoulli's method of assuming that the solution can be written as a product of functions, each depending only on one variable, we equate:

$$\phi(x, z, t) = F(x) \cdot G(z) \cdot T(t)$$

which, after differentiation with respect to x, z and t, gives:

$$\alpha^2 \left(\frac{F''}{F} + \frac{G''}{G} \right) = \frac{\ddot{T}}{T}$$

With T depending only on t and F, and G being independent of t, we have:

$$\frac{\ddot{T}}{T} = -\omega^2$$

The choice of sign for the separation constant is due to the requirement of periodic solutions in time. For the F and G functions, we can write:

$$\frac{F''}{F} + \frac{G''}{G} = -\frac{\omega^2}{\alpha^2}$$

and setting $\dfrac{F''}{F} = -h^2$

we have $\dfrac{G''}{G} = h^2 - \dfrac{\omega^2}{\alpha^2} = -\kappa^2$

which leads to solutions of the form:

$$F = e^{\pm ihx} \text{ and } G = e^{\pm i\kappa z}$$

Letting the waves propagate in the direction of the positive x-axis, the potential becomes:

$$\phi(x, z, t) = (Ae^{i\kappa z} + Be^{-i\kappa z}) \cdot e^{i(hx - \omega t)}$$

where the factor to A and B respectively corresponds to waves travelling in the positive and negative direction of the z-axis as seen on figure 2-1.
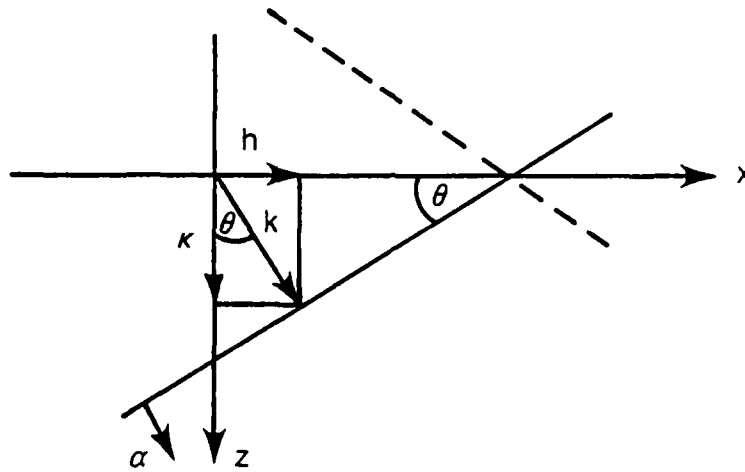
Figure 2-1. Wavefront Geometry

So we are dealing with plane waves propagating with the wavenumbers $k = \omega/\alpha$ normal to the wavefront, h in the x direction and κ in the z direction, satisfying the important condition $k^2 = h^2 + \kappa^2$.

From figure 2-1 we obtain the apparent horizontal velocity, which is the horizontal phase velocity $c = \omega/h = \alpha/\sin \theta$. When $\omega^2/\alpha^2 > h^2$, we see that the potential will not oscillate with respect to z but decay exponentially. These types of waves are called inhomogeneous waves and are frequently associated with boundary interaction as seen later.

CHAPTER 3

REFLECTION COEFFICIENT AND IMPEDANCE

Since the waves we are interested in are interacting with the sea floor and the layers below, the solutions to the wave equation must therefore satisfy certain boundary conditions depending on the nature of the boundary. The conditions are usually expressed directly in terms of stress and displacement.

For example, for two elastic media in welded contact, both stress and displacement must be continuous across the boundary. In the case of a liquid-solid or liquid-liquid interface, only the normal component of the stress and the displacement has to be continuous and the shear stress disappears. For a free and unloaded boundary, all stresses are zero.

On some occasions it is more advantageous to use velocity potentials instead of displacement potentials which can be done by multiplying the displacements by $i\omega$. The requirement of continuity of stress and displacement, therefore, can also be expressed in terms of stress and particle velocity or impedance as defined in equation (2-5).

The boundary which is of main interest is the interface between the water column and the sea floor. Let us now determine the reflection and transmission coefficients for a plane wave incident from the water as shown in figure 3-1. What the bottom looks like is of no concern at this moment and we will only treat it as a "black box."
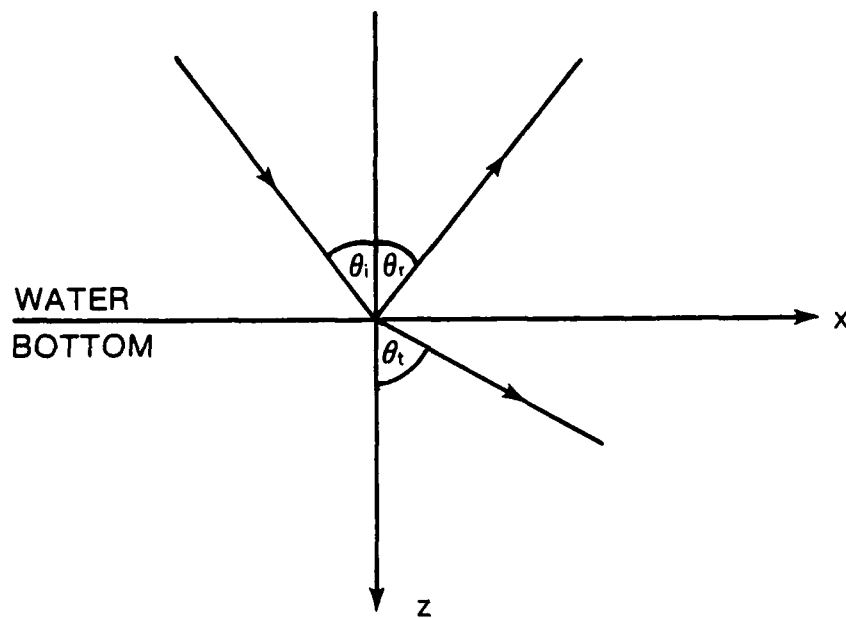
Figure 3-1. Plane Wave Reflection from the Bottom

From the Fermat principle (minimum travel time), we know that $\theta_i = \theta_r$ which means that:

$$\kappa_i = \kappa_r = \kappa \quad \text{and} \quad h_i = h_r = h$$

The total field in the water can then be written as:

$$\phi = \phi_i + R \cdot \phi_i = (e^{i\kappa z} + R \cdot e^{-i\kappa z}) \cdot e^{i(hx - \omega t)}$$

where R is the reflection coefficient.

Differentiating this with respect to t and z, the pressure p and the particle velocity are expressed as:

$$p = -\rho \, \frac{\partial^2 \phi}{\partial t^2} = \rho \omega^2 \phi = \rho \omega^2 \, (e^{i\kappa z} + R \cdot e^{-i\kappa z}) \cdot e^{i(hx - \omega t)}$$

$$\dot{w} = -i \, \omega \cdot \frac{\partial \phi}{\partial z} = \omega \kappa \, (e^{i\kappa z} - R \cdot e^{-i\kappa z}) \cdot e^{i(hx - \omega t)}$$

8

which at the boundary z = 0, reduces to:

$$p = \rho\omega^2 (1 + R) e^{i(hx - \omega t)}; \quad \dot{w} = \omega\kappa (1 - R) e^{i(hx - \omega t)}$$

Using the definition for the impedance and $h = k \cos\theta$ and $k = \omega/\alpha$, we end up with the following equation for the bottom impedance:

$$Z = \frac{\rho\alpha (1 + R)}{\cos\theta (1 - R)}$$

or for the reflection coefficient R:

$$R = \frac{Z - Z_0}{Z + Z_0}$$

with $Z_0 = \rho\alpha/\cos\theta$ being the impedance for the water.

In other words, if the bottom impedance is known, the reflection coefficient can be calculated from the above formula. However, as we will see later, the impedance often is a complicated function depending on both frequency and angle of incidence. This is the plane wave reflection coefficient which in optics is termed the Fresnel or Rayleigh coefficient.

Assuming now that the bottom can be treated as a liquid half-space (often a good assumption), the shear modulus $\mu = 0$. As a boundary condition, we will use the continuity of σ across the interface. The potential in the bottom, with T being the transmission coefficient, is:

$$\phi_t = T \cdot e^{i\kappa_t \cdot z} \cdot e^{i(hx - \omega t)}$$

Differentiating twice with respect to t, we obtain the stress in the bottom as:

$$\sigma_b = \rho_b \frac{\partial^2 \phi_t}{\partial t^2} = \omega^2 \rho_b T e^{i\kappa_b z} \cdot e^{i(hx - \omega t)}$$

giving:

$$T = \rho/\rho_b (1 + R)$$

9

or expressed as a function of impedance:

$$T = \frac{2 \cdot \rho Z}{\rho_b (Z + Z_0)}$$

By knowing the impedance Z at the boundary it is straightforward to calculate both the reflection and transmission coefficients. Whereas to get the angle of the transmitted wave, information of the bottom itself is required.

Now let us consider some simple examples looking at the bottom reflection characteristics for different situations.

CHAPTER 4

THE HALF-SPACE BOTTOM

In the ocean, the bottom often consists of soft unconsolidated sediments which acoustically can be considered liquid due to the very low shear modulus. We will therefore study this case in more detail. Figure 4-1 illustrates our simple model where water has a density of ρ and a velocity of α and the bottom has a density of ρ_1 and a compressional velocity of α_1. The angle of incidence in the water is θ and the angle of the transmitted wave in the bottom is θ_1.

$$\alpha \qquad \rho$$

///////////////////////

$$\alpha_1 \qquad \rho_1$$
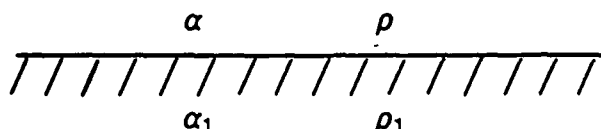
Figure 4-1. Simple Bottom Model

Given that the horizontal phase velocity c along the interface must be the same in the water and in the bottom, we get from figure 2-1:

$$c = \alpha/\sin\theta = \alpha_1/\sin\theta_1$$

or

$$\alpha/\alpha_1 = \sin\theta/\sin\theta_1$$

which is the Snell's refraction law.

Using the potential for the transmitted wave and equation (2-5), the impedance Z_1 for the bottom, with $\alpha_1/\cos\theta_1$ as the vertical phase velocity, becomes:

$$Z_1 = \frac{\alpha_1 \cdot \rho_1}{\cos\theta_1}$$

The reflection coefficient expressed by density, wave velocity, and angle of incidence becomes:

$$R = \frac{\rho_1\,\alpha_1\,\cos\theta - \rho\,\alpha\,\cos\theta_1}{\rho_1\,\alpha_1\,\cos\theta + \rho\,\alpha\,\cos\theta_1}$$

which with Snell's Law reduces to the classical reflection coefficient:

$$R = \frac{a \cdot \cos\theta - \sqrt{n^2 - \sin^2\theta}}{a \cdot \cos\theta + \sqrt{n^2 - \sin^2\theta}} \qquad (4-1)$$

where $a = \rho_1/\rho$ is the density contrast and $n = \alpha/\alpha_1$ the refractive index.

When studying the reflection coefficient at angles close to grazing, the following simplified expression can be obtained by using the grazing angle $\varepsilon = 90 - \theta$ instead of the angle of incidence:

$$R = \frac{a \cdot \sin\varepsilon - \sqrt{n^2 - \cos^2\varepsilon}}{a \cdot \sin\varepsilon + \sqrt{n^2 - \cos^2\varepsilon}}$$

For small grazing angles with $\sin\varepsilon \approx \varepsilon$ and $\cos\varepsilon \approx 1$, the following can be obtained:

$$R = -\frac{\dfrac{a}{\sqrt{n^2 - 1}} \cdot \varepsilon - 1}{\dfrac{a}{\sqrt{n^2 - 1}} \cdot \varepsilon + 1} \approx -\left(1 - \frac{2 \cdot a}{\sqrt{n^2 - 1}} \cdot \varepsilon + \cdots\right)$$

Using the Taylor expression for the exponential function

$$e^x \approx 1 + x + \cdot$$

the reflection coefficient near grazing can be written as:

$$R \approx -e^{-\frac{2 \cdot a}{\sqrt{n^2 - 1}} \cdot \varepsilon}$$

This expression will be used later to look at reflection loss anomalies near grazing.

The form of the reflection coefficient depends on the ratios of a and n. We will consider three cases corresponding to values observed in the real world: the intromission angle, the critical angle, and no critical or intromission angle. Appendices B and C contain discussions of the values for the bottom geoacoustical

parameters observed in the sea floor environment. However, in some of the following examples, extreme values for these parameters have been used in order to emphasize their relative importance on the reflection coefficient.

INTROMISSION ANGLE CASE: $1 < n < a$

This is the most common case with the top bottom layer consisting of unconsolidated sediments as has been observed during a large number of experiments.

The argument of the square root $n^2 - \sin^2 \theta$ is always positive. The coefficient remains real for all angles and is zero for:

$$a \cdot \cos \theta = \sqrt{n^2 - \sin^2 \theta}$$

or

$$\sin \theta_B = \sqrt{\frac{a^2 - n^2}{a^2 - 1}}$$

This angle θ_B is called the intromission angle or, in optics, the Brewster angle. In optics, at this angle, the reflected and the transmitted waves are perpendicular to each other; however, in acoustics this is not the case due to the density effect. In nature where some attenuation is always present, the reflection coefficient will not be zero but finite (as will be discussed later). The phase shift will be zero for angles steeper than the intromission angle and 180° for more grazing angles, meaning that a reflected signal will be inverted.

To show the behavior of the reflection coefficient curve, we will use results obtained from bottom cores taken in the deep Mediterranean Naples Abyssal Plain. The averages and standard deviations for the upper 50 cm have been computed as:

relative compressional velocity $\alpha_1 = 0.977 \pm 0.004$

relative density $\rho_1 = 1.39 \pm 0.04$

the bottom and the density of the bottom water. The reason for using relative values, as we will be doing for the rest of the report, is that they are independent of seasonal changes in the water column.

Also instead of the reflection coefficient, we will use the reflection loss in dB defined as -20 Log (R). The reason is that we will need the losses in dB for the sonar equation.

Figure 4-2 illustrates the loss curve corresponding to the above data and the actual measured losses from the water/sediment interface. One will notice excellent agreement except around the intromission angle where the effect of attenuation is noticeable.
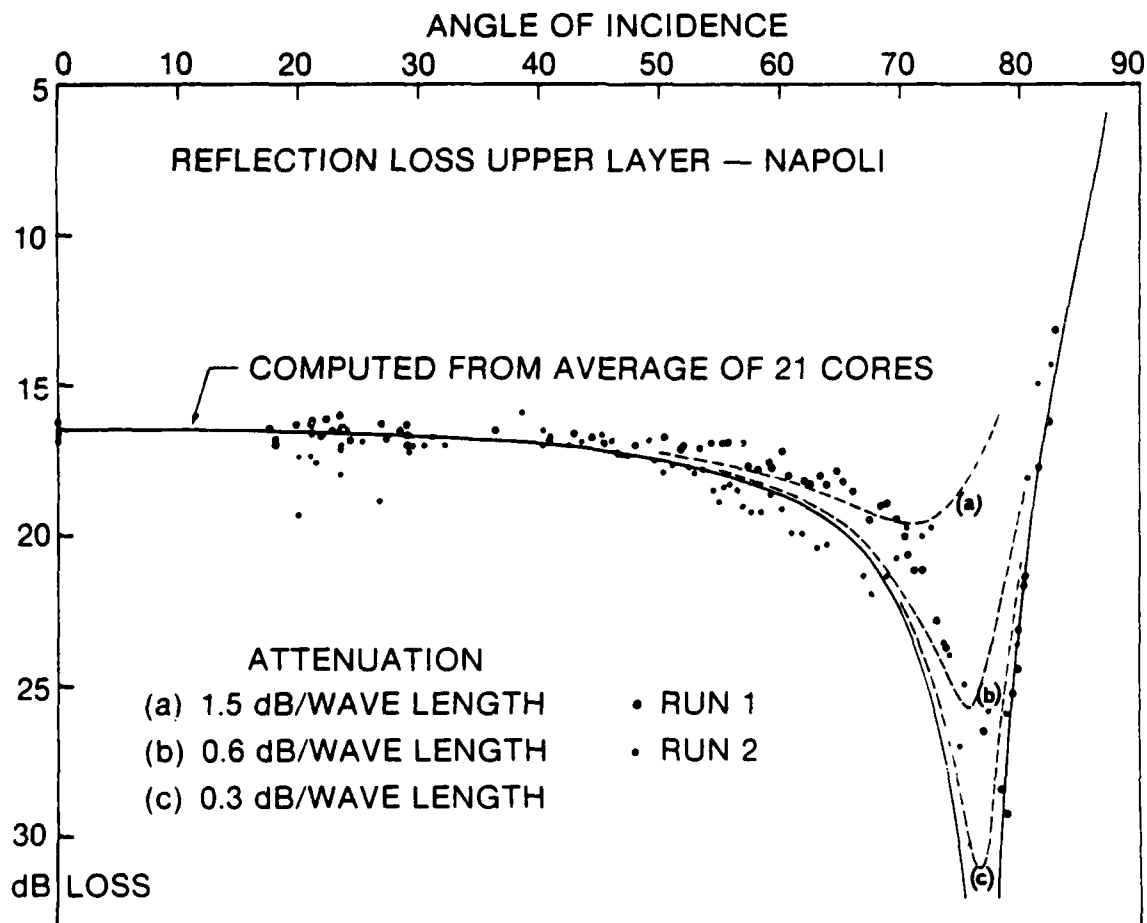
Figure 4-2. Reflection Loss (Intromission Angle Case)

CRITICAL ANGLE CASE: n < 1, n < m

This case of having a higher wave velocity in the bottom than in the water is usually found when the bottom is composed of coarser sediments such as sand.

Using equation (4-1), for angles of incidence larger than arcsin (n), the reflection coefficient R becomes complex with a magnitude of one and can be written as $R = e^{i\phi}$ where ϕ is the phase shift (not to be confused with the ϕ previously used for potentials). This angle is called the critical angle θ_{cr}. For angles more grazing, the reflection becomes total with all the incident energy being reflected and with the presence of an inhomogeneous wave travelling in the bottom along the interface. The phase shift is expressed as:

$$\phi = -2 \arctan \left(\frac{\sqrt{\sin^2 \theta - n^2}}{a \cos \theta} \right)$$

The phase shift is zero for angles of incidence less than θ_{cr} and increases monotonic to 180° at grazing. The sign of the phase shift is determined from the direction of the z-axis.

Figure 4-3 illustrates the reflection loss for a sandy bottom with the relative wave velocity $a = 1.13$ and the relative density $\rho = 2.0$. The loss curves for taking attenuation into account will be discussed in the next chapter.

NO CRITICAL OR INTROMISSION ANGLE CASE: 1 < n, a < n

This is a rare situation which has been included for completeness and can occur in the case where the bottom contains gas bubbles, such as methane caused by decomposition of organic matter in the bottom. This is normally observed in lakes or bays and possibly could be more common in the future as a result of pollution.
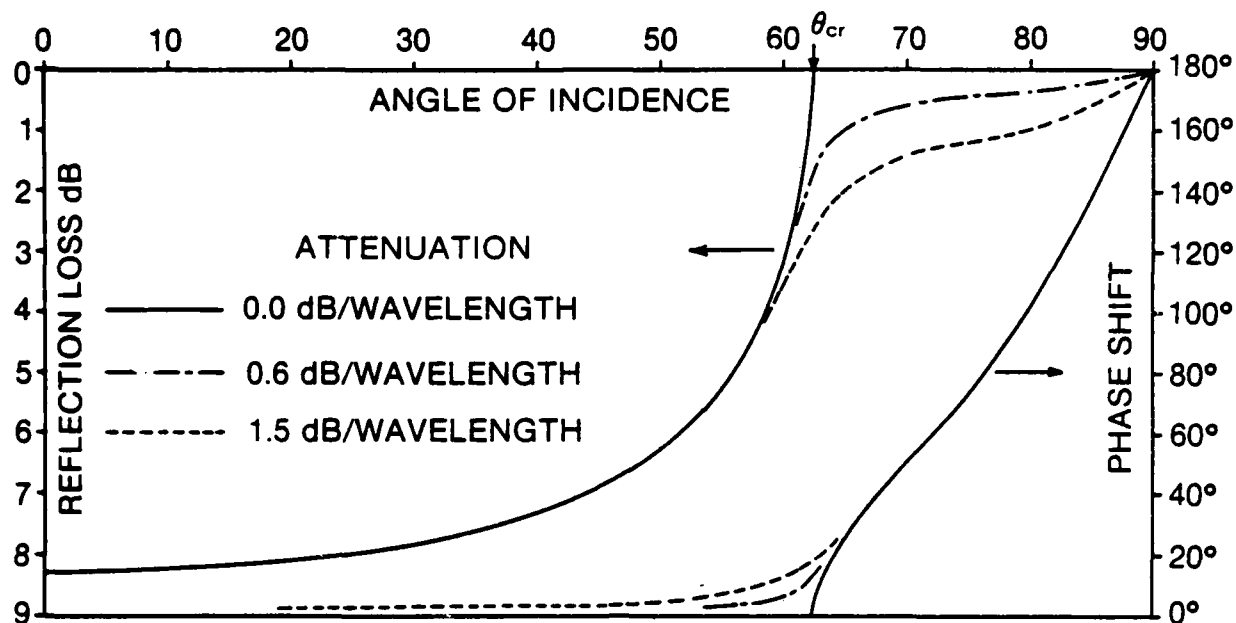
Figure 4-3. Reflection Loss (Critical Angle Case)

The presence of gas bubbles has little effect on density but a dramatic effect on wave velocity through a strong increase in the compressibility of the sediments.   To understand this, let us look at a unit volume of bottom material as seen in figure 4-4.
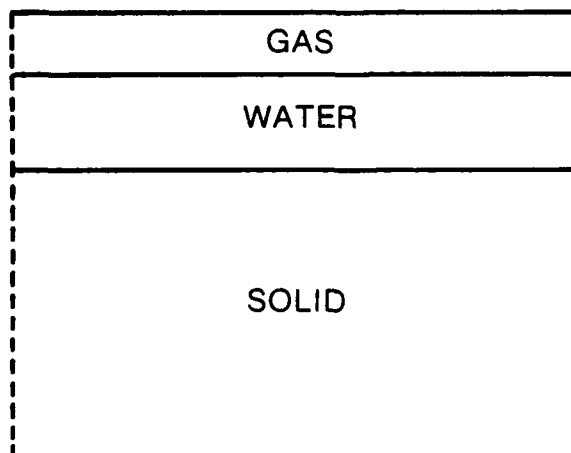
Figure 4-4. Sediment Unit Volume

We will assume that the bottom is composed of a mixture of non-resonant adiabatic-behaving gas bubbles, water, and solids. We will also assume that we can treat such a sediment as an ideal three-component mixture and that the equations for elastic waves are valid.

We will now introduce the concept of porosity, defined as the ratio between the volume of the voids and the total volume of the sediment. The volume of gases, water and solids are represented in the following ratios as g, x and y with $g + x + y = 1$. The porosity n then becomes $n = g + x$.

If the density of the solid particulate matter in the sediment is constant, then from the definition of porosity, the bulk sediment density is given by:

$$\rho_{sed} = \rho_g \cdot g + \rho_w \cdot (n - g) + (1 - n) \cdot \rho_s$$

where the indices g, w and s respectively refer to gas, water and solid.

The sound velocity for a liquid is given by

$$\alpha = \sqrt{\frac{1}{\rho \cdot B}}$$

where B is the compressibility. We assume that B can be expressed as the sum of the three component moduli, so in terms of porosity we get:

$$B_{sed} = B_g \cdot g + B_w \cdot (n - g) + (1 - n) \cdot B_s$$

and for the wave velocity

$$\alpha = \sqrt{\frac{1}{[\rho_g \cdot g + \rho_w \cdot (n - g) + (1 - n) \cdot \rho_s] \cdot [B_g \cdot g + B_w \cdot (n - g) + (1 - n) \cdot B_s]}}$$

which is the so-called Woods equation for a three-component mixture. The validity of the above assumptions has been verified through many experiments and in a later chapter we will use the porosity as an independent parameter to parameterize the wave velocity and sediment density.

Figure 4-5 illustrates an example of the relative wave velocity as a function of gas content for a 70/80 percent porosity sediment and a methane-nitrogen mixture, showing the very marked effect for even small quantities of free gas bubbles.
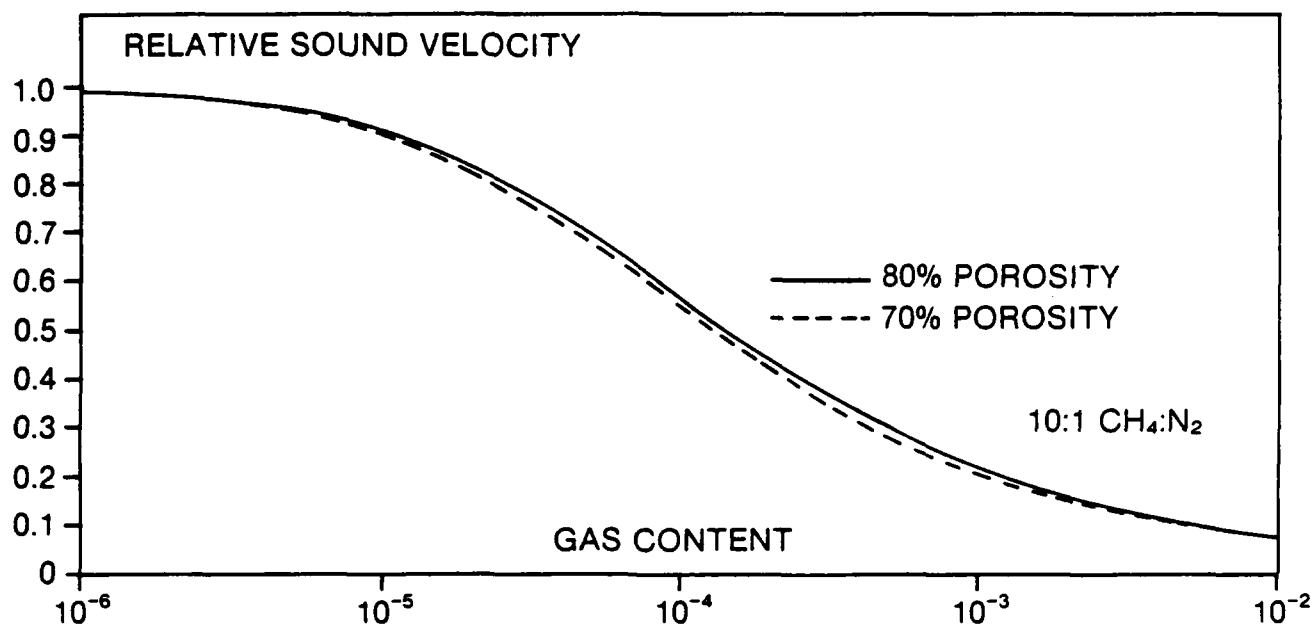
Figure 4-5. Wave Velocity as Function of Gas Content

Now assuming that n >> sin θ, equation (4-1) can be reduced to the simple expression:

$$R = \frac{z_1/z \cdot \cos \theta - 1}{z_1/z \cdot \cos \theta + 1}$$

showing that R only depends on the impedance ratio and the angle of incidence with a 180° phase shift for all angles.

Figure 4-6 plots the reflection loss for a relative density $\rho = 1.3$ and a relative wave velocity $\alpha = 0.2$ equal to a gas content 0.001. Also on the same plot are shown reflection losses measured in a lake near the SACLANTCEN where the bottom contained a high concentration of free methane of which some was released for each shoot fired during the experiment. The reflected pulses received were all inverted due to the 180° phase shift from this almost perfect pressure release interface.
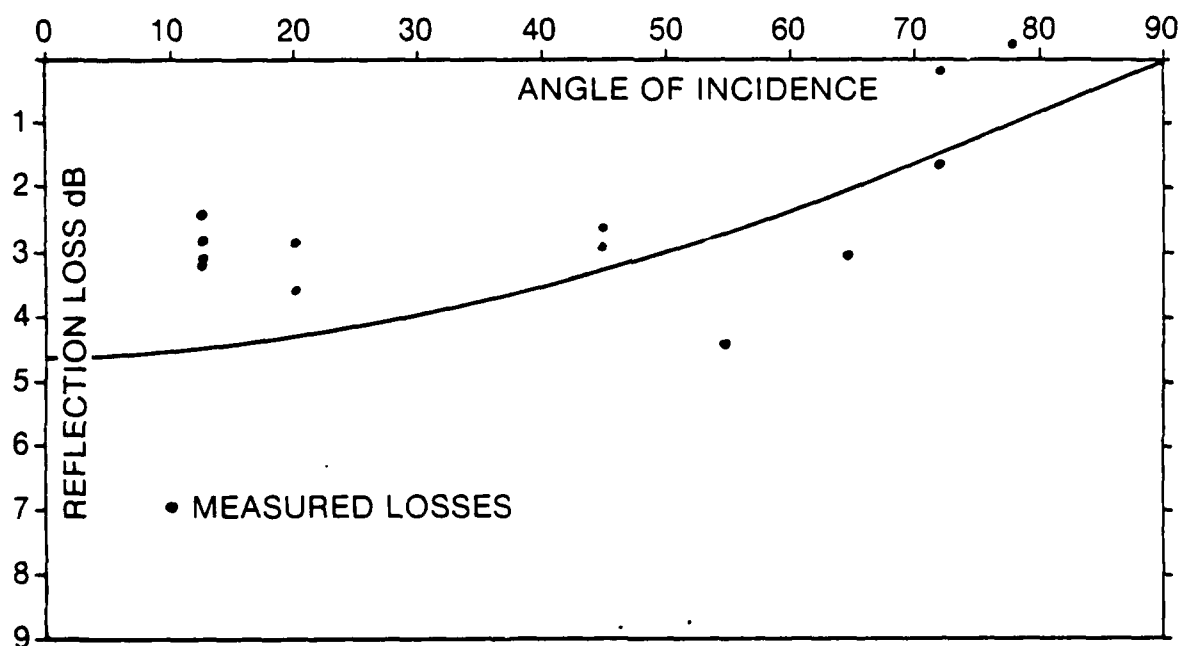
Figure 4-6. Calculated and Measured Reflection Losses
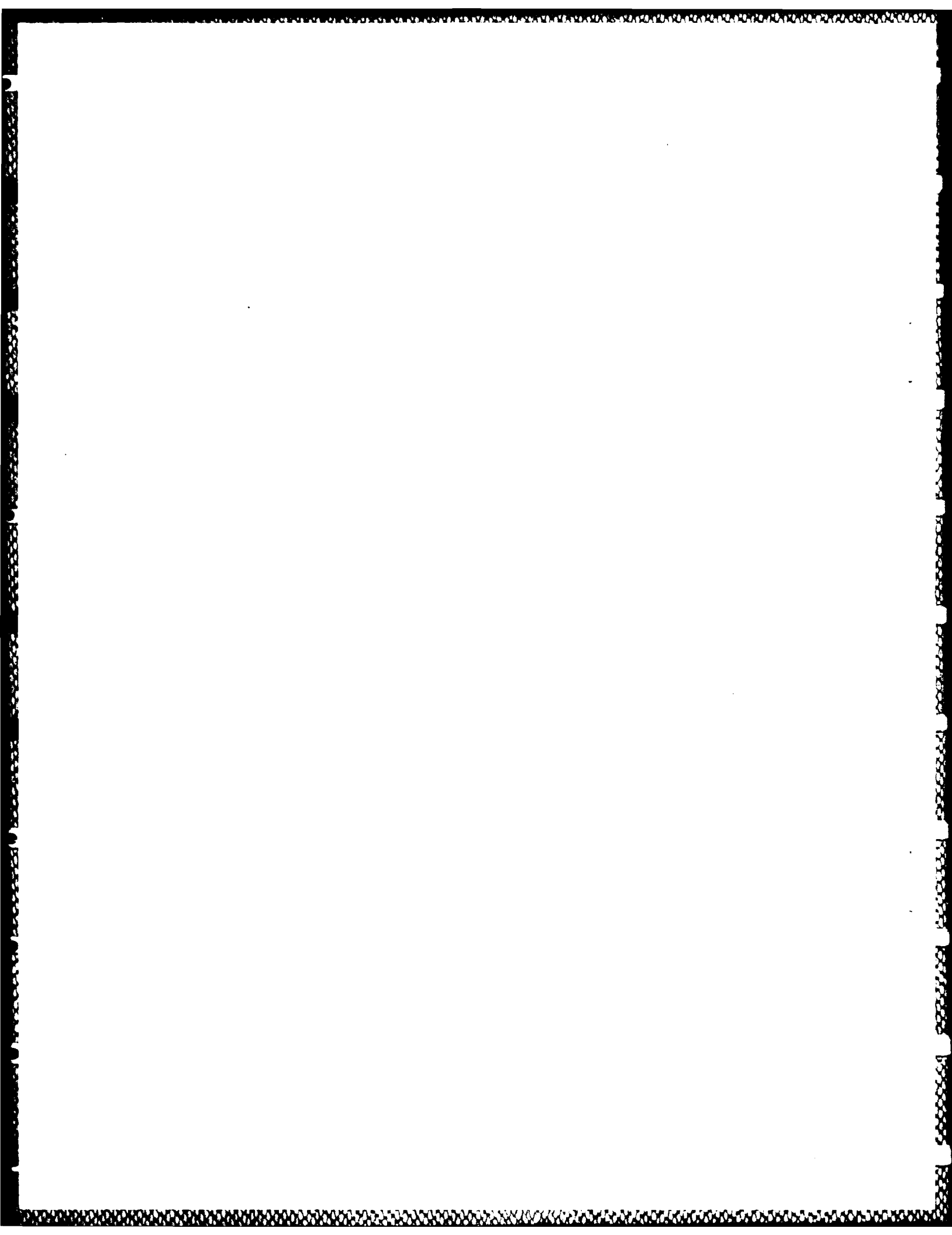
CHAPTER 5

ATTENUATION

Until now we have ignored attenuation in our calculations of the reflection coefficient, an idealization which is not always permissible. Real-bottom materials absorb energy; this results in a smoothing of the reflection coefficient curves, especially near the critical or the intromission angle. In this report, we will not deal with the actual attenuation mechanisms or processes but will introduce attenuation through complex wavenumbers and wave velocities. Looking at the propagation of a wave with a complex wave velocity $\alpha = \alpha \cdot (1 - i\nu)$, we have for the wavenumber $\cdot$ $k = k' = \omega/\alpha (1 - i\nu) \approx k \cdot (1 + i\nu)$)

$$e^{ikx} = e^{ik (1 + i\nu)x} = e^{-\nu kx} \cdot e^{ikx}$$

where the first factor represents the attenuation. The imaginary part of is a function of frequency and through this report we will consider a linear dependence, which corresponds to a constant attenuation δ in dB per wavelength λ. Thus, with $\lambda = \dfrac{2\pi}{k}$, we get:

$$\delta = 20 \cdot \log e^{-k\nu\lambda} = 20 \cdot \log e^{2\pi\nu}$$

and: $\quad \alpha = \alpha (1 - i\, 0.0183\, \delta)$

which can be used in the different expressions for the reflection coefficient.

With the presence of attenuation, it can be shown that neither total reflection nor total transmission exists except at grazing. The analytical calculations for the reflection coefficient are quite lengthy and the effect is perhaps better illustrated by using our previous examples. Figures 4-2 and 4-3 illustrated the reflection losses for varying degrees of attenuation. The smoothing effect of the attenuation is clearly seen near critical and intromission angles.

What happens if the attenuation is very large? Is the reflection coefficient then going to be very small? In such a case, we have $\nu \gg 1$ and $n n^2 = k_i^2/k^2 = n'^2 (1 + i\nu)^2 = n'^2 (1 + 2i\nu - \nu^2)$. Inserting this into equation (4-1) and dividing both nominator and denominator by ν, we obtain:

$$R = \frac{\dfrac{a \cos \theta}{\nu} - \sqrt{n'^2 (1/\nu^2 - 1 + 2i/\nu) - \sin^2 \theta/\nu}}{\dfrac{a \cos \theta}{\nu} + \sqrt{n'^2 (1/\nu^2 - 1 + 2i/\nu) - \sin^2 \theta/\nu}}$$

which for $\nu \to \infty$ gives $R = -1$.

In other words the reflection is total with a 180° phase shift, when the attenuation is high in the bottom. In optics, the analog is the reflection of light from a metallic surface, the mirror--but who notices in the morning that you are phase-shifted 180°.

CHAPTER 6

GENERAL LAYERING

So far we have only looked at the most simple bottom model, the liquid half-space. When inspecting core samples taken from the ocean floor, a large majority of them show a marked layering, very often alternating between harder and softer sediments. In this chapter we will therefore study the reflectivity from the most general type of ocean bottom, one consisting of several parallel sediment layers, each supporting both compressional and shear waves and including attenuation of both wave types.

Figure 6-1 illustrates our model for calculating the reflection coefficient for a plane wave incident from a fluid half-space onto a semi-infinite medium consisting of n parallel homogeneous and isotropic layers on top of a half-space.
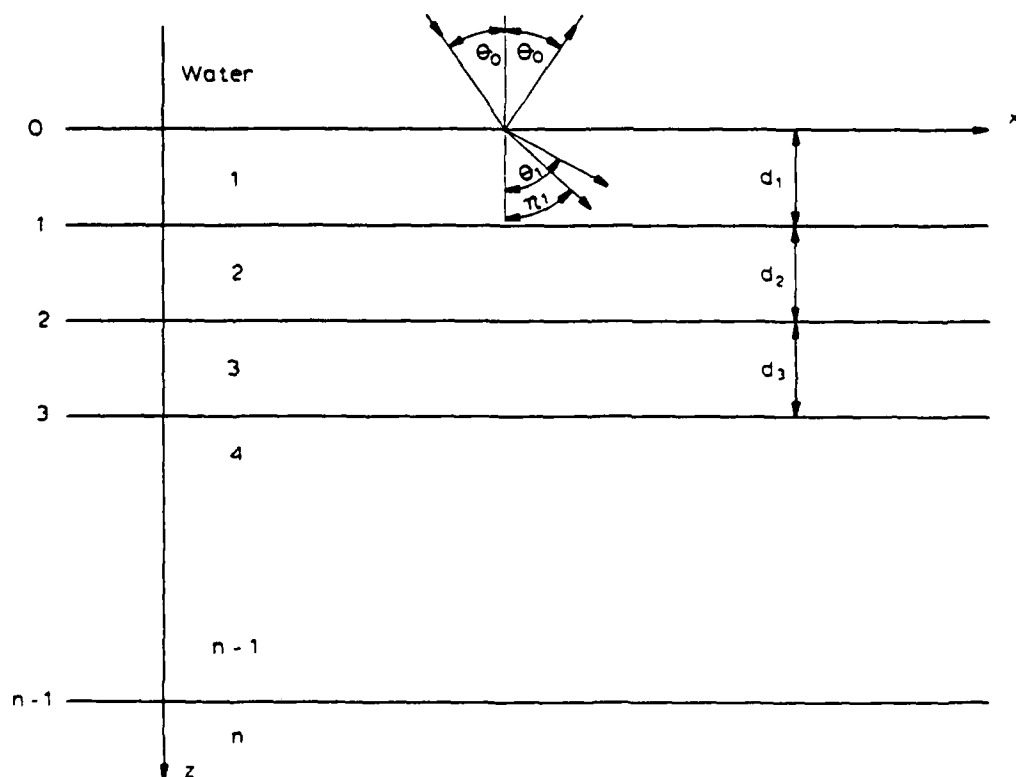
Figure 6-1. Layer Geometry

For a wave with the angle of incidence θ in the fluid half-space, the two angles in the mth layer corresponding to compressional and shear waves will be determined by Snell's Law in the following way:

$$\frac{\alpha_0}{\sin \theta_0} = \frac{\alpha_m}{\sin \theta_m} = \frac{\beta_m}{\sin \eta_m} = c \tag{6-1}$$

where c is the horizontal phase velocity.

From the relationship between wavenumber and velocity,

$$\omega = k_0 \, \alpha_0 = k_m \, \alpha_m = \kappa_m \, \beta_m$$

equation (6-1) can also be written as follows:

$$k_0 \sin \theta_0 = k_m \sin \theta_m = \kappa_m \sin \eta_m = h$$

where $h = \omega/c$ is the horizontal wavenumber, and k and κ are the normal wavenumbers in the mth layer for the compressional and shear waves.

In this case we will need the potentials for both the compressional and shear waves. Using the form $g(z) \cdot e^{i(hx - \omega t)}$ for the potentials and inserting it into the wave equations from chapter 2, a solution for the mth layer can be written as:

$$\phi_m = [A_m \, e^{-ik_m \cos \theta_m z} + B_m \, e^{ik_m \cos \theta_m z}] \, e^{i(hx - \omega t)}$$

$$\psi_m = [C_m \, e^{-i\kappa_m \cos \eta_m z} + D_m \, e^{i\kappa_m \cos \eta_m z}] \, e^{i(hx - \omega t)}$$

The four constants are to be determined from the boundary conditions, which are continuity in stress and displacement, or more conveniently as continuity in particle velocity. By differentiating equation (2-3) with respect to time and combining this result and equation (2-4) with the expressions for the two potentials above, we get the following matrix form in which the quantities of interest are expressed by the four constants A_m, B_m, C_m and D_m.

$$
\begin{bmatrix} \dot{u}/c \\ \dot{w}/c \\ \sigma \\ \tau \end{bmatrix} = \begin{bmatrix} t_{11} & t_{12} & t_{13} & t_{14} \\ t_{21} & t_{22} & t_{23} & t_{24} \\ t_{31} & t_{32} & t_{33} & t_{34} \\ t_{41} & t_{42} & t_{43} & t_{44} \end{bmatrix} \begin{bmatrix} A_m + B_m \\ A_m - B_m \\ C_m - D_m \\ C_m + D_m \end{bmatrix}
$$

or, using the more convenient matrix notation,

$$
\overline{S} = \overline{\overline{T}}[z]\overline{P}
$$

Omitting the common factor $e^{i(hx - \omega t)}$, the elements in $\overline{\overline{T}}$ are:

$$
t_{11} = -(\alpha_m/c)^2 \cos a_m h \cdot z
$$

$$
t_{12} = i(\alpha_m/c)^2 \sin a_m h \cdot z
$$

$$
t_{13} = -\gamma_m b_m \cos b_m h \cdot z
$$

$$
t_{14} = i \gamma_m b_m \sin b_m h \cdot z
$$

$$
t_{21} = i(\alpha_m/c)^2 a_m \sin a_m h \cdot z
$$

$$
t_{22} = -(\alpha_m/c)^2 a_m \cos a_m h \cdot z
$$

$$
t_{23} = i\gamma_m \sin b_m h \cdot z
$$

$$
t_{24} = \gamma_m \cos b_m h \cdot z
$$

$$
t_{31} = -\rho_m \alpha_m^2 (\gamma_m - 1) \cos a_m h \cdot z
$$

$$
t_{32} = i\rho_m \alpha_m^2 (\gamma_m - 1) \sin a_m h \cdot z
$$

$$
t_{33} = -\rho_m c^2 \gamma_m^2 b_m \cos b_m h \cdot z
$$

$$
t_{34} = i\rho_m c^2 \gamma_m^2 b_m \sin b_m h \cdot z
$$

$$
t_{41} = -i \rho_m \alpha_m^2 \gamma_m a_m \sin a_m h \cdot z
$$

$$
t_{42} = \rho_m \alpha_m^2 \gamma_m a_m \cos a_m h \cdot z
$$

$$t_{43} = i \, \rho_m \, c^2 \, \gamma_m \, (\gamma_m - 1) \, \sin b_m \, h \cdot z$$

$$t_{44} = -\rho_m \, c^2 \, \gamma_m \, (\gamma_m - 1) \, \cos b_m \, h \cdot z$$

where $a_m = \cot \theta_m$ and $b_m = \cot \eta_m$

and $\gamma_m = 2 \cdot (\beta_m/c)^2$

So for a system of n layers, we get $4 \cdot n$ equations plus one for the water-column and two for the limiting half-space, to determine the $4 \cdot n + 3$ unknown constants. Since we are mainly interested in the calculation of the reflection coefficient, we will not try to solve the equations directly, but use a method based on transfer matrices due to W.T. Thompson and later modified by N.A. Haskell.[3],[4]

Placing the origin of the z-axis at the $(m - 1)^{th}$ interface, we get for $z = 0$ and $z = d_m$

$$\overline{S}_{m-1} = \overline{\overline{T}}_m \, [0] \cdot \overline{P}_m$$

and   (6-2)

$$\overline{S}_m = \overline{\overline{T}}_m \, [d_m] \cdot \overline{P}_m$$

where d_m is the thickness of the layer and in which indices for $\overline{S}$ refer to the interface and indices for $\overline{\overline{T}}$ and $\overline{P}$ refer to the layer.

By eliminating $\overline{P}_m$ from the two equations, we get a relation between the value of velocity and stress at the top and bottom of the mth layer:

                                                                                     (6-3)

$$\overline{S}_m = \overline{\overline{T}}_m \, [d_m] \cdot \overline{\overline{T}} \, [0]^{-1} \cdot \overline{S}_{m-1}$$

or

$$\overline{S}_m = \overline{\overline{A}}_m \cdot \overline{S}_{m-1}$$

The elements of $\overline{\overline{A}}_n$ can be found after some simple but quite lengthy calculations.

$$A_{11} = \gamma_n \cos P_n - (\gamma_n - 1) \cos Q_n$$

$$A_{12} = i[(\gamma_n - 1) \sin P_n/a_n + \gamma_n b_n \sin Q_n]$$

$$A_{13} = -(\cos P_n - \cos Q_n)/\rho_n c^2$$

$$A_{14} = i(\sin P_n/a_n + b_n \sin Q_n)/\rho_n c^2$$

$$A_{21} = -i[\gamma_n a_n \sin P_n + (\gamma_n - 1) \sin Q_n/b_n]$$

$$A_{22} = -(\gamma_n - 1) \cos P_n + \gamma_n \cos Q_n$$

$$A_{23} = i(a_n \sin P_n + \sin Q_n/b_n)/\rho_n c^2$$

$$A_{24} = A_{13}$$

$$A_{31} = \rho_n c^2 \gamma_n (\gamma_n - 1) (\cos P_n - \cos Q_n)$$

$$A_{32} = i\rho_n c^2 [(\gamma_n - 1)^2 \sin P_n/a_n + \gamma_n^2 b_n \sin Q_n]$$

$$A_{33} = A_{22}, \quad A_{34} = A_{12}$$

$$A_{41} = i \rho_n c^2 [\gamma_n^2 a_n \sin P_n + (\gamma_n - 1)^2 \sin Q_n/b_n]$$

$$A_{42} = A_{31}$$

$$A_{43} = A_{21}$$

$$A_{44} = A_{11}$$

where

$$a_n = \cot \theta_n, \quad b_n = \cot \eta_n, \quad \gamma_n = 2(\beta_n/c)^2,$$

$$P_n = a_n \cdot h \cdot d_n \text{ and } Q_n = b_n \cdot h \cdot d_n$$

The elements V_{ij} of the half-space matrix $\overline{\overline{T}}[0]^{-1}$ are:

$$V_{11} = -2(\beta_m/\alpha_m)^2$$

$$V_{13} = (\rho_m \alpha_m^2)^{-1}$$

$$V_{22} = c^2 \, (\gamma_m - 1)/\alpha_m^2 \, a_m$$

$$V_{24} = (\, \rho_m \, \alpha_m^2 \, a_m)^{-1}$$

$$V_{31} = (\, \rho_m - 1)/\gamma_m \cdot b_m$$

$$V_{33} = -(\, \rho_m \, c^2 \, \gamma_m \, b_m)^{-1}$$

$$V_{42} = 1$$

$$V_{44} = (\, \rho_m \, c^2 \, \gamma_m)^{-1}$$

$$V_{12} = V_{14} = V_{21} = V_{23} = V_{32} = V_{34} = V_{41} = V_{43} = 0$$

To take the attenuation in the layer into account, we will use complex wavenumbers as before. Ignoring the attenuation in the water means that both k, h and c are real, but from Snell's Law we see that the wavenumber, velocities and angles of incidence will be complex in a layer with attenuation, which again means that the elements in $\overline{\overline{A}}$ are complex.

From the conditions of continuity and successive use of equation (6-3)

$$\overline{S}_{n-1} = \overline{\overline{A}}_{n-1} \cdot \overline{\overline{A}}_{n-2} \ldots \overline{\overline{A}}_0 \cdot \overline{S}_0$$

and from equation (6-2)

$$\overline{P}_n = \overline{\overline{T}}_n \, [0]^{-1} \cdot \overline{\overline{A}}_{n-1} \cdot \overline{\overline{A}}_{n-2} \ldots \overline{\overline{A}}_0 \cdot \overline{S}_0 \qquad (6-4)$$

where $\overline{P}_n$ represents the potential in the lower half-space, $\overline{\overline{T}}[0]^{-1}$ the acoustic properties of the half-space, $\overline{\overline{A}}_{n-1} \ldots \overline{\overline{A}}_0$ the acoustic properties of the layering, and $\overline{S}_0$ the upper boundary condition. In the two half-spaces 0 and n, certain conditions have to be met. No shear stresses or shear waves can exist in the fluid, which means that

$$\tau = C_0 = D_0 = 0$$

For the solid half-space to ensure a limited potential for $Z \rightarrow + \infty$,

$$B_n = D_n = 0$$

Inserting the above-given values into equation (6-4)

$$
\begin{bmatrix} A_n \\ A_n \\ C_n \\ C_n \end{bmatrix} = \begin{bmatrix} h_{11} & h_{12} & h_{13} & h_{14} \\ h_{21} & h_{22} & h_{23} & h_{24} \\ h_{31} & h_{32} & h_{33} & h_{34} \\ h_{41} & h_{42} & h_{43} & h_{44} \end{bmatrix} \begin{bmatrix} \dot{u}/c \\ \dot{w}/c \\ \sigma \\ 0 \end{bmatrix}
$$

where the matrix $\overline{\overline{H}} = \overline{\overline{T}}_n [0]^{-1} \cdot \overline{\overline{A}}_{n-1} \ldots \overline{\overline{A}}_0$.

Eliminating A_n , C_n and $\dot{u}/c$ gives:

$$
\dot{w}/c = -\frac{(h_{13} - h_{23})(h_{31} - h_{41}) - (h_{33} - h_{43})(h_{11} - h_{21})}{(h_{12} - h_{22})(h_{31} - h_{41}) - (h_{11} - h_{21})(h_{32} - h_{42})} \, \sigma
$$

or from the definition of the bottom impedance as $-\sigma/\dot{w}$, we get:

$$
Z_b = \frac{(h_{12} - h_{22})(h_{31} - h_{41}) - (h_{11} - h_{21})(h_{32} - h_{42})}{c \cdot (h_{13} - h_{23})(h_{31} - h_{41}) - (h_{33} - h_{43})(h_{11} - h_{21})}
$$

and for the reflection coefficient

$$
R = \frac{Z_b - Z}{Z_b + Z}
$$

where Z is the water impedance.

Because of the complexity of the equations, they are not well suited for an analytical study except for some simple cases, which will be presented in the following chapters. For a more general purpose, the above equations have been programmed for an IBM - XT in Microsoft FORTRAN as described in appendix A.

CHAPTER 7

SOLID HALF-SPACE

With only the half-space and no layers present, $n = 1$ and the H matrix becomes $\overline{\overline{H}} = \overline{\overline{T}}[0]^{-1}$. Inserting the values for $t_{i,j}$, we get for the bottom impedance:

$$Z_b = \frac{\dfrac{c^2 (\gamma_1 - 1)^2}{a_1^2 \gamma_1 \, a_1 \, b_1} + 2 \; \dfrac{(\beta_1/\alpha_1)^2}{}}{- \dfrac{(\gamma_1 - 1) \cdot c}{\rho_1 \, \alpha^2 \, \gamma_1 \, b_1} + 2 \dfrac{(\beta_1/\alpha_1)^2}{\rho_1 \, c \, \gamma_1 \, b_1}}$$

which is not a convenient expression for analytically studying the reflection coefficient. Using the different relations between the angles θ and η and c, the bottom impedance as shown by Brekhovskikh [5] becomes:

$$Z_b = \frac{\rho_1 \, \alpha_1}{\cos \theta_1} \cdot \cos^2 2\eta_1 + \frac{\rho_1 \, \beta_1}{\cos \eta_1} \cdot \sin^2 2\eta_1$$

Using Snell's Law with the relative wave velocities, we have:

$$\frac{\sin \theta}{1} = \frac{\sin \theta_1}{\alpha_1} = \frac{\sin \eta_1}{\beta_1}$$

showing the possibility for two critical angles determined by

$$\theta_{\alpha cr} = \text{Arc sin } (1/\alpha_1)$$

$$\theta_{\beta cr} = \text{Arc sin } (1/\beta_1)$$

respectively for compressional and shear waves.

In the following, we will study three different cases depending on the values of α_1 and β_1 :

a) $\alpha_1 > 1 > \beta_1$ One critical angle

b) $\alpha_1 > \beta_1 > 1$ Two critical angles

c) $\alpha_1 > \beta_1 > 1.09$ Rayleigh interface waves

ONE CRITICAL ANGLE $\alpha_1 > 1 > \beta_1$

This is the most common case when we are dealing with a bottom consisting of consolidated sediments as often found in shallow water. Figure 7-1 illustrates the loss and phase shift when $\alpha_1 = 1.13$, $\beta_1 = 0.4$ and $\rho_1 = 2.0$. Two values for the attenuation are used, 0 and $1 \, dB/\lambda$. The values for no shear are also shown for comparison. Clearly, the presence of shear waves "softens" the bottom, due to energy being carried away from the interface by them.
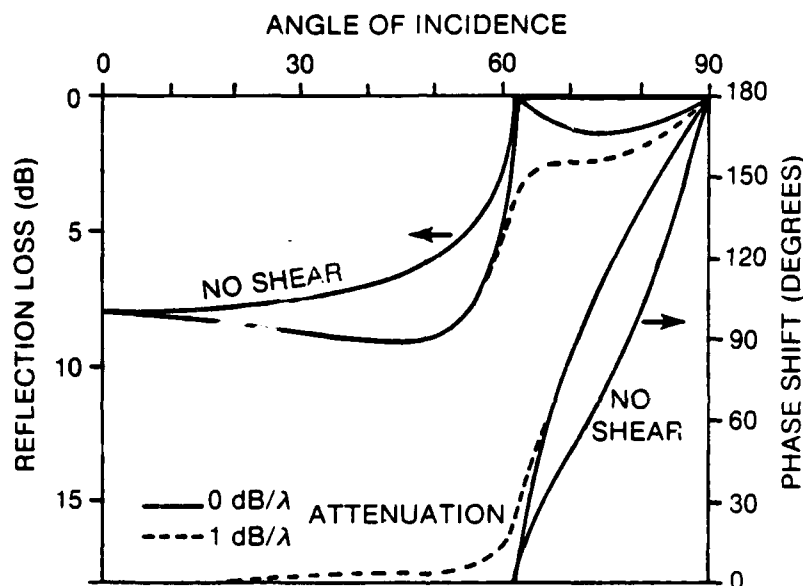
Figure 7-1.   Reflection Loss for a Half-Space with One Critical Angle

TWO CRITICAL ANGLES $\alpha_1 > \beta_1 > 1$

This is the case when we are looking of reflection from a sedimentary rock half-space. Figure 7-2 diagrams the reflection loss and phase shift for the following acoustic values: $\alpha_1 = 1.87$, $\beta_1 = 1.07$, $\rho_1 = 2.2$, again with 0 and 1 dB/ attenuation for both waves.

ANGLE OF INCIDENCE
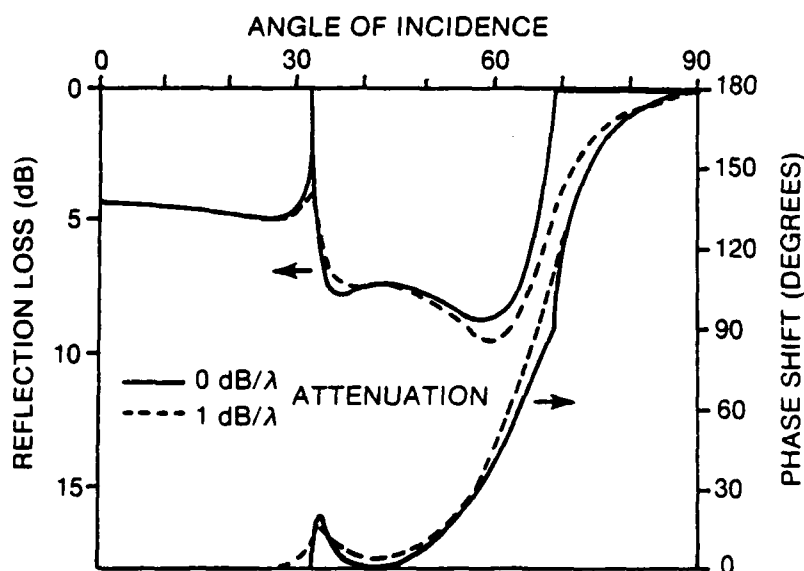
Figure 7-2. Reflection Loss for a Half-Space with Two Critical Angles

As the grazing angle diminishes and we reach the critical angle arc sin $(1/\alpha_1)$, the reflection will be total, but only at this angle when no attenuation is present. For angles between the two critical angles, the reflection coefficient will be less than one, since the shear waves will be carrying energy away from the boundary. In this interval, the bottom impedance is complex, and when the imaginary part is zero, the phase shift is also zero. This corresponds to $\cos^2 \eta_1$ $= 0$ which gives $\eta_1 = 45°$ and from Snell's Law, θ = arc sin $(\sqrt{2}/2 \cdot \beta_1)$ $= 41.36°$ in our case. From differentiation with respect to η, this value also corresponds to a minimum as seen in figure 7-2. Only after the last critical angle arc sin $(1/\beta_1)$ $= 69.2°$ or 20.8° grazing has been reached, can total reflection occur.

RAYLEIGH INTERFACE WAVES $\alpha_1 > \beta_1 > 1.09$

This case is not a typical situation, but it is interesting, being related to the propagation of Rayleigh interface waves. Figure 7-3 shows the reflection

33

loss and phase shift for the following bottom parameters: $\alpha_1 = 3.48$, $\beta_1 = 2.0$, $\rho_1 = 2.5$ with no attenuation included to enhance the shape of the curves. The phase shift curve again has the minimum for $\theta = 20.705°$; it also has a jump from $+180°$ to $-180°$ for $\theta = 32.92°$. The Rayleigh wave velocity for a half-space with the above constants can be shown to be $V_R = 0.920 \cdot \beta_1 = 1.840$, which turns out to be equal to the horizontal phase velocity $c = 1/\sin(32.92) = 1.840$. This value can be shown to correspond to a pole in the complex reflection coefficient.

ANGLE OF INCIDENCE
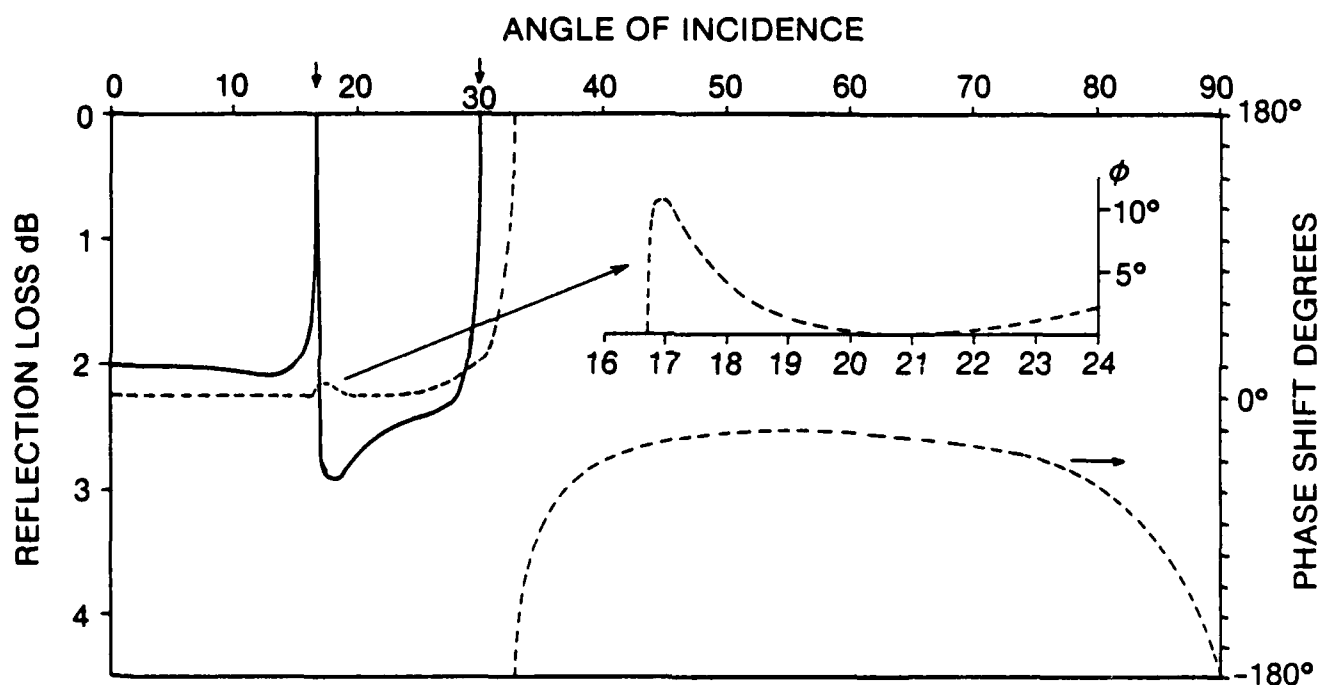
Figure 7-3. Reflection Loss for a Solid Half-Space Supporting Rayleigh Waves

CHAPTER 8

LIQUID LAYERS

Before looking at some examples for layers with both compressional and shear waves, let us consider a bottom consisting of unconsolidated sediments which acoustically can be considered liquid due to the very low shear modulus. We will study this type of layering in more detail since some of the results we will obtain are useful for the understanding of several reflection processes.

In this case $\gamma = 2(\beta/c) = 0$ and no shear potentials exist so the boundary conditions are reduced to the requirement of continuity of only σ and $\dot{W}$ across an interface. The 4 x 4 T matrix reduces to a 2 x 2 matrix and we obtain along the same lines as in chapter 6:

$$\overline{S} = \overline{\overline{T}}[z] \, \overline{P} \text{ with } \overline{\overline{T}} = \begin{bmatrix} t_{21} & t_{22} \\ t_{31} & t_{32} \end{bmatrix}$$

$$\text{and } \overline{S} = \begin{bmatrix} \dot{w}/c \\ \sigma \end{bmatrix} \qquad \text{and} \qquad \overline{P} = \begin{bmatrix} A + B \\ A - B \end{bmatrix}$$

Using the appropriate values for t_{ij} from chapter 6, we get the following for the mth layer:

$$\overline{\overline{T}}_m \, [d] = \begin{bmatrix} i(\alpha_m/c) \, a_m \cdot \sin P_m & -(\alpha_m/c) \, a_m \cdot \cos P_m \\ \rho_m \cdot \alpha_m^2 \cdot \cos P_m & -i \, \rho_m \cdot \alpha_m^2 \cdot \sin P_m \end{bmatrix}$$

where $P_m = a_m \cdot h \cdot d_m$ is the phase shift through layer m.

$$\overline{\overline{T}}_m \, [0]^{-1} = \begin{bmatrix} 0 & 1/\rho_m \cdot \alpha_m^2 \\ -1/(\alpha_m/c)^2 \, a_m & 0 \end{bmatrix}$$

which with $\overline{\overline{A}} = \overline{\overline{T}}[d] \, \overline{\overline{T}}[0]^{-1}$ gives:

$$\overline{\overline{A}}_m = \begin{bmatrix} \cos P_m & ia_m \, (\rho_m \cdot c^2)^{-1} \cdot \sin P_m \\ i \, \rho_m \, c^2 \, a_m^{-1} \cdot \sin P_m & \cos P_m \end{bmatrix}$$

For the total number of layers:

$$\overline{S}_{n-1} = \overline{\overline{A}}_{n-1} \cdot \overline{\overline{A}}_{n-2} \ldots \overline{\overline{A}}_1 \cdot \overline{S}_0 = \overline{\overline{A}} \, \overline{S}_0$$

which is the matrix equation relating the boundary conditions at the bottom and the top of the layering. Or:

$$\overline{P} = \overline{\overline{T}}[0]^{-1} \cdot \overline{\overline{A}} \cdot \overline{S} = \overline{\overline{H}} \cdot \overline{S}$$

which with $\begin{bmatrix} A \\ A \end{bmatrix} = \begin{bmatrix} h_{11} & h_{12} \\ h_{21} & h_{22} \end{bmatrix} \begin{bmatrix} \dot{w}/c \\ \sigma \end{bmatrix}$ and $z_b = -\sigma/\dot{w}$ gives: $z_b = \dfrac{h_{11} - h_{21}}{c \, (h_{12} - h_{22})}$

and reflection coefficient $R = (z_b - z)/(z_b + z)$. Let us now consider some simple and illustrative cases.

The Bottom Consisting of a Half-Space

With no layers present, $H = T[0]^{-1}$ and we have:

$h_{11} = h_{22} = 0$, $h_{12} = 1/\rho_1 \, \alpha_1^2$ and $h_{21} = -1/(\alpha_1/c)^2 \cdot a_1$, so that

$$z_b = \alpha_1 \, \rho_1/\cos \theta_1 \quad ,$$

agreeing with the previous results.

The Bottom Consisting of a Single Layer over a Half-Space

In this case, we get for the H matrix:

$$\overline{\overline{H}} = \begin{bmatrix} 0 & 1/\rho_2 \, \alpha_2^2 \\ -1/(\alpha_2/c)^2 \, a_2 & 0 \end{bmatrix} \begin{bmatrix} \cos P_1 & ia_1 \, (\rho_1 \, c^2)^{-1} \sin P_1 \\ i \, \rho_1 \, c^2 \, a_1^{-1} \sin P_1 & \cos P_1 \end{bmatrix}$$

with the index 1 and index 2 referring respectively to the layer and the half-space.

After some lengthy calculations and setting $z_1 = \alpha_1 \rho_1 / \cos \theta_1$ and $z_2 = \alpha_2 \rho_2 / \cos \theta_2$, the total bottom impedance becomes:

$$z_b = \frac{z_2 \cos P_1 + i\, z_1 \sin P_1}{\cos P_1 + i\, z_2/z_1 \sin P_1}$$

and the reflection coefficient becomes:

$$R = \frac{(z_2 - z) + i(z_1 - \dfrac{zz_2}{z_1}) \tan P_1}{(z_2 + z) + i(z_1 + \dfrac{zz_2}{z_1}) \tan P_1}$$

where Z is the impedance of the water.

Contrary to the simple half-space solution, the reflection coefficient is an oscillating function of P_1, which can be written as $P_1 = 2\pi \, (d_1/\lambda_1) \cos \theta_1$. For vertical incidence, two special cases exist, one corresponding to a layer thickness equal to a number of integer half-wavelengths and one corresponding to an odd number of quarter-wavelengths.

If $P = m\,\pi$ for m = 1, 2, 3..., sin P = 0 and we get:

$$R = (z_2 - z)/(z_2 + z),$$

meaning that a half-wave layer has no influence on the reflectivity which is being controlled only by the half-space. This could also be seen from the A matrix for a layer, which, for sin P = 0 and cos P = 1, reduces to the unit matrix, meaning that such layers have no influence on the total reflection coefficient.

If $P = m\,\pi/2$ for m = 1, 3, 5,..., cos P = 0 and sin P = 1 and we get:

$$R = (Z_1^2 - Z_2 \cdot Z)/(Z_1^2 + Z_2 \cdot Z)$$

Therefore, if $Z_1 = \sqrt{Z_2 \cdot Z}$, no reflection takes place. This particular case is very frequently utilized in optics where quarter-wave coatings are used to increase the transmitted light in, for example, lens systems.

To illustrate how the loss depends on the frequency and the angle of incidence, we will study the case with the acoustic constants as given in table 8-1.

Table 8-1. Bottom Acoustic Constants for a Two-Layer Model

ALPHA	BETA	RHO	AA	AB	DEPTH
.970	.000	1.450	.100	.000	1.000
1.050	.000	1.850	.300	.000	

where AA and AB are the attenuations in dB per wavelength.

The losses are shown in figures 8-1 and 8-2 for 15° and 60° angles of incidence, respectively. Note that the interference pattern clearly corresponds to quarter- and half-wavelengths in the layer with minimum losses equal to the case where only the half-space was present. As the angle of incidence increases, there is a shift toward higher frequencies due to the cos θ term for the phase shift in the layer.

The formula for the reflection coefficient can be rewritten using the two local reflection coefficients at the two interfaces 0 and 1, with $r_{01} = (Z_1 - Z)/(Z_1 + Z)$ and $r_{12} = (Z_2 - Z_1)/(Z_2 + Z_1)$:

$$R = \frac{r_{01} + r_{12} \cdot e^{-2ik_1 d_1}}{1 + r_{12} \cdot r_{01} \cdot e^{-2ik_1 d_1}}$$
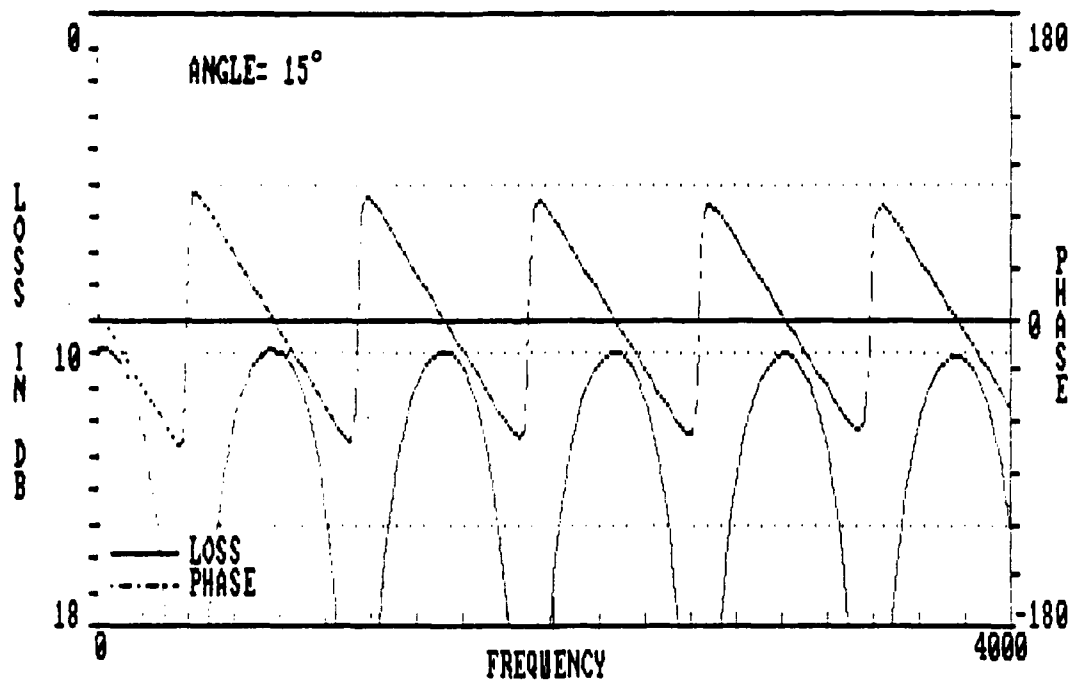
Figure 8-1. Reflection Loss and Phase Shift as a Function of Frequency
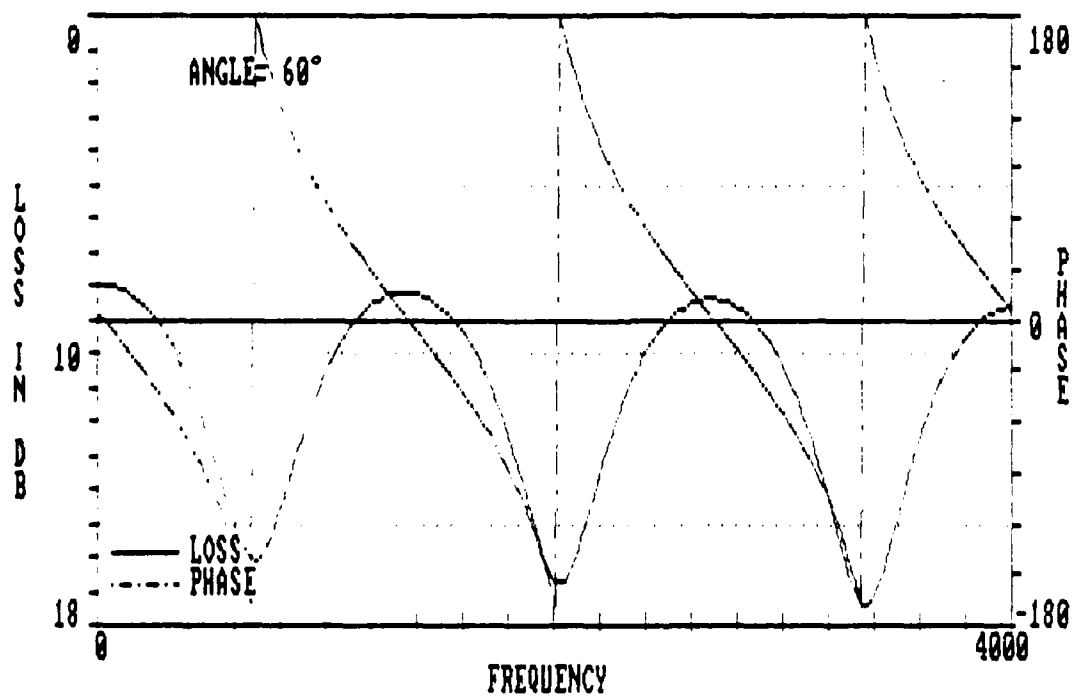
(15° Angle of Incidence)

Figure 8-2. Reflection Loss and Phase Shift as a Function of Frequency

(60° Angle of Incidence)

an expression attributed to the famous astronomer G.B. Airy in 1833. This result can also easily be obtained by the following considerations. Looking at the ray paths in the layering as seen in figure 8-3, we can write the total reflection coefficient as:

$$R = r_{01} + t_{01} \cdot r_{12} \cdot t_{10} \cdot e^{-2ik_1 d_1} + t_{01} \cdot r_{12} \cdot r_{10} \cdot r_{12} \cdot t_{10} \cdot e^{-4ik_1 d_1} + t_{01} \cdot r_{12} \cdot r_{10} \cdot r_{12} \cdot r_{10} \cdot r_{12} \cdot e^{-6ik_1 d_1} + \ldots$$

$$R = r_{01} + t_{01} \cdot r_{12} \cdot t_{10} \, (1 + r_{10} \cdot r_{12} \cdot e^{-2ik_1 d_1} + r_{10}^2 \cdot r_{12}^2 \cdot e^{-4ik_1 d_1} + \ldots)$$

$$R = r_{01} + t_{01} \cdot r_{12} \cdot t_{10} \cdot e^{-2ik_1 d_1} \cdot \frac{1}{1 - r_{10} \cdot r_{12} \cdot e^{-2ik_1 d_1}}$$

with $e^{-i2k_1 d_1}$ being the phase shift for a double passage through the layer.
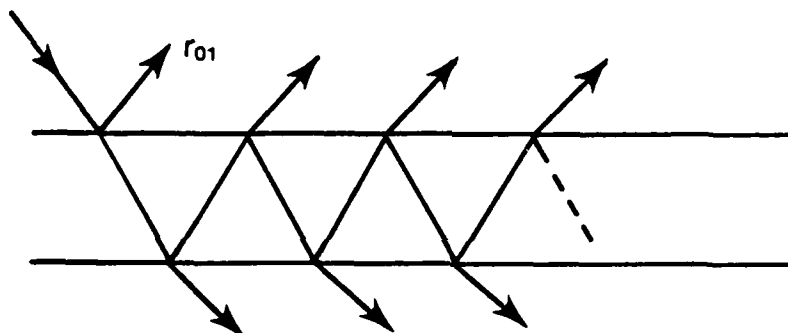
Figure 8-3. Ray Paths in Layers

Rearranging using $r_{ij} = -r_{ji}$ and $t_{ij} = 1 + r_{ij}$, the above reduces to the Airy expression which is very useful and can be applied recursively to calculate the reflection coefficient from a multilayered medium. We will later use it to study some special cases, such as a density gradient in a layer and reflection close to grazing.

For weakly reflecting layers, the local reflection coefficients are small compared to unity and we can ignore second order terms. Thus, the reflection coefficient can be written in the simple form:

$$R = r_{01} + r_{12} \cdot e^{i2\phi_1} \quad ,$$

a formula well suited for recursive calculation in the case of multilayers. This approximation corresponds to the graphical polygon technique used in optics before the days of computers by calculating the reflection coefficient using vector addition of the local reflection coefficients for a set of layers. Though this method is now obsolete, it is quite illustrative and we will use it for the three-layer model given in table 8-2 and construct the reflection coefficient for ≈ 0, 150, and 300 Hz at vertical incidence.

Table 8-2. Bottom Acoustic Constants for a Three-Layer Model

ALPHA	BETA	RHO	AA	AB	DEPTH
1.050	.000	1.890	.000	.000	1.000
1.130	.000	2.050	.000	.000	1.500
1.870	.000	2.200	.000	.000	

From the two reflection coefficients, we get:

$$R = r_{01} + R_1 \cdot e^{i2\phi_1}$$

$$R_1 = r_{12} + r_{23} \cdot e^{i2\phi_2}$$

as a function of the local reflection coefficients and the phase shift in the two layers. From the impedances, these are easily computed:

$$r_{01} = 0.332$$
$$r_{12} = 0.075$$
$$r_{23} = 0.279$$

In the following we will give the reflection coefficient and phase shift obtained (1) graphically (signified by "graph") from figure 8-4, numerically ("num"), and exactly ("exact") using transfer matrices.

a) <u>f = 0 Hz</u>

In this case, $\phi_1^o = \phi_2^o = 0$ and the local reflection coefficients are on the same line as seen in figure 8-4. Computing the equation graphically, numerically, and exactly, we get:

R = 0.332 + 0.075 + 0.279 = 0.69 (graph)
R = 0.686 (num)
R = 0.609 (exact)

b) <u>f = 150 Hz</u>

The two phase shifts in degrees are:

$\phi_1^o = 360 \cdot 0.1 \cdot 1.0/1.055 = 34.12°$
$\phi_2^o = 360 \cdot 0.1 \cdot 1.5/1.13 = 47.79°$

Results obtained are:

R = 0.18 and ϕ = -58° (graph)
R = 0.178 and ϕ = -55.9° (num)
R = 0.194 and ϕ = -55.99° (exact)

c) <u>f = 300 Hz</u>

The two phase shifts are obtained as above, yielding

$\phi_1^o = 128.48°$
$\phi_2^o = 191.16°$

From the vector addition, we have:

R = 0.51 and ϕ = 13° (graph)
R = 0.510 and ϕ = 13.8° (num)
R = 0.494 and ϕ = 8.84° (exact)

The accuracy of the approximate method, whether graphical or numerical, for the above cases can be considered to be quite satisfactory for the interference effects from the different layers.
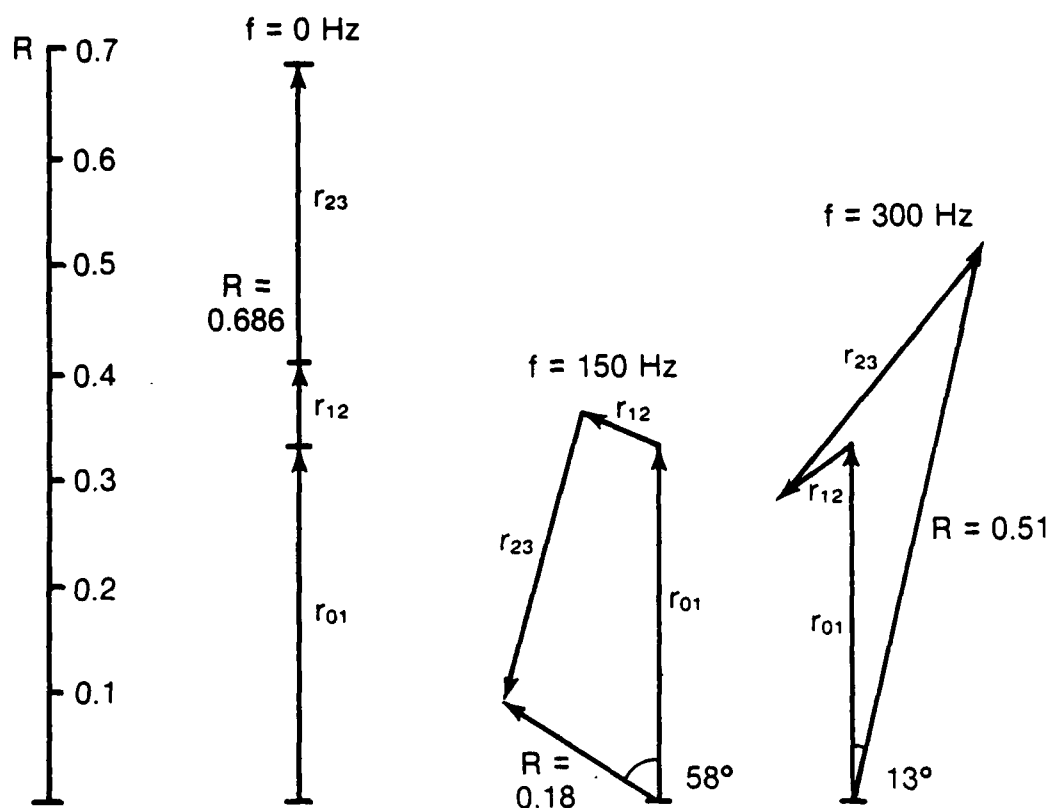
Figure 8-4. Vector Addition of Reflection Coefficients

Now let us look at the phase shift as a function of frequency and impedance for this simple two-layer liquid bottom. The phase shift   is determined as

$$\tan \psi = \frac{\text{Im}[R]}{\text{Re}[R]}$$

where $\text{Im}[R]$ and $\text{Re}[R]$ are the imaginary and real parts of the reflection coefficient. Inserting these values and setting the phase shift in the layer 2 $k_1 d_1 =$ ϕ, the phase shift for the reflection becomes:

$$\tan \psi = \frac{r_{12} (r_{01}^2 - 1) \sin \phi}{r_{01} (r_{12}^2 + 1) + r_{12} (r_{01}^2 + 1) \cos \phi}$$

We will discuss some different cases according to the relative magnitude of the two local reflection coefficients, r_{01} and r_{12}, and assume that the angle

43

of incidence is less than critical and that the reflection coefficients are small compared to 1 so we can ignore higher order terms. The expression for the phase shift can then be rewritten as:

$$\tan \psi \approx \frac{-\sin \phi}{r_{01}/r_{12} + \cos \phi}$$

a) $\underline{r_{12} \gg r_{01}}$

This corresponds to a weak reflector on top of a stronger reflecting half-space. The phase shift becomes:

$$\tan \psi \approx -\tan \phi$$

and

$$\psi \approx -\phi = -2k_1 \cos \theta_1 \, d_1 \text{ or}$$

$$\psi \approx -\omega \frac{2d_1 \cos \phi_1}{\alpha_1}$$

which is a linear phase shift corresponding to a simple time delay as one would expect.

b) $\underline{r_{01} = r_{12}}$

In this case the phase shift is

$$\tan \psi \approx \frac{\sin \phi}{1 + \cos \phi}$$

$$\psi \approx -\phi/2$$

again a linear phase behaviour with respect to frequency but with only half the slope or time delay as compared to the case above.

Figures 8-5 and 8-6 show the phase shifts calculated from the transfer matrices and clearly demonstrate the near-linear dependence. This is also very often the situation observed from experiments, even when we are dealing with a complicated multilayered bottom as seen from figures 16-3 and 16-4 in chapter 16.
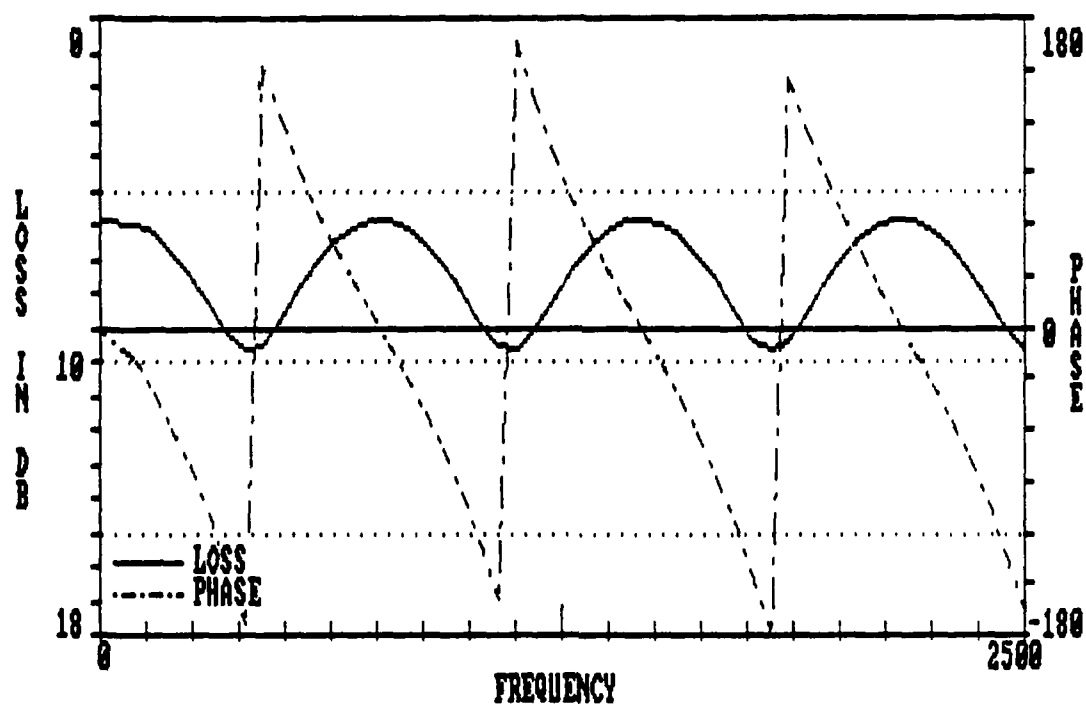
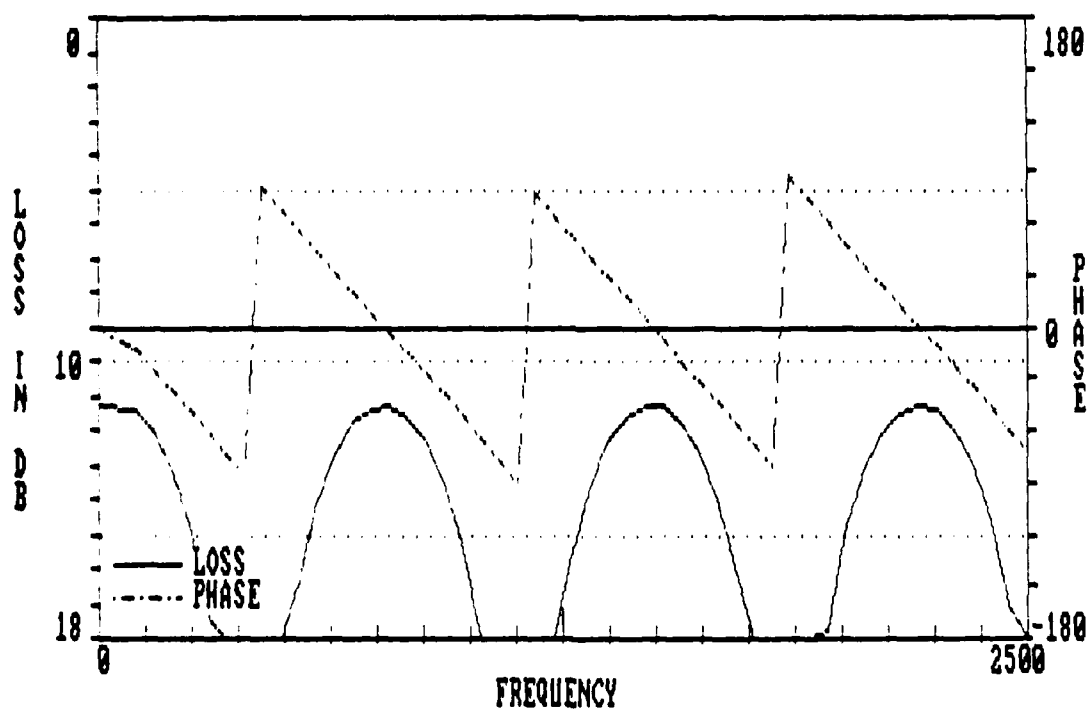Figure 8-5. Phase Shift for $\alpha_1 = 0.96$, $\alpha_2 = 1.23$, $\rho_1 = 1.3$, $\rho_2 = 2.5$

Figure 8-6. Phase Shift for $\alpha_1 = 0.98$, $\alpha_2 = 1.03$, $\rho_1 = 1.35$, $\rho_2 = 1.7$

CHAPTER 9

HIGH LOSS AT GRAZING

It is frequently believed that with a bottom for which a critical angle exists and for small grazing angles, reflection will always be close to perfect, with no or very little loss. Although this can be true, there are situations where the reflection coefficient behaves differently.

The sea floor under consideration is a soft, low-velocity layer on top of a harder, high-velocity half-space as indicated in figure 9-1. With $\alpha_2 > 1 > \alpha_1$ and r_{01} and r_{12} (the local Rayleigh reflection coefficients), we have an intromission angle case for r_{01} and a critical angle case for r_{12}. Further, we will consider the case where θ is small and $\theta < \arccos(1/\alpha_2)$, in other words the reflection from interface 1-2 is total.
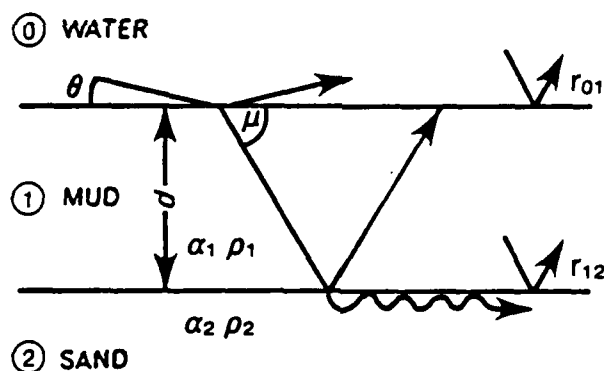
Figure 9-1. Layering Geometry

Using the Airy expression from the previous chapter for the reflection coefficient for the complete layering and in this case the more convenient grazing angle instead of the angle of incidence, we get:

$$R(\theta, k) = \frac{r_{01} + r_{12} \cdot e^{i\phi}}{1 + r_{01} \cdot r_{12} \cdot e^{i\phi}} \tag{9-1}$$

where $\phi = 2kd \cdot \sin\mu$ is the geometrical phase shift through the layer, with k being the wavenumber. We will study this expression in more detail for $\theta \to 0$.

From Snell's Law, we have

$$\frac{\cos \theta}{\cos \mu} = \frac{1}{\alpha_1}$$

$$\mu = \arccos(\alpha_1 \cdot \cos \theta),$$

$$\frac{d\mu}{d\theta} = \frac{\alpha_1 \sin \theta}{\sqrt{1 - (\alpha_1)^2 \cos^2 \theta}}$$

which for $\theta \to 0$ gives $\dfrac{d\mu}{d\theta} \to 0$.

This means μ will vary little with θ for θ close to zero, and we will consider it constant and equal to μ_0.

For small grazing angles, as discussed in chapter 4, the local reflection coefficient is expressed by exponential functions:

$$r_{01} = -e^{-Q\theta}$$
$$r_{12} = -e^{-S'\mu},$$

with

$$Q = \frac{2\rho_1}{\sqrt{(1/\alpha_1)^2 - 1}} \qquad (9-2)$$

$$S' = \frac{2\rho_2/\rho_1}{\sqrt{(\alpha_1/\alpha_2)^2 - 1}}$$

For $\alpha_2 > 1 > \alpha_1$, Q is real and positive and S' is imaginary and negative:

$$S' = \frac{i\,2\rho_2/\rho_1}{\sqrt{1 - (\alpha_1/\alpha_2)^2}} = -iS$$

and

$$R_{23} = -e^{iS\mu} = e^{i(S\mu - \pi)}.$$

$(9-3)$

Inserting equations (9-2) and (9-3) into equation (9-1), we get:

$$R(\theta, k) = \frac{-e^{Q\theta} + e^{i(S\mu - \pi)} \cdot e^{i\phi}}{1 - e^{Q\theta} \cdot e^{i(S\mu - \pi)} \cdot e^{i\phi}}$$

or

$$R(\theta, k) = \frac{-e^{Q\theta} + e^{i(S\mu - \pi + 2dk \cdot \sin\mu)}}{1 - e^{Q\theta} \cdot e^{i(S\mu - \pi + 2dk \cdot \sin\mu)}}$$

which for $\theta \to 0$ and $\mu \to \mu_0$ gives

$$R(k) \underset{\theta \to 0}{=} - \frac{1 - e^{iS\mu_0 - \pi + 2dk \cdot \sin\mu_0)}}{1 - e^{iS\mu_0 - \pi + 2dk \cdot \sin\mu_0)}} = -1$$

as expected: total reflection with a 180° phase shift.

But when $\quad e^{iS\mu_0 - \pi + 2dk \cdot \sin\mu_0)} = 1$ (9-4)

we have a singularity with $\quad R \to \dfrac{0}{0} \quad$ for $\quad \theta \to 0$.

From physical reasons, we know that $|R| < 1$ and we can, therefore, expect R to have a minimum. This can also be shown by numerical calculations since the work involved in the analytical study of R(k) at this singularity is very tedious.

From equation (9-4), we find

$$S \cdot \mu_0 - \pi + 2dk \sin\mu_0 = 2n \cdot \pi, \; n = 0, 1, 2, \ldots$$

and with $\quad k = 2\pi/\lambda$

$$\left(\frac{d}{\lambda}\right)_n = \frac{(2n + 1)\pi - S\mu_0}{4\pi \sin\mu_0}$$ (9-5)

For these values the reflection coefficient will be very small, even very close to grazing. Figure 9-2 shows the reflection loss as a function of θ and d/λ for the layering used in the previous chapter.
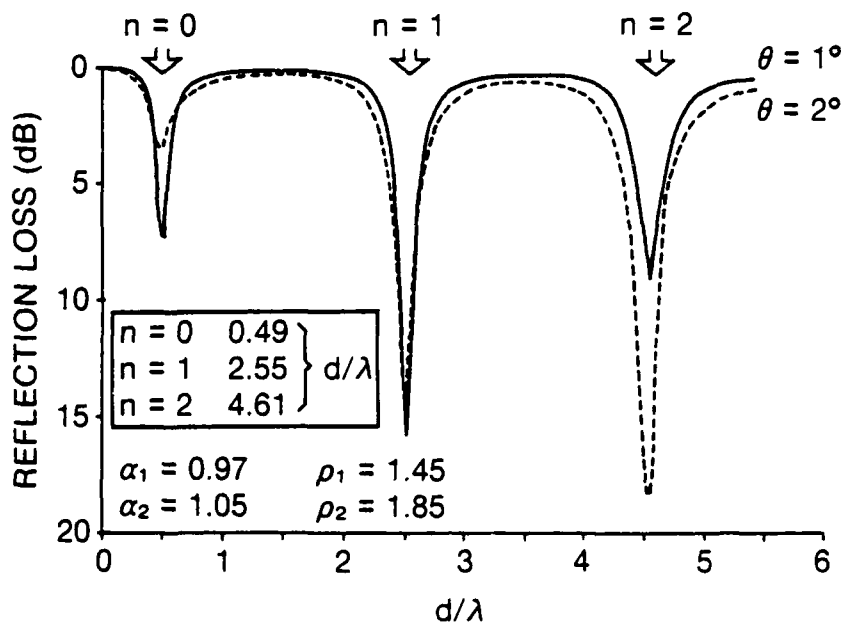
Figure 9-2. Reflection Loss as a Function of Wavelength

for 1° and 2° Grazing Angles

Using the above parameters at equation (9-5), we can then calculate the d/λ values for which high losses are expected:

$$(d/\lambda)_n = \frac{(2n + 1)\,\pi - 1.637}{3.055}$$

This yields

$$d/\lambda = \begin{cases} 0.49 & n = 0 \\ 2.55 & n = 1 \\ 4.61 & n = 2 \end{cases}$$

One should note that the value of $d/\lambda = 0.49$, close to 1/2, is a coincidence and that d/λ values increase with increasing hardness of the lowest layer, with d/λ approaching 0.8 for $n = 0$ in the case of a very hard layer.

These high-loss d/λ values are shown in figure 9-2 as arrows and agree very well with those calculated numerically from equation (9-1) at 1° and 2° grazing. To indicate how the loss varies with grazing angles for different d/λ values, figure 9-3 shows the losses for the same case with $d/\lambda = 0$, 0.5, 2, and ∞, the first and last corresponding to only the high-velocity half-space and a half-space with the characteristics of the upper layer. Note the extremely small angle for which a high loss is obtained for $d/\lambda = 0.5$.

Figure 9-3. Reflection Loss as a Function of Grazing Angle
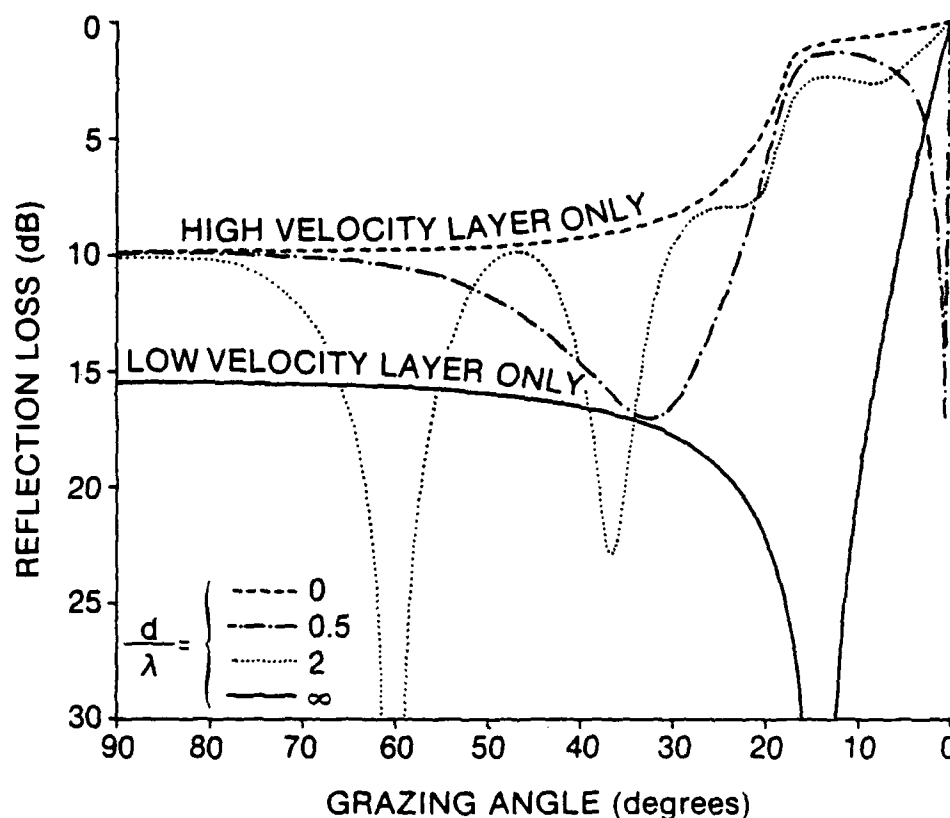
How can we explain these reflection loss anomalies for discrete d/λ values? Let us look at the waves being reflected inside the first layer, as seen in figure 9-4.
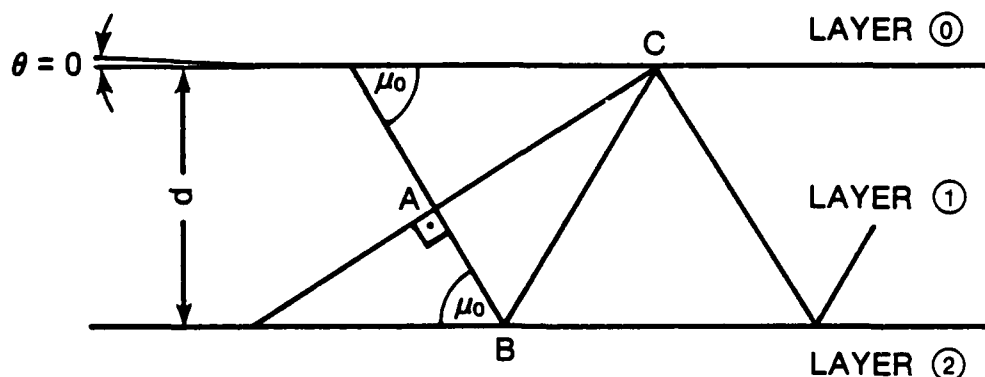
Figure 9-4. Wave Path in the Bottom Layer

When $\theta \rightarrow 0$, the local reflection coefficient $\Gamma_{10} = 1$ with a zero-degree phase shift, since we have a plane wave coming from medium 1 being reflected from the higher medium 0, where μ_0 is in fact the critical angle. Writing the equation for conditions under which the wave fronts interfere constructively in layer 1, we get:

$$(AB + BC) \cdot k + \psi_1 + \psi_2 = 2 \cdot \pi \cdot n,$$

where ψ_1 and ψ_2 are the phase shifts at the two interfaces. From the above, $\psi_1 = 0$ and $\psi_2 = S\mu_0 - \pi$, AB + BC is easily expressed by d, and μ_0 as:

$$AB + BC = 2d \sin \mu_0 \text{ or} \qquad (9-6)$$
$$S\mu_0 + 2dk \sin \mu_0 - \pi = 2\pi n,$$

which is exactly the same criterion for the singularities in the reflection coefficient.

This means that we are dealing with the propagation of trapped modes in the top layer and their characteristic equation is equation (9-6). With just a small amount of attenuation in the layer, it absorbs most of the incident energy and thereby creates a low reflection coefficient just close to grazing.

In shallow water sound propagation, one can also show that these singular frequencies correspond to similar singularities in the frequency-dependent transmission loss.

Figure 9-5 illustrates the relative sound speed and density measured on a core taken on the Italian continental shelf. Using these acoustic parameters with a water sound speed of 1500 m/s and the layer depth d = 3.7 m, we find from equation (9-5) that high losses near grazing are expected for:

    f = 200 Hz,
    f = 1050 Hz,
    f = 1900 Hz,
    f = 2700 Hz,

which are within the frequency ranges for both active and passive sonar systems.
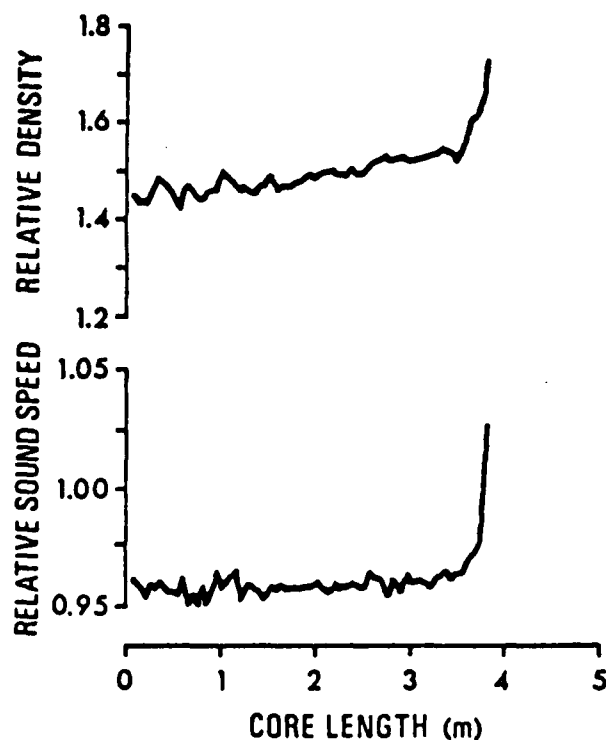

Figure 9-5. Sea Floor Characteristics

As a further illustration, the transmission losses for iso-velocity conditions at a range of 35 km and for a water depth of 115 m with bottom character-

istics corresponding to the above core have been calculated. Figure 9-6 very

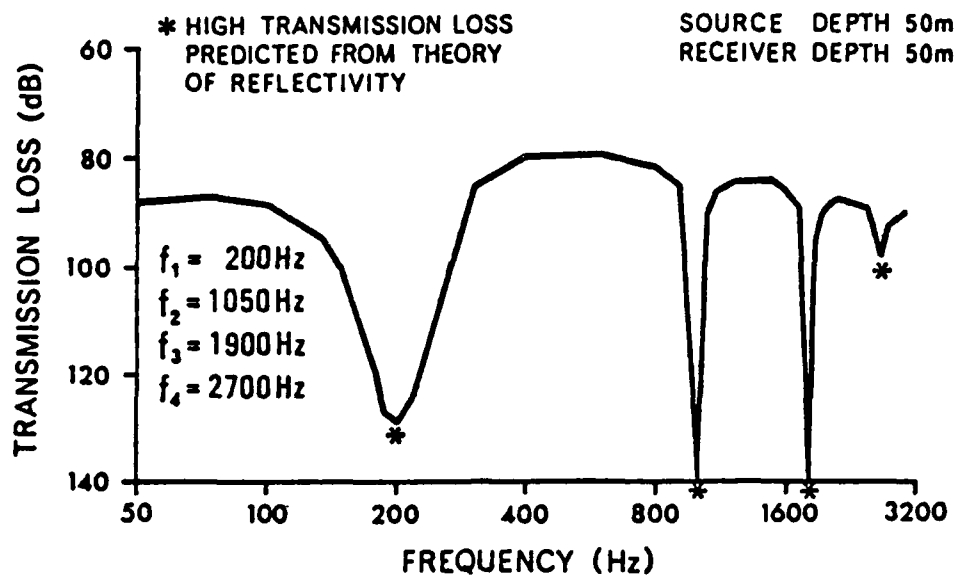markedly shows the effect on shallow-water transmission.

Figure 9-6. Transmission Loss as a Function of Frequency

CHAPTER 10

DENSITY GRADIENT

Again turning to what can be observed in nature, one will notice that for unconsolidated bottoms consisting of clay and silt, the analysis of cores can show a more or less constant wave velocity in the upper meters, whereas density clearly increases with depth. Let us look at one possible explanation for this.

In chapter 4, we were looking at the rather unusual case of bottom consisting of a mixture of gas bubbles, water and solid. We will now look at the very common case where there are no free gas bubbles present and we can treat the sediment as an ideal two-component mixture. The equations for the relative density and velocity from chapter 4 can be rewritten as:

$$\rho_{sed}/\rho_{water} = \rho_{solid}/\rho_{water} \cdot (1 - n) + n$$

and

$$\alpha_{sed}/\alpha_{water} = \sqrt{\left[\frac{\rho_{solid}}{\rho_{water}} (1 - n) + n\right] \frac{1}{\left[\frac{B_{solid}}{B_{water}} (1 - n) + n\right]}}$$

where n is the porosity.

Using $\rho_{solid}/\rho_{water}$ = 2.62 and B_{solid}/B_{water} = 0.0455, the values of $\rho_{sediment}/\rho_{water}$ and $\alpha_{sediment}/\alpha_{water}$ have been calculated. Figure 10-1 shows the relative sound velocity and density for a two-component sediment as a function of porosity, with the velocity exhibiting a wide minimum around a porosity of about 75 percent, whereas the density increases linearly with decreasing porosity.

Measurements on several thousand core samples indicate that our assumptions can be considered valid. We will frequently use this relationship between porosity, density, and velocity, known as the Woods equation. In situ, values for porosity usually range from 35 percent for coarse sands to 65 percent for silts and 85 percent for clays, as discussed in appendix C.
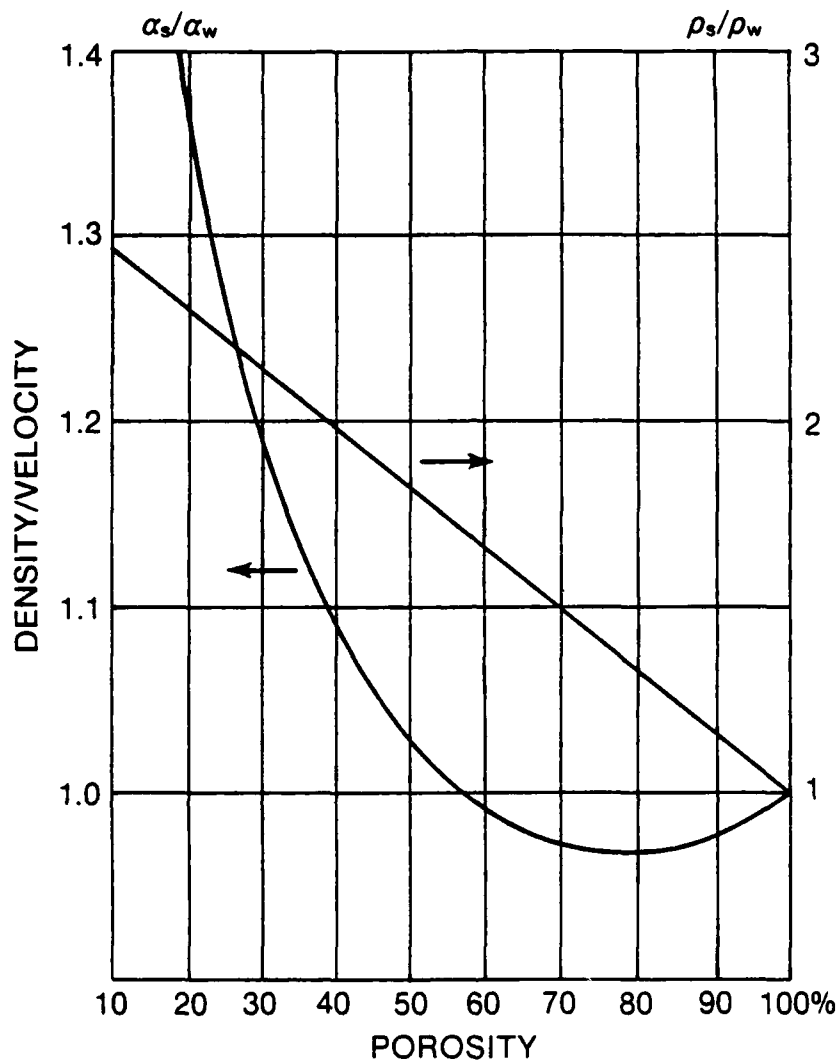
Figure 10-1. Relation between Density/Velocity and Porosity

Therefore, if we have a sediment with a porosity near 75 percent, a
decrease in porosity with increasing depth would change the relative velocity
very little.   However, the density would increase with depth, thereby creating
density gradient, as seen from figure 10-2, which is representative for several
cores taken in the Alboran Abyssal Plain to the east of Gibraltar.
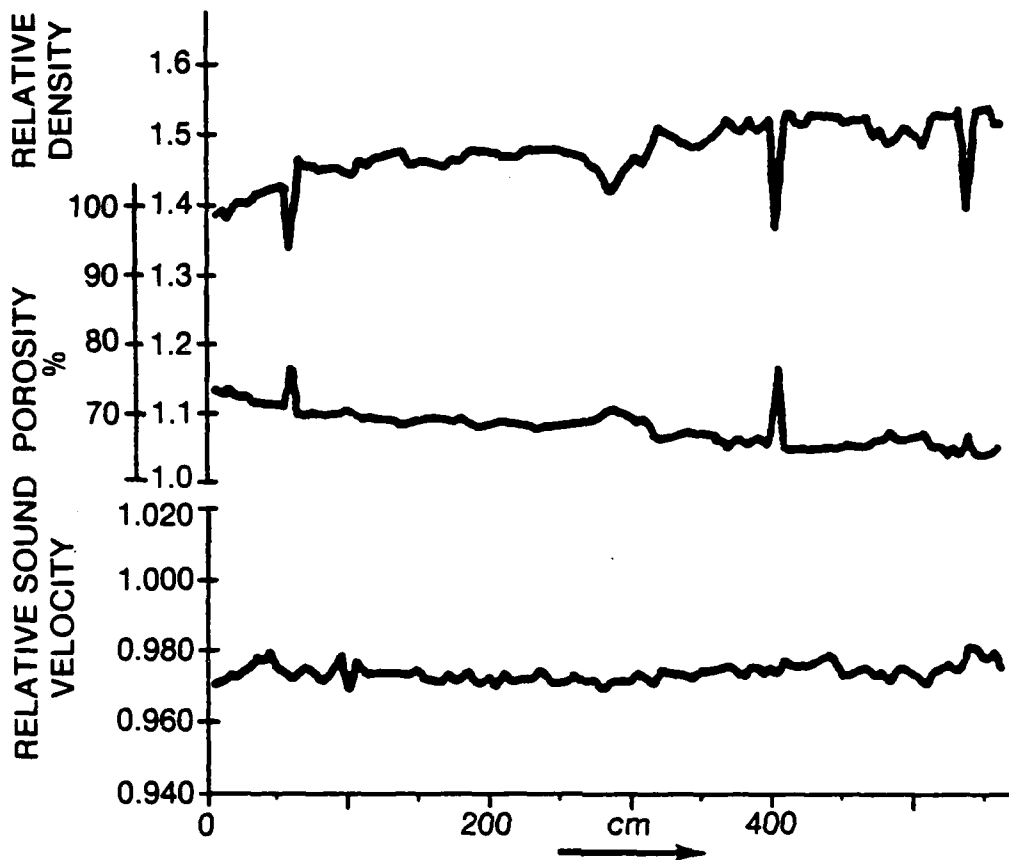
Figure 10-2. Example of Relative Density, Wave Velocity, and Porosity

The relative velocity is approximately 0.975 and we have a type of intromission angle reflection, in this case, with a frequency-dependent reflection coefficient due to the clearly seen density gradient.

To calculate the reflection coefficient, let us approximate the continuous density gradient with finite density steps, creating a layering system as seen in figure 10-3.
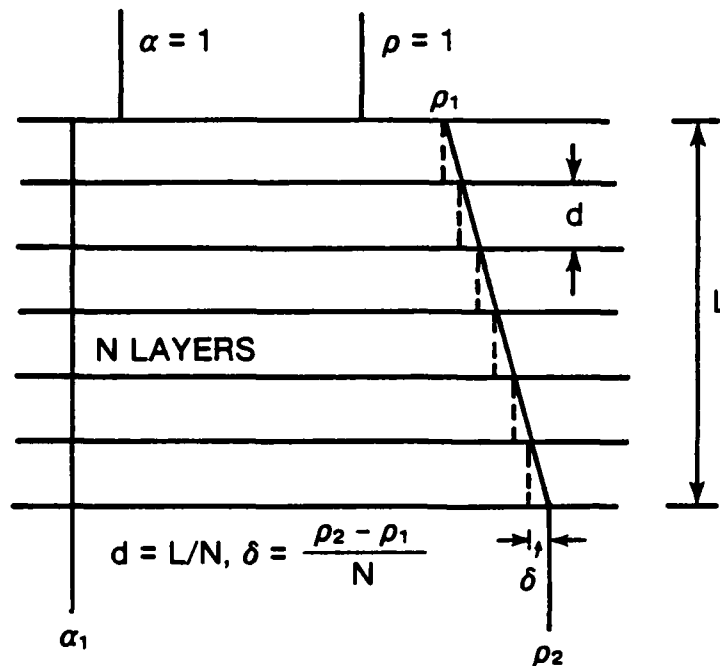
Figure 10-3. Approximation of Density Gradient

Using the Airy formula for the reflection coefficient from the n layer expressed by the local reflection coefficients, we have:

$$R_{n-1} = \frac{r_{n-1} + R_n \cdot e^{i\phi}}{1 + r_{n-1} \cdot R_n \cdot e^{i\phi}}$$

where:

r_{n-1} is the local reflection coefficient, depending on the density and wave velocity on each side of the n-1 interface,

R_n is the reflection coefficient from all the layers below interface n,

R_{n-1} is the reflection coefficient for all layers below interface n-1, and

ϕ is the two-way phase shift equal for all layers.

The formula can be used recursively but is not very convenient for our purpose. However, by selecting very thin layers and assuming that $1 > \alpha_1$ and $R_n \cdot r_{n-1} \ll 1$, we can as before use the much more convenient approximation:

$$R_{n-1} = r_{n-1} + R_n \, e^{i\phi}$$

which physically means that we are ignoring multiple reflections. Starting the calculations at the lowest interface N, we get:

$$R_N = r_N$$

$$R_{N-1} = r_{N-1} + R_N \cdot e^{i\phi}$$

$$\cdot$$
$$\cdot$$
$$\cdot$$

$$R_{n-1} = r_{n-1} + R_n \cdot e^{i\phi}$$

$$\cdot$$
$$\cdot$$
$$\cdot$$

$$R_1 = r_1 + R_2 \cdot e^{i\phi}$$

$$R_0 = r_0 + R_1 \cdot e^{i\phi}$$

or

$$R_0 = r_0 + r_1 \cdot e^{i\phi} + r_2 \cdot e^{i2\phi} + \ldots r_N \cdot e^{iN\phi}$$

With
$$r_n = \frac{\rho_{n+1} - \rho_n}{\rho_{n+1} + \rho_n} = \frac{\rho_2 - \rho_1}{N \, (\rho_{n+1} + \rho_n)}$$

$$r_n \approx \frac{\rho_2 - \rho_1}{N \, (\rho_2 + \rho_1)}$$

$$R_0 = r_0 + r_n \cdot e^{i\phi} \, [1 + e^{i\phi} + \ldots + e^{i(N-1)\phi}]$$

Applying the formula for a sum for geometrical series, we obtain for the reflection coefficient:

$$R_0 = r_0 + \frac{e^{i\phi} \, (\rho_2 - \rho_1)}{N \, (\rho_2 + \rho_1)} \cdot \frac{e^{iN\phi} - 1}{e^{i\phi} - 1}$$

and $\phi = 2 \cdot k_1 \cdot d \cdot \cos \theta$, with k being the wavenumber and θ the angle of incidence equal for all the thin layers. Using Snell's Law, this reduces to:

$$\phi = 2 \, \frac{L}{N} \cdot k_0/\alpha_1 \cdot \sqrt{1 - \alpha_1^2 \sin^2 \theta_0}$$

which is real for all angles of incidence.

Letting $N \to \infty$ and $d \to 0$, the density profile will approach a linear one and, after some calculations, we arrive at the following expression for the reflection coefficient for a layer with a density gradient:

$$R_0 = r_0 + \frac{\rho_2 - \rho_1}{\phi_0 \, (\rho_2 + \rho_1)} \cdot (\sin \phi_0 + i(1 - \cos \phi_0))$$

with

$$\phi_0 = 4\pi \cdot \frac{L}{\lambda_0} \cdot \frac{1}{\alpha_1} \cdot \sqrt{1 - \alpha_1^2 \cdot \sin^2 \theta_0}.$$

To see how the gradient affects the reflection coefficient, we will use the values from figure 10-2 which gives:

$$\alpha_1 = 0.975, \rho_1 = 1.4 \text{ and } \rho_1 = 1.5.$$

Figure 10-4 shows the reflection losses for selected angles of incidence and as function of dimensionless wavelength.
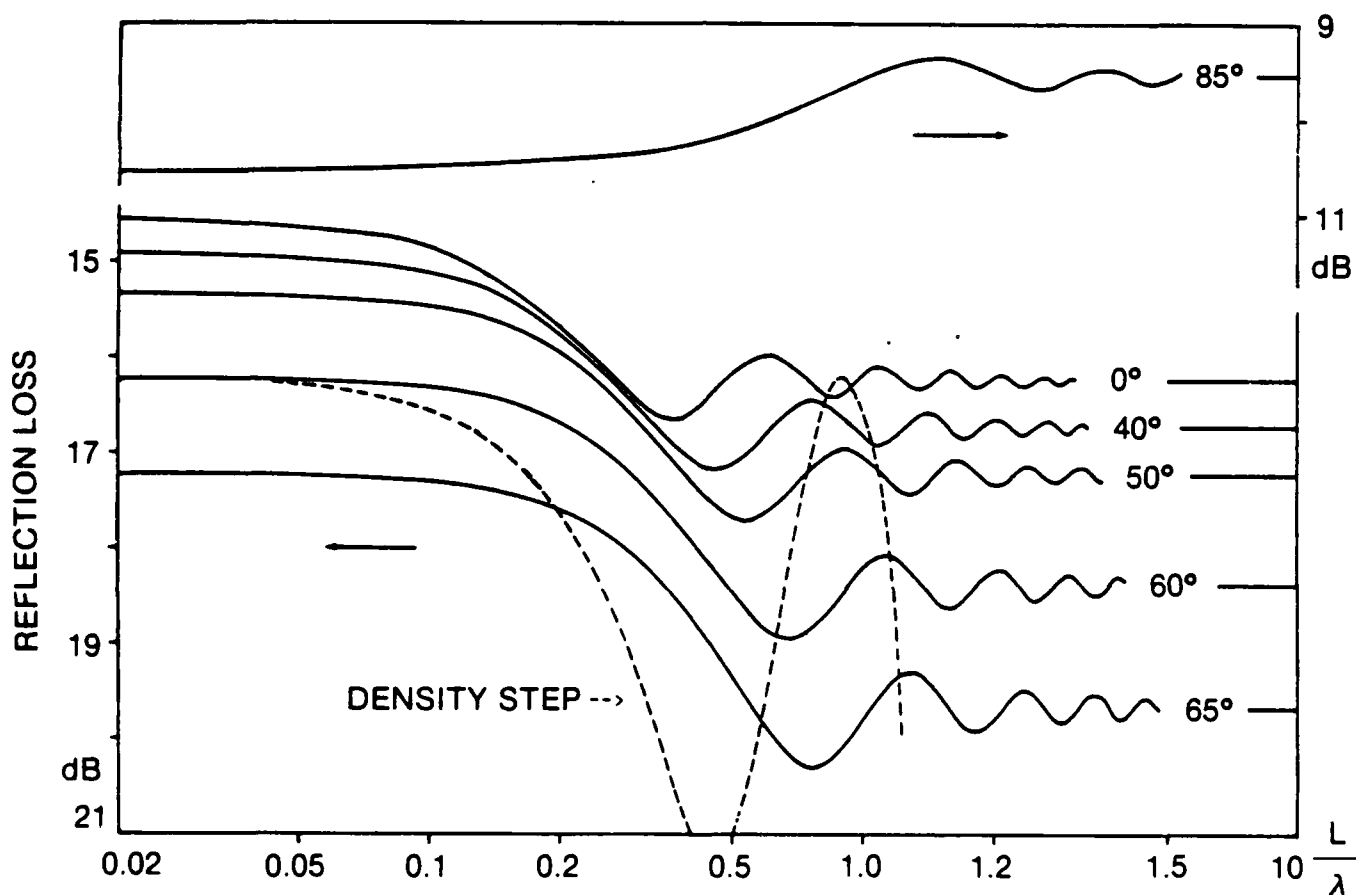
Figure 10-4. Reflection Loss in the Presence of a Density Gradient

The curves show the usual $\lambda/4$ and $\lambda/2$ oscillations, but being damped with increasing frequency, approaching an asymptotic loss value. The reason for this can be understood from the fact that, for long wavelengths/low frequencies, the gradient has little effect, whereas for shorter wavelengths/higher frequencies only the water-sediment interface affects the reflection coefficient. For comparison, figure 10-4 also shows the losses at 60° for the case with no gradient but with a single layer with a density of 1.4 and a half-space with a density of 1.5, showing the smoothing effect of the density gradient.

CHAPTER 11

EXAMPLES OF GENERAL LAYERING

When dealing with general multilayered bottoms, it is not possible analytically as in the past to study the behavior of the reflection coefficient as a function of angle of incidence and frequency. Therefore, we will use the transfer matrix method as described in chapter 6 to calculate numerically the reflection losses using three different bottom models with the acoustic parameters as given in table 11-1, with AA and AB being the attenuation of compressional and shear waves. In Model C, the density and compressional wave velocity are related to porosity through the Woods equation.

Table 11-1. Bottom Acoustic Constants for Three Models

MODEL	α	β	AA dB/λ	AB dB/λ	ρ	d	
A	1.0	0	0	0	1.0	—	Water
	1.055	0.26	1.0	1.5	1.89	1.0	45% Porosity
	1.13	0.40	1.5	2.5	2.05	—	35% Porosity
B	1.0	0	0	0	1.0	—	Water
	1.055	0.26	1.0	1.5	1.89	1.0	45% Porosity
	1.13	0.40	1.5	2.5	2.05	1.5	35% Porosity
	1.87	1.07	0.5	0.75	2.2	—	Limestone
C	1.0	0	0	0	0	—	Water
	Varying as function of porosity					1.0	
	1.13	0.40	1.5	2.5	2.05	—	35% Porosity

To give an overall image of the reflection loss as a function of angle of incidence and frequency, the reflection loss isolines were plotted in the angle of incidence-dimensionless wavenumber plane. Let us look at the results from the individual models.

MODELS A AND B

The reflection loss was calculated for three models, as given in table 11-1. For Model A, the reflection loss was also calculated for cases without shear waves or without attenuation. The results of the computations are shown in figures 11-1 to 11-4.

Several significant features are noticeable. One is the system of valleys and ridges originating at 0 degree incidence and being shifted toward higher frequencies with increasing angles. These low and high losses correspond respectively to half-wave and quarter-wave layer thicknesses. This means that the extremes will be determined by: $d \cos \theta = m\pi/4$.

At angles near the critical angle, the complexity increases and one often finds large losses in this region. After the critical angle in the top layer, the losses decrease quickly and show little frequency dependence. When comparing the losses for the case with and without shear waves, one will notice that the shape of the isoloss contours is very much the same, but generally with 1 to 2 dB lower losses in the absence of shear as one would expect.

Comparing the losses with and without attenuation shows some interesting features. The isoloss contours get much more irregular due to the unmasked interference between the two types of waves. After the critical angle in the deepest layer, the effect of the shear waves is clearly seen when the effective thickness equals quarter-wavelengths.

MODEL C

In the section above, we looked at solid layers supporting shear waves. From the cores taken at the SACLANTCEN, it seems that the porosity of the upper layers of the deep sea bed is usually about 70 to 80 percent. It might

Figure 11-1.   Reflection Loss in dB as a Function of the Angle of Incidence

and the Wavenumber - Model A

Figure 11-2. Reflection Loss in dB as a Function of the Angle of Incidence

and the Wavenumber - Model A, no Damping

Figure 11-3. Reflection Loss in dB as a Function of the Angle of Incidence
and the Wavenumber – Model A, no Shear
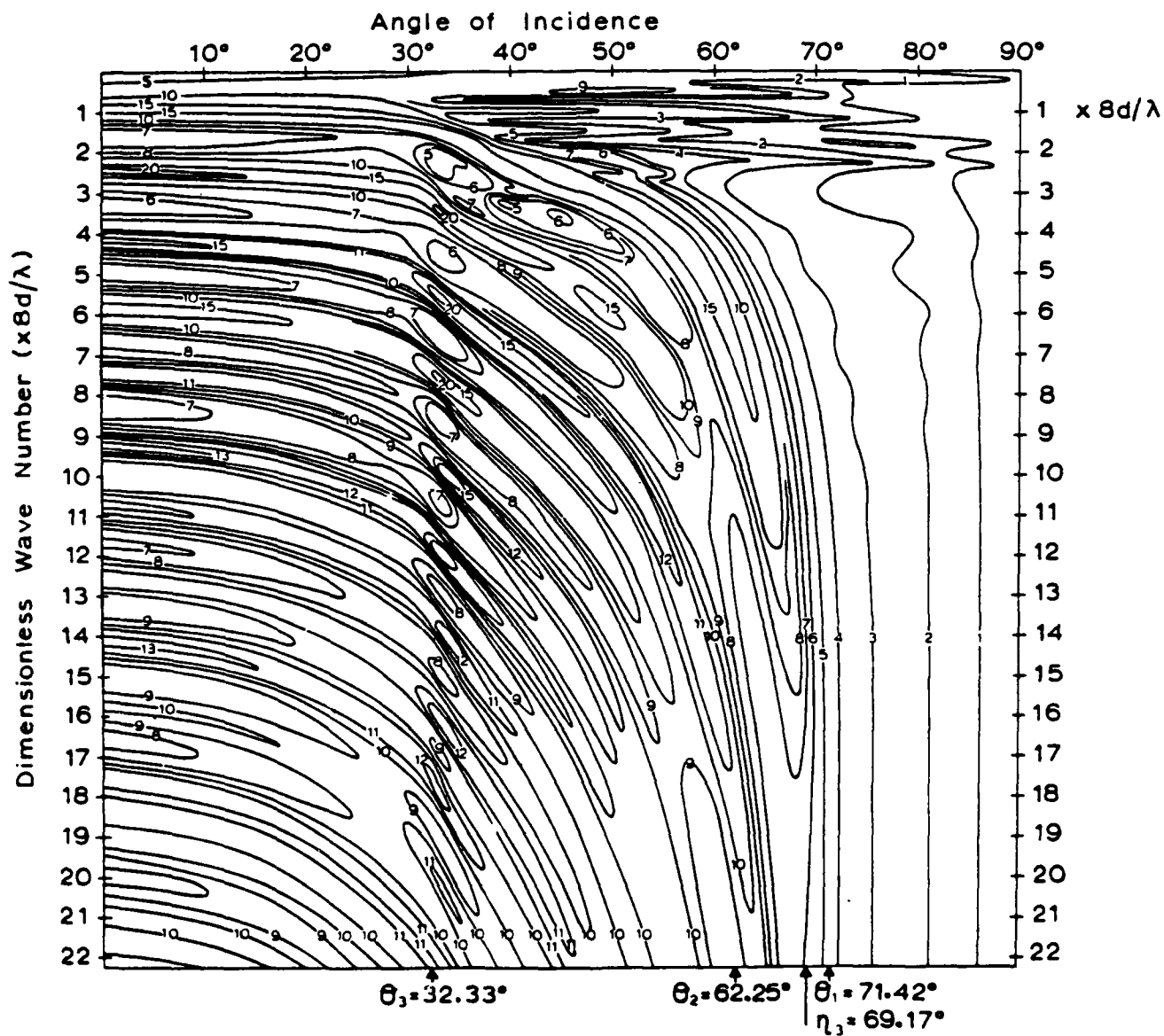
Figure 11-4. Reflection Loss in dB as a Function of the Angle of Incidence

and the Wavenumber - Model B

therefore be of interest to see how a low velocity layer on top of a more consolidated sediment will affect the reflectivity. To obtain a general picture of the reflection loss, this has been calculated for a porosity equal to 80 percent, at which the sediment sound velocity is minimum. The resulting iso-loss curves are shown in figure 11-5 and the usual system of ridges and valleys are noticeable. Two marked zones with very high losses are observed near grazing and correspond to an extension of the quarter-wave valleys. These are caused by the trapping of waves in the upper layer as already discussed in chapter 9.

Figure 11-6 shows the reflection loss as a function of frequency and porosity for angles of incidence of 0°, 60° and 80°. The 100-percent porosity case is included for completeness and corresponds to pure water.

ANGLE OF INCIDENCE
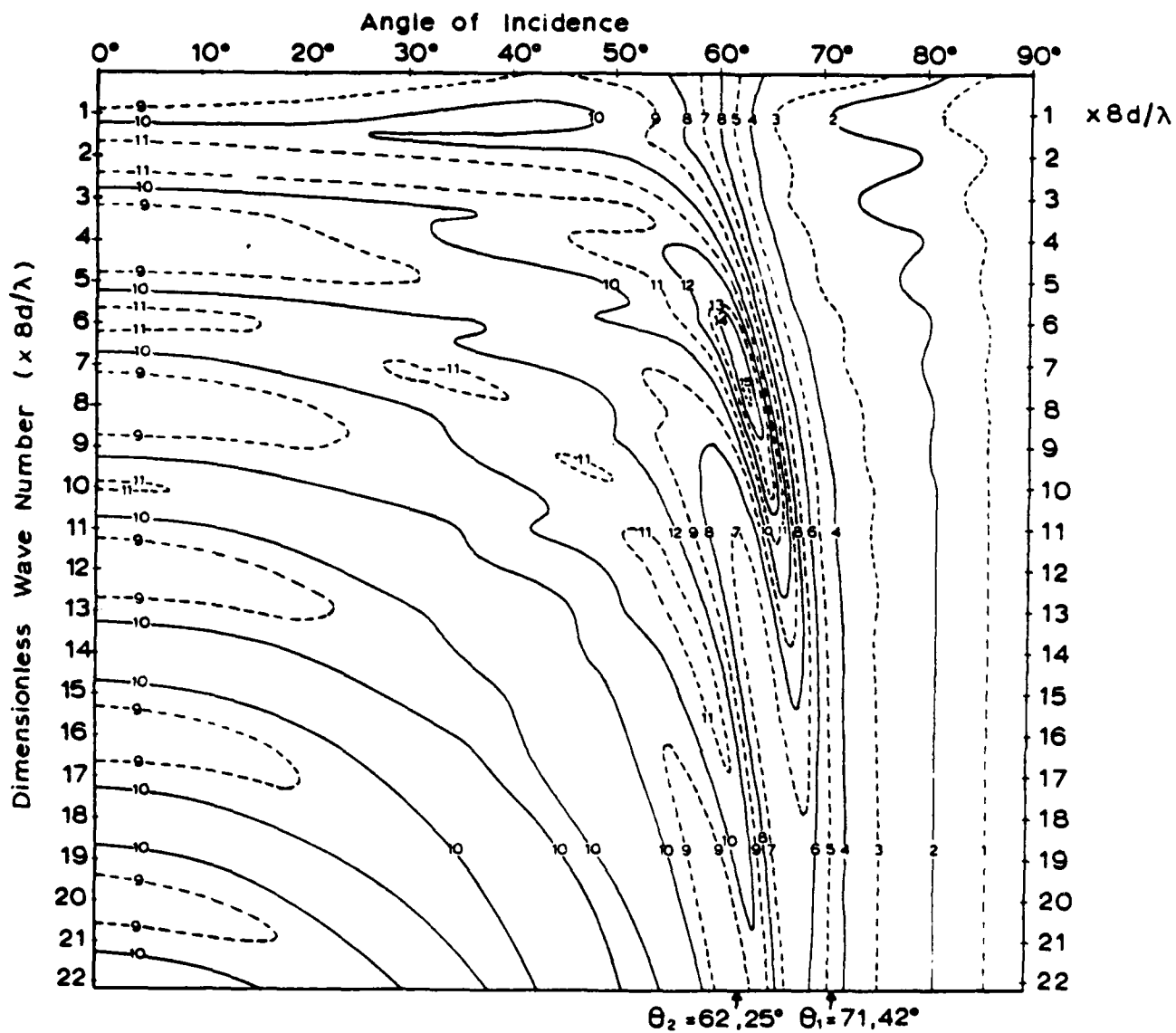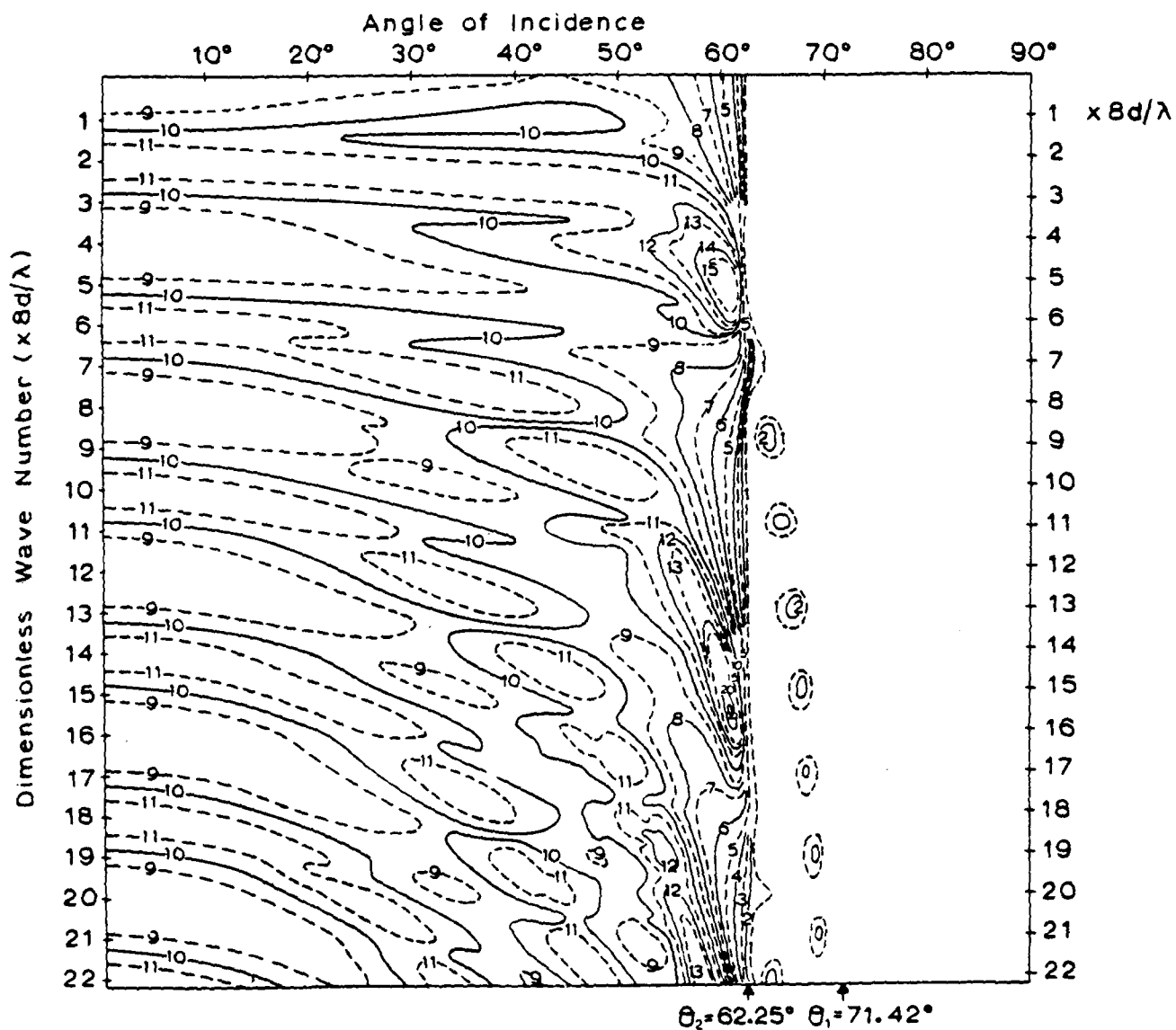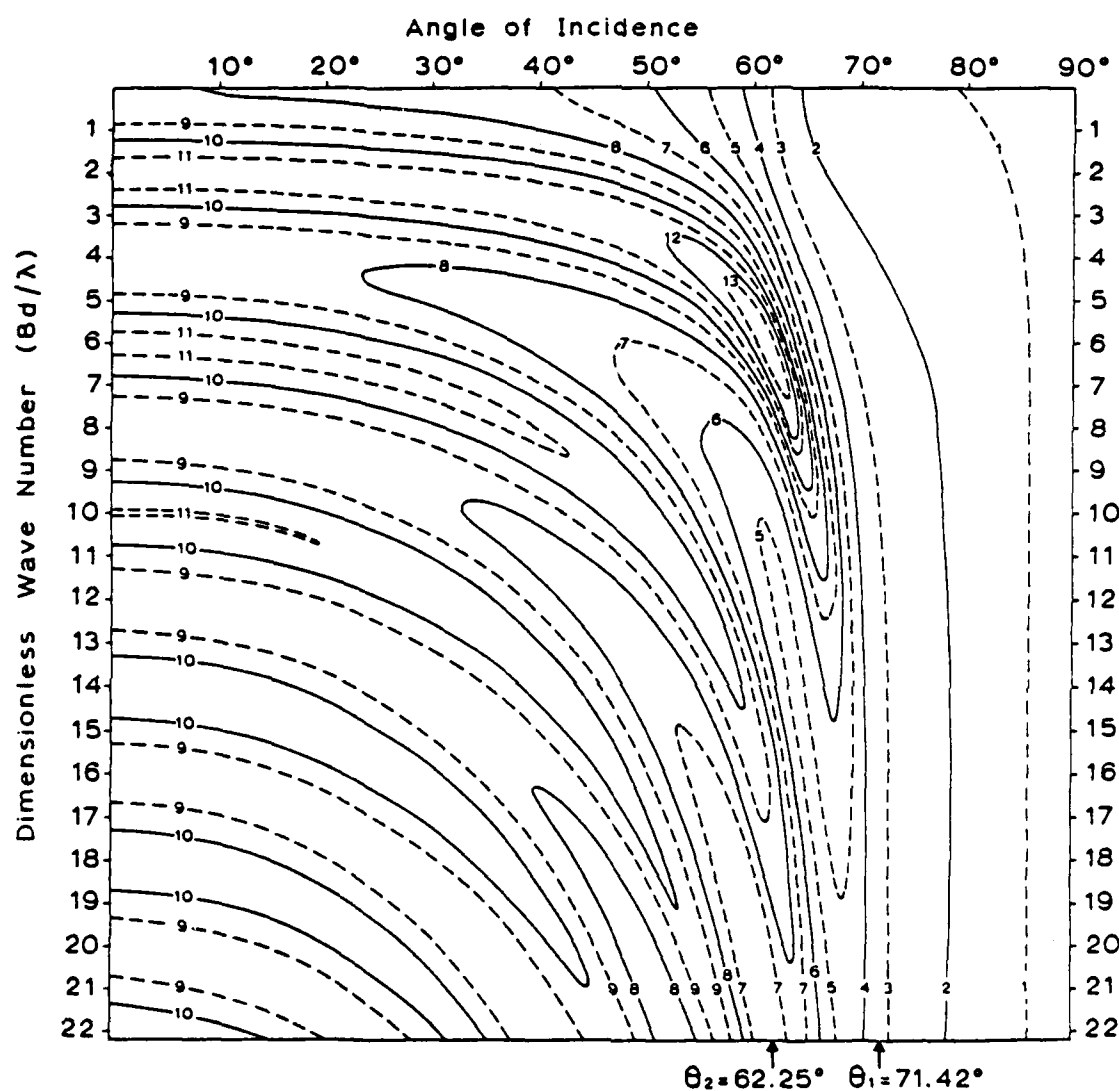

Figure 11-5. Reflection Loss in dB as a Function of the Angle of Incidence

and the Wavenumber - Model C

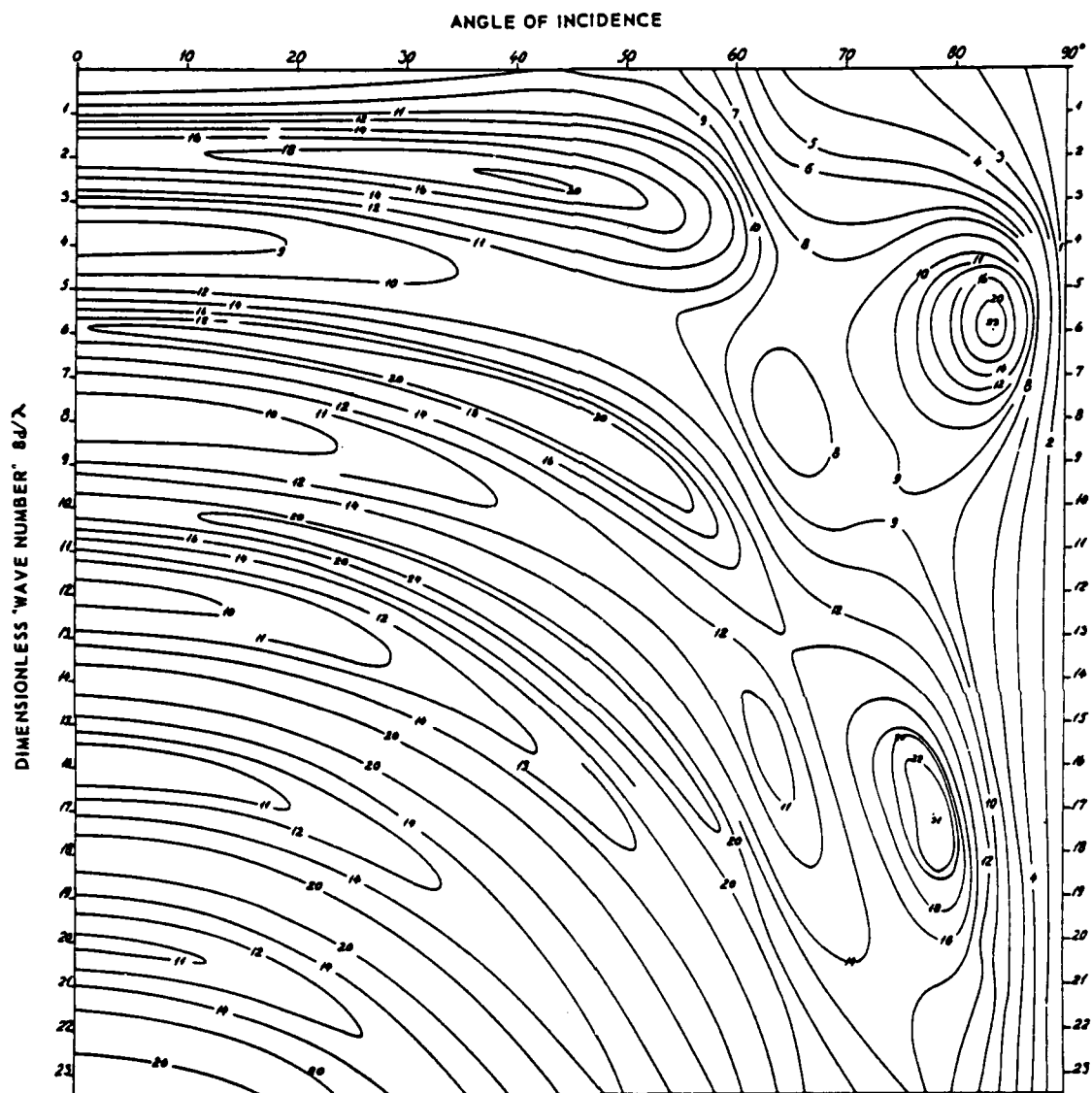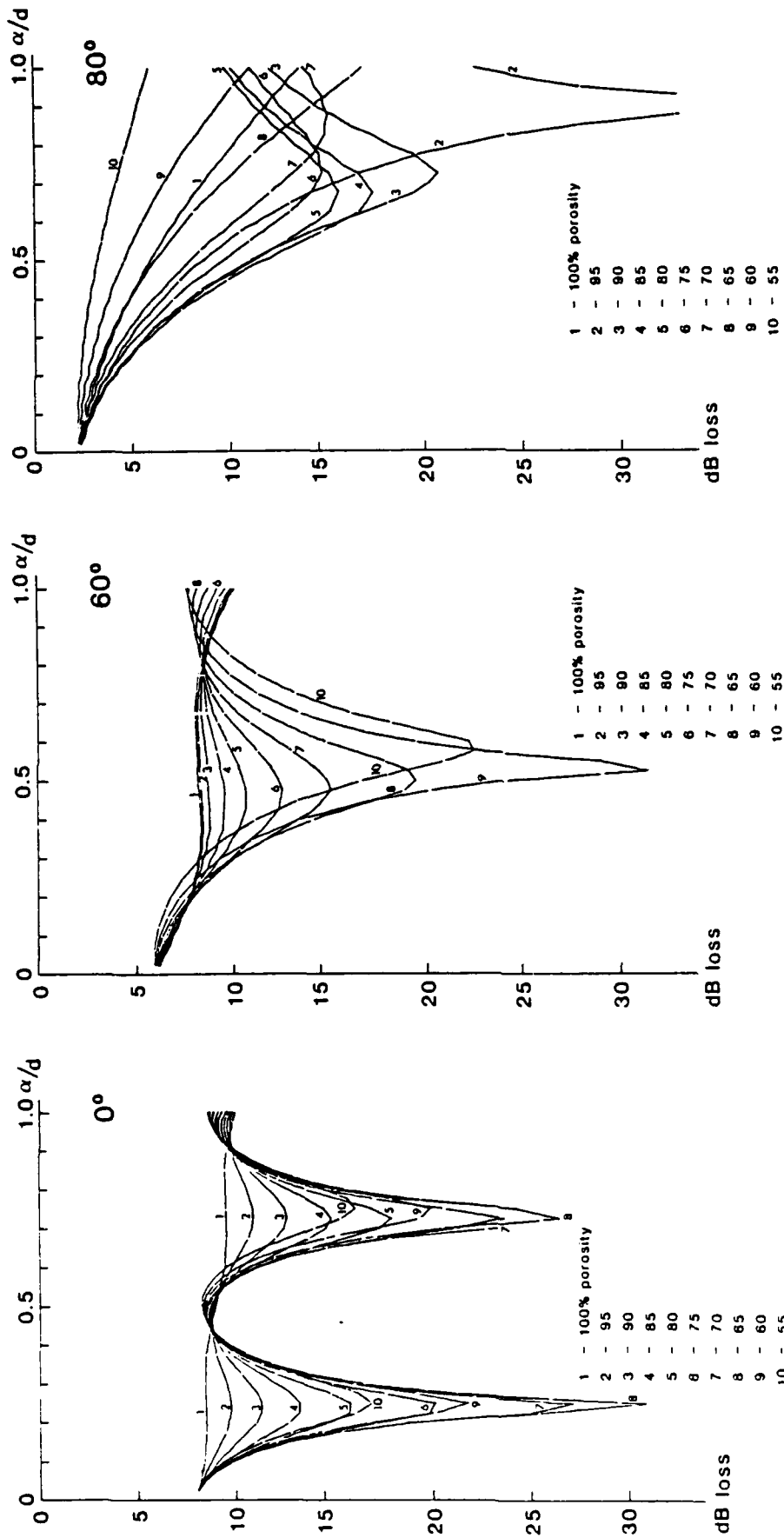Figure 11-6. Reflection Loss as a Function of Frequency

CHAPTER 12

IMPULSE RESPONSE

In the preceding chapter, we have described the bottom by its complex reflection coefficient $R(\omega)$ for a given angle of incidence as a function of frequency and treated it as a linear and time invariant system. Another way to describe such a linear system is by the impulse response in the time domain defined as the reflected signal for an incident delta function $\delta(t)$. For the delta function, also called the Dirac pulse, there exists the Fourier pair $\delta(t) <-> 1$. The impulse response h(t) is therefore determined by the well known Fourier integral:

$$h(t) = \frac{1}{2\pi} \int_{-\infty}^{\infty} R(\omega) \, e^{i\omega t} \, d\omega \qquad (12-1)$$

In the case of a single half-space as reflector, the reflection coefficient can be written as follows:

$$R(\omega) = \begin{cases} A_0 \cdot e^{i\theta_0} & \omega > 0 \\[2mm] A_0 \cdot e^{-i\theta_0} & \omega < 0 \end{cases}$$

or, using the signum function sgn ω, as:

$$R(\omega) = A_0 \cdot e^{i\theta_0 \, \mathrm{sgn}\, \omega} = A_0 (\cos \theta_0 + i \sin \theta_0 \, \mathrm{sgn}\, \omega)$$

which inserted in equation (12-1), gives

$$h(t) = A_c \left[\cos \theta_0 \frac{1}{2\pi} \int_{-\infty}^{\infty} e^{i\omega t} \, d\omega + \sin \theta_0 \frac{1}{2\pi} \int_{-\infty}^{\infty} i \, \mathrm{sgn}\, \omega \, e^{i\omega t} \, d\omega \right]$$

From the Fourier pairs,

$$\delta(t) <-> 1$$

and

$$1/\pi \cdot t <-> -i \cdot \mathrm{sgn}\, \omega$$

we obtain:

$$h(t) = A_0 \cdot \cos \theta_0 \cdot \delta(t) - A_0 \frac{\sin \theta_0}{\pi t}$$

which is shown in figure 12-1.
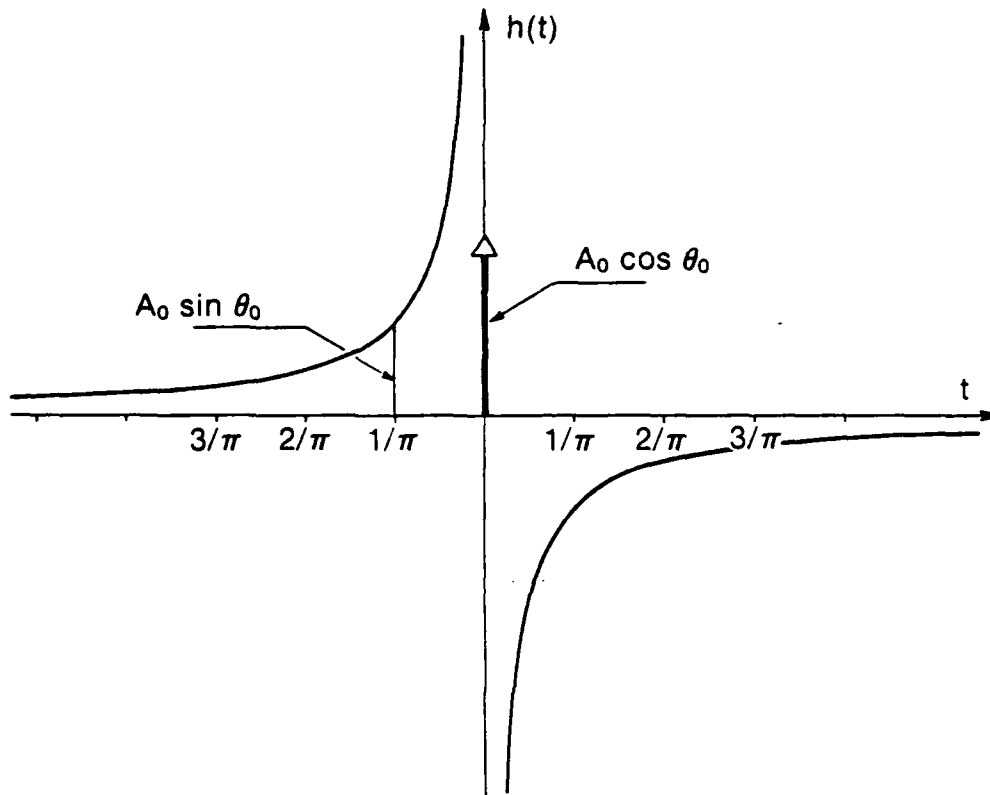
Figure 12-1. Impulse Response for a Half-Space Model

If there is no damping present, θ will be zero for angles of incidence less than the critical angle; hence, the impulse response is represented by the delta pulse at zero time. Only after the critical angle will there exist a phase shift causing the hyperbolic term in the impulse response.

In the case of a general multilayered bottom, $R(\omega)$ is so complicated that the Fourier integral has to be calculated numerically. This means that it is necessary to truncate the integral at a frequency high enough for the remainder to be ignored. But for $\omega \to \infty$, there still exists a finite reflection loss, so

any termination of the integral will cause a serious truncation error. To avoid this difficulty we remove from the reflection coefficient function the asymptotic value that corresponds to the case where the upper layer is acting as a half-space reflector:

$$R\,(\omega) = R'\,(\omega)\ + T\,(\omega),$$

where

$$T\,(\omega) \to 0 \text{ for } \omega \to \infty.$$

Thus, the impulse response can be written as:

$$h(t) = \text{Re}\,[R\,(\infty)]\,\delta\,(t) - \frac{\text{Im}\,[R\,(\infty)]}{\pi\,t} + \frac{1}{\pi}\int_0^{\omega_0} T(\omega)\,e^{i\omega t}\,d\omega$$

where Re[ ] and Im[ ] are, respectively, the real and imaginary parts. The last integral can now be calculated by truncating at ω_0, such that $T\,(\omega) \ll 1$. In the case where no damping is present this procedure will not work, since $T\,(\omega)$ will keep oscillating even for $\omega \to \infty$ and it will be necessary to use a proper frequency window such as discussed later in chapter 14.

If one is considering the situation where the angle of incidence is sufficiently small such that no critical angle will occur in a layered bottom, the impulse response can be obtained in the following way. Using the formula for the reflection coefficient for a two-layer model obtained as a sum of single reflections as given in chapter 8, we have:

$$R\,(\omega) = r_{01} +$$
$$t_{01}\cdot r_{12}\cdot t_{10}\cdot e^{-2ik_1\,d_1\cos\theta_1} +$$
$$t_{01}\cdot r_{12}\cdot r_{10}\cdot t_{10}\cdot e^{-4ik_1\,d_1\cos\theta_1} + \ldots,$$

where $2\cdot k_1\cdot d_1\cdot \cos\theta_1 = (2d_1\cdot\cos\theta_1/\alpha_1)\cdot\omega$ is the phase shift in the layer.

The Fourier inversion can now be made on each term. Using the following pairs

$$\delta(t) <\text{-}> 1$$

$$f(t - t_0) <\text{-}> F(\omega)\, e^{-it_0\omega}$$

with

$$f(t) <\text{-}> F(\omega)$$

the impulse response becomes:

$$h(t) = r_{01} \cdot \delta(t) +$$
$$t_{01} \cdot r_{12} \cdot t_{10} \cdot \delta\left(t - \frac{2d_1 \cos\theta_1}{\alpha_1}\right) +$$
$$t_{01} \cdot r_{12} \cdot r_{10} \cdot r_{12} \cdot t_{10} \cdot \delta\left(t - \frac{4d_1 \cos\theta_1}{\alpha_1}\right) + \ldots$$

which is a sequence of delta pulses separated from each other by the travel time $2d_1 \cdot \cos\theta_1/\alpha_1$, a result one would expect.

At this point it is also possible to get an idea of the influence of the attenuation on a separate pulse by introducing the complex wavenumber $k' = k(1 - i\cdot\varepsilon)$. The phase shift now becomes:

$$e^{-2ik_1' d_1 \cos\theta_1} = e^{-2ik_1 d_1 \cos\theta_1} \cdot e^{-2k_1 \varepsilon d_1 \cos\theta_1} =$$

$$e^{-i(2d_1 \cos\theta_1/\alpha_1)\omega} \cdot e^{-(2d_1 \cos\theta_1 \cdot \varepsilon/\alpha_1) \cdot i\omega}$$

The Fourier transform is then carried out by the use of the pairs

$$f(t) <\text{-}> F(\omega)$$

$$F(t) <\text{-}> 2 \cdot \pi \cdot f(-\omega)$$

and

$$e^{-\beta |t|} <\text{-}> 2\beta/(\beta^2 + \omega^2)$$

resulting in, for example for the second pulse, the following form:

$$t_{01} \cdot r_{12} \cdot t_{10} \cdot \frac{d_1 \cos\theta_1\, \varepsilon/\alpha_1}{\pi \cdot [4(d_1 \cos\theta_1 \cdot \varepsilon/\alpha_1)^2 + (t - 2d_1 \cos\theta_1/\alpha_1)^2]}$$

In this case it is not a delta pulse, but a smaller, "Gaussian-looking" pulse that is obtained; thus, increased attenuation will decrease the peak amplitude but widen the pulse. Had the attenuation in the water been taken into account, the reflection from the first interface would not have been a perfect delta pulse but a finite pulse like the reflection from the second interface.

To illustrate the technique, the impulse response has been calculated for the same three-layer model (B), used in chapter 11, for 0°, 40°, 60° and 80° angles of incidence. The results are shown in figures 12-2 to 12-5.

Looking, for example, at figure 12-3, we notice the following reflections: first, the delta pulse and the hyperbolic term from the surface, then the Gaussian-looking pulse from the second interface. Because the critical angle for the half-space is 32.3°, the reflection from the third interface will involve phase shift, which gives the pulse from this layer an inverted look. The next pulse to be seen on the figure occurs at $t \approx 4.5$ and is caused by the reflection of the previous pulse from the first and second interfaces before leaving this layer through the first interface. The pulse will have the same polarity as the incident because of an additional reflection from the first interface separating a higher impedance from a lower impedance. The following pulses are difficult to trace exactly due to the repeated influence on the phase shift.

The impulse response is a very useful way of describing the reflectivity and often is much easier to comprehend than the complex reflection coefficient when trying to deduct the characteristics of the bottom layering.

Figure 12-2. Impulse Response for a Three-Layer Model, 0° Angle of Incidence

Figure 12-3. Impulse Response for a Three-Layer Model, 40° Angle of Incidence

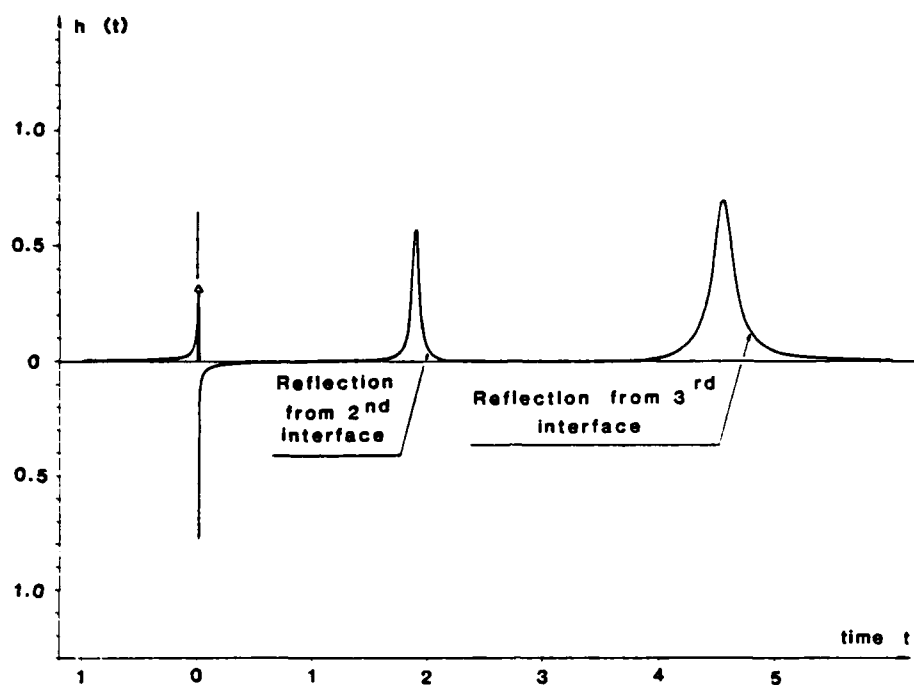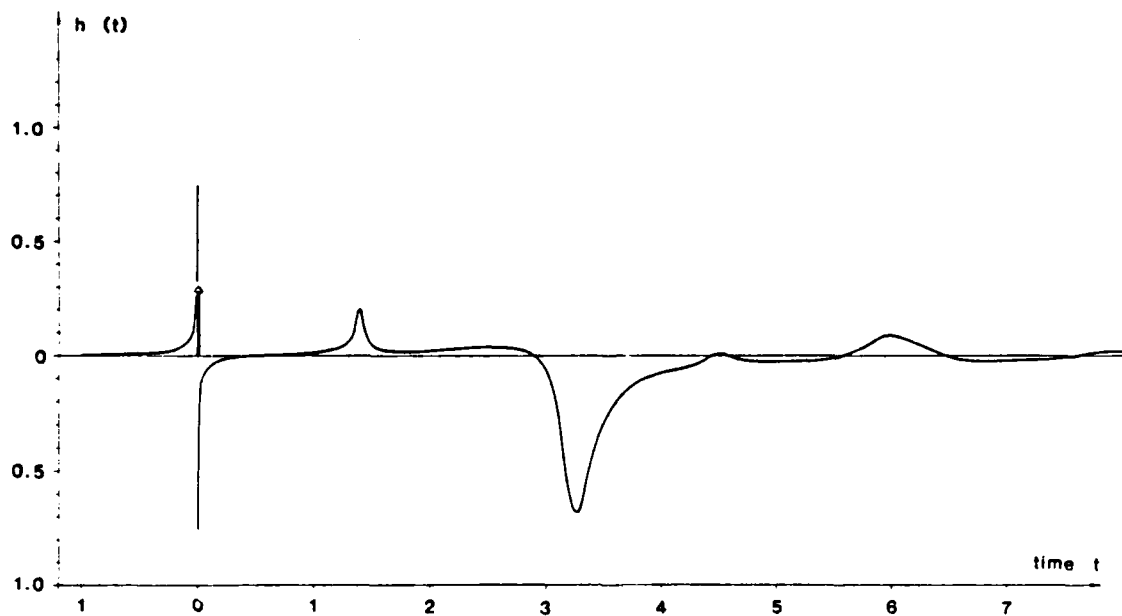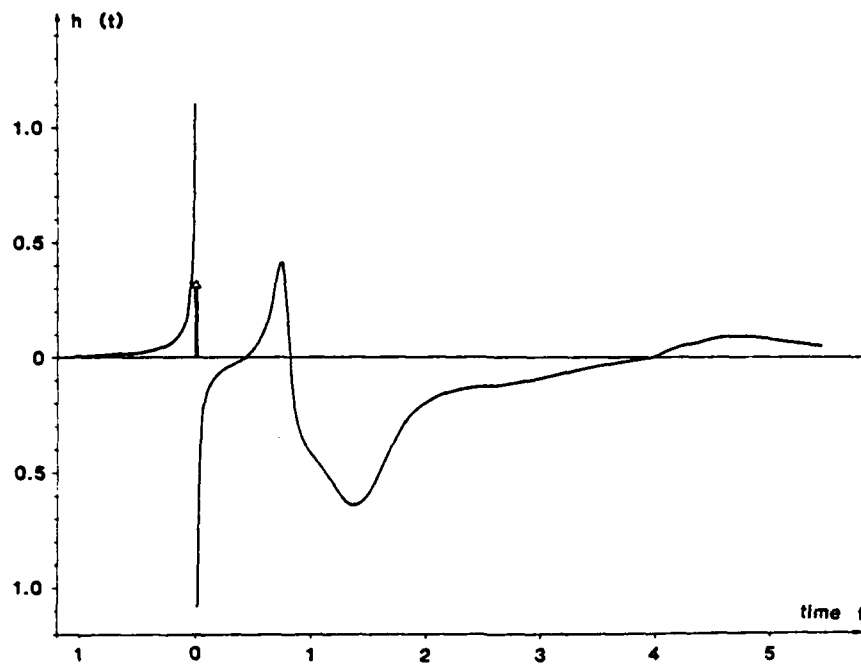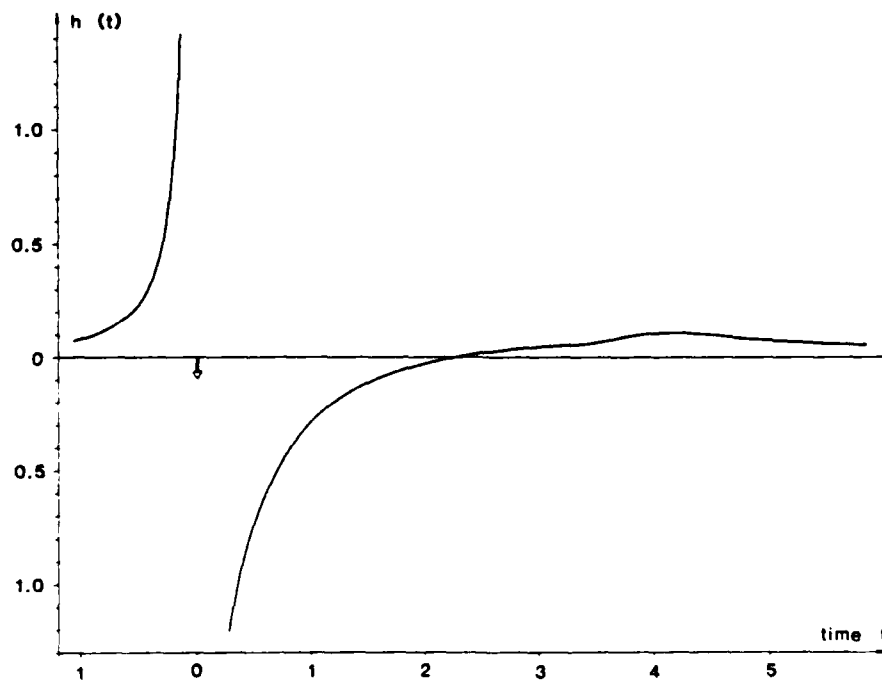Figure 12-4. Impulse Response for a Three-Layer Model, 60° Angle of Incidence

Figure 12-5. Impulse Response for a Three-Layer Model, 80° Angle of Incidence

CHAPTER 13

PERIODIC LAYERS

Analysis of hundreds of sediment cores taken from both the Atlantic and the Mediterranean shows that two distinct types of deep sea sediment are found. One consists of rather homogeneous clay, which has been deposited slowly and continuously (so-called pelagic sediments). The other consists of layers of clay mixed with sand or silt deposited suddenly by turbidity currents. Turbidity sedimentation is a frequent type in the Mediterranean and in the Atlantic. An inspection of the core sections very often indicates a clearly marked systematic change between clay and sand, giving certain parts of the core a periodic structure. It is of interest to study these conditions in more detail, since we shall see that periodic layers of quarter-wave thickness are one of the few cases where very high reflectivity exists over a finite frequency band.

Let us start by rewriting the transfer matrix A for liquid layers to a form more convenient for our purpose. From chapter 8, we have:

$$
\begin{bmatrix} \dot{w}/c \\ \sigma \end{bmatrix}_m = \begin{bmatrix} \cos P_m & i a_m (\rho_m c^2)^{-1} \sin P_m \\ i \rho_m c^2 a_m^{-1} \sin P_m & \cos P_m \end{bmatrix} \begin{bmatrix} \dot{w}/c \\ \sigma \end{bmatrix}_{m-1}
$$

which by the use of the values for c and a can be written as:

$$
\begin{bmatrix} \dot{w} \\ \sigma \end{bmatrix}_m = \begin{bmatrix} \cos P_m & i \dfrac{1}{Z_m} \sin P_m \\ i Z_m \sin P_m & \cos P_m \end{bmatrix} \begin{bmatrix} \dot{w} \\ \sigma \end{bmatrix}_{m-1} \qquad \text{or} \quad \overline{S}_m = \overline{\overline{A}}_m \cdot \overline{S}_{m-1}
$$

with
$$ Z_m = \frac{\rho_m \cdot \alpha_m}{\cos \theta_m} $$

being the impedance for the m layer. It is easy to prove that the determinant of this matrix is equal to unity, a fact due to the assumption of no attenuation in the medium.

By relating the boundary condition vector for the lower half-space interface and the layer-water interface through the new A matrices and by introducing $Z_n = -\sigma_n/\dot{w}_n$ and $Z_0 = -\sigma_0/\dot{w}_0$ as the impedances for the lower half-space and the total layering respectively, we get after some calculations:

$$R = \frac{(-a_{21} + a_{22} Z_n) - (a_{11} - a_{12} Z_n) Z_0}{(-a_{21} + a_{22} Z_n) + (a_{11} - a_{12} Z_n) Z_0} \qquad (13-1)$$

which expresses the reflection coefficient R by the half-space and water impedances and by the coefficients a_{ij} for the layering (excluding half-space) product matrix A.

Consider now a bottom built up of a succession of homogeneous sand and clay layers with markedly different acoustic parameters causing an alternation between higher and lower impedances. There will therefore be two types of A matrices, A_1 and A_2, one corresponding to sand and one to clay. The product matrix for such a double layer is:

$$\bar{\bar{m}} = \begin{bmatrix} \cos P_1 \cos P_2 - \dfrac{Z_2}{Z_1} \sin P_1 \sin P_2 & i(\dfrac{1}{Z_2}\cos P_1 \sin P_1 + \dfrac{1}{Z_1}\cos P_2 \sin P_1) \\ i(Z_1 \cos P_2 \sin P_1 + Z_2 \cos P_1 \sin P_2) & \cos P_1 \cos P_2 - \dfrac{Z_1}{Z_2} \sin P_1 \sin P_2 \end{bmatrix}$$

which is the transfer matrix for a single period (a double layer) in the layering.

The transfer matrix for N equal double layers is then:

$$\bar{\bar{a}} = \bar{\bar{m}} \cdot \bar{\bar{m}} \cdot \bar{\bar{m}} \cdot \bar{\bar{m}} \cdot \ldots \bar{\bar{m}}. \quad \text{N times}$$

Since A is unity, the elements in a can be expressed explicitly by the use of Chebyshev polynomials in the following way:

$$a_{11} = m_{11} U_{N-1}(x) - U_{n-2}(x)$$
$$a_{12} = m_{12} U_{N-1}(x)$$
$$a_{21} = m_{21} U_{N-1}(x)$$
$$a_{22} = m_{22} U_{N-2}(x) - U_{N-2}(x),$$

where $U_N(x)$ is the Chebyshev polynomial of second kind and N^{th} degree. The argument x is half of $\bar{\bar{m}}$'s trace and equal to

$$X = \cos P_1 \cos P_2 - \tfrac{1}{2} \left(\frac{Z_1}{Z_2} + \frac{Z_2}{Z_1} \right) \sin P_1 \sin P_2.$$

The first polynomials are $U(x) = 1$, $U(x) = 2x$, and the higher orders can be computed from the recurrence formula:

$$U_N(x) = 2x\, U_{N-1}(x) - U_{N-2}(x)$$

In the case where the acoustic thickness of the two layers are identical (which corresponds to equal phase shifts),

$P_1 = P_2 = P$ and $\bar{\bar{m}}$ reduces to:

$$\bar{\bar{m}} = \begin{bmatrix} \cos^2 P - \dfrac{Z_2}{Z_1} \sin^2 P & i\left(\dfrac{1}{Z_1} + \dfrac{1}{Z_2}\right) \cos P \sin P \\ i(Z_1 + Z_2) \cos P \sin P & \cos^2 P - \dfrac{Z_1}{Z_2} \sin^2 P \end{bmatrix}$$

When $P = \pi/2$ (which is the case when the thickness of the simple layer equals a quarter-wavelength), $\bar{\bar{m}}$ reduces further to the simple and symmetrical form:

$$\bar{\bar{m}} = \begin{bmatrix} -\dfrac{Z_2}{Z_1} & 0 \\ 0 & -\dfrac{Z_1}{Z_2} \end{bmatrix}$$

and

$$\bar{\bar{a}}_N = \begin{bmatrix} (-\dfrac{Z_2}{Z_1})^N & 0 \\[4mm] 0 & (-\dfrac{Z_1}{Z_2})^N \end{bmatrix}$$

The reflection coefficient is then, according to equation (13-1):

$$R = \frac{1 - (\dfrac{Z_2}{Z_1})^{2N}\dfrac{Z_0}{Z_n}}{1 + (\dfrac{Z_2}{Z_1})^{2N}\dfrac{Z_0}{Z_n}}$$

This is valid only at a frequency corresponding to the quarter-wave criterion in the original layers.

The analytical evaluation of R when the phase shift P is not equal to $\pi/2$ leads to rather complicated expressions. The following cases have therefore been computed numerically and the results given in graphical form using

$$\alpha_{sand} = 1.05, \ \alpha_{clay} = 0.95, \ \rho_{sand} = 1.8 \text{ and } \rho_{clay} = 1.4.$$

Figure 13-1 shows the vertical losses for $N = 1, 2, 3, 4, 6, 9$ and $0 \le P \le \pi$ with $P_1 = P_2 = P$.

To avoid confusion between the different curves, only the high reflection zone has been plotted at the highest values of N. We find a very characteristic, almost frequency-independent, low loss around $P = \pi/2$. Outside this region the losses are much higher and oscillate, with the number of oscillations increasing with N.

When using the condition of periodicity, it can be shown that when $N \to \infty$, one can find a finite interval around $P = \pi/2$ with zero loss and that the width of this high-reflectance is twice the arcsine of the local reflection coefficient $r = (Z_1 - Z_2)/(Z_1 + Z_2)$ between two single layers.
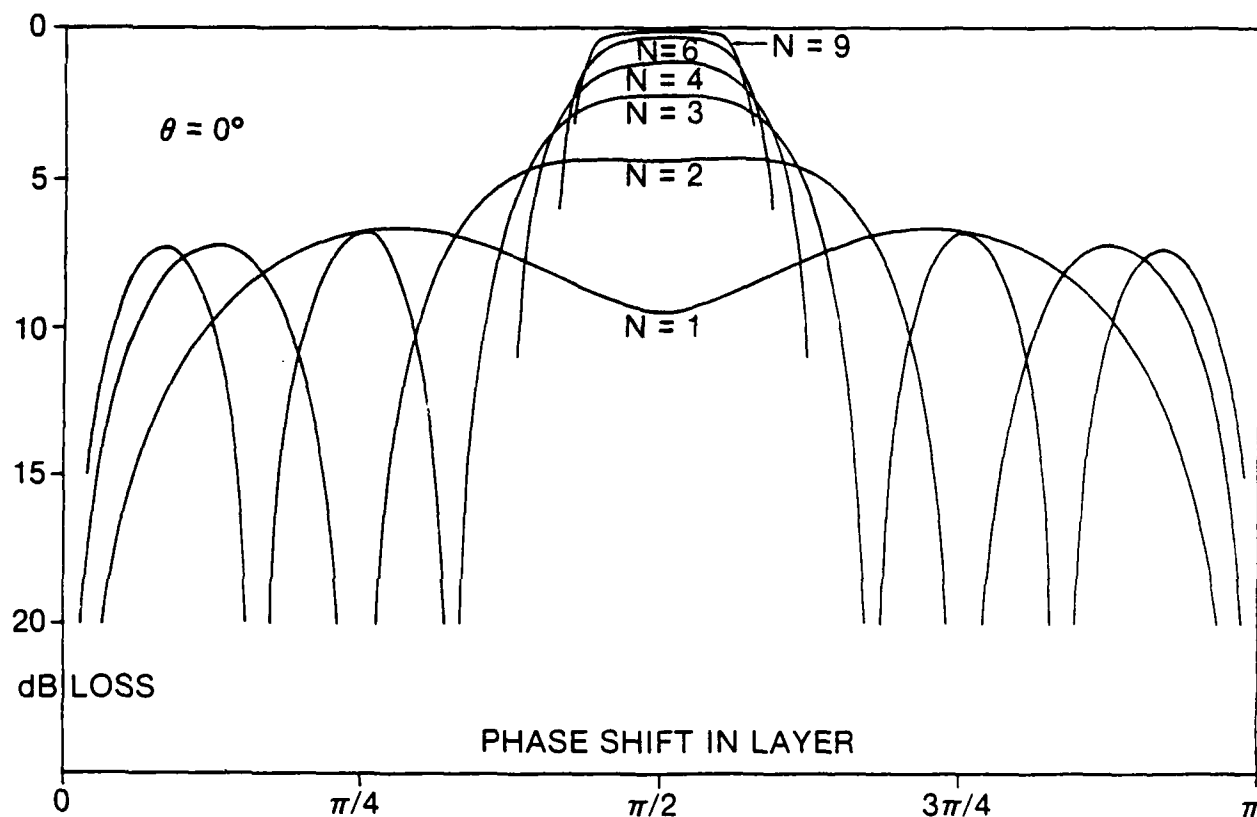
Figure 13-1. Reflection Loss in dB as a Function of Phase Shift
for Different Numbers of Layers

The influence on the angle of incidence is investigated for the case N = 3 and with the single layers matched in phase for vertical incidence. The results are given in figure 13-2. Apart from an expected shift of the high-reflectance zone towards higher frequencies, we notice that both the width of the zone and the reflectivity increase with an increasing angle of incidence.
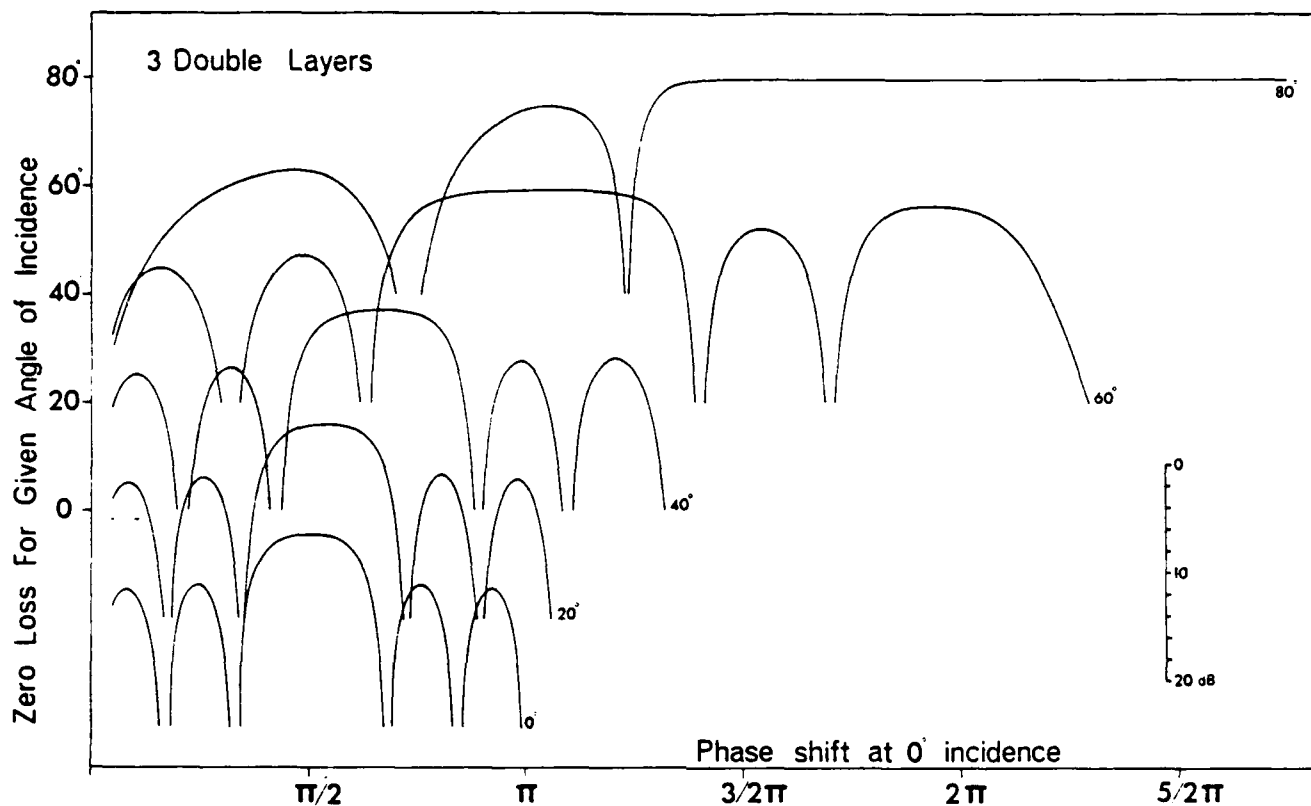
Figure 13-2. Reflection Loss in dB for N = 3 as a Function of Phase Shift
for Different Angles of Incidence

Until now we have only considered single layers of equal acoustic thickness
(same phase shift in both layers), a criterion that quite often is not exactly
met in nature.   We shall now study the effect of three double layers that are
similar but not exactly matched.   Figure 13-3 shows the minimum loss for the
first high- reflectance zone as a function of the ratio between acoustical
thicknesses.

Figure 13-3. Minimum Reflection Loss in dB for N = 3 as a Function of Different Ratios of Acoustic Thickness (Thickness of Double Layer Equal to $\lambda/2$)
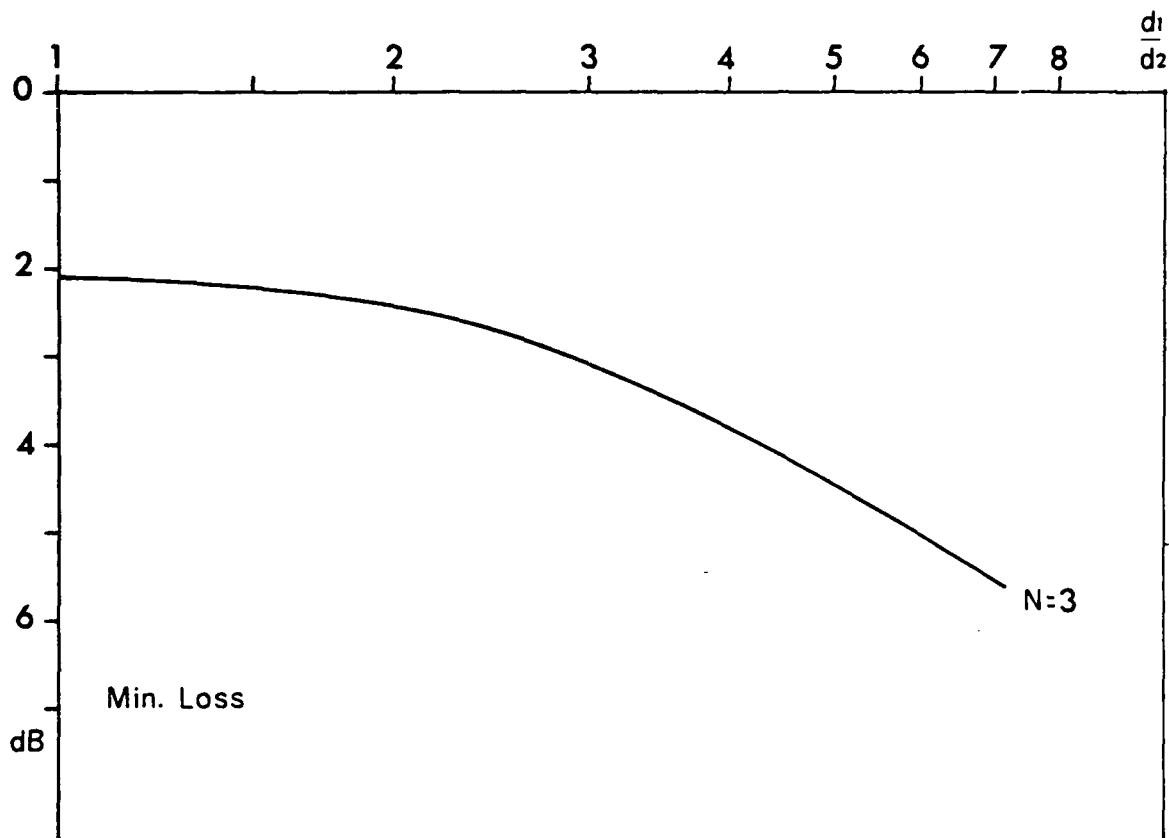
From the figure we notice a very important factor: even in the case of unmatched layers, high-reflectance zones exist when the thickness of the total double layer is equal to a half-wavelength. We can, therefore, perhaps conclude that, where a periodicity is found in the sub-bottom layering, low-loss frequency bands should be found by, for example, the use of broadband signals such at those from explosive sources.

One of the several areas where SACLANTCEN has made bottom reflectivity measurements is in the Tyrrhenian Abyssal Plain southwest of Naples. Figure 13-4 shows the reflection losses as a function of frequency and angle of

incidence. The losses are strongly oscillating except within a very marked band approximately 300 Hz wide where the losses are almost constant and in the order of 2 to 3 dB. The center frequency is about 1500 Hz at 18.3° angle of incidence. Correcting this to vertical incidence by cos 18.3°, we get f = 1430 Hz.

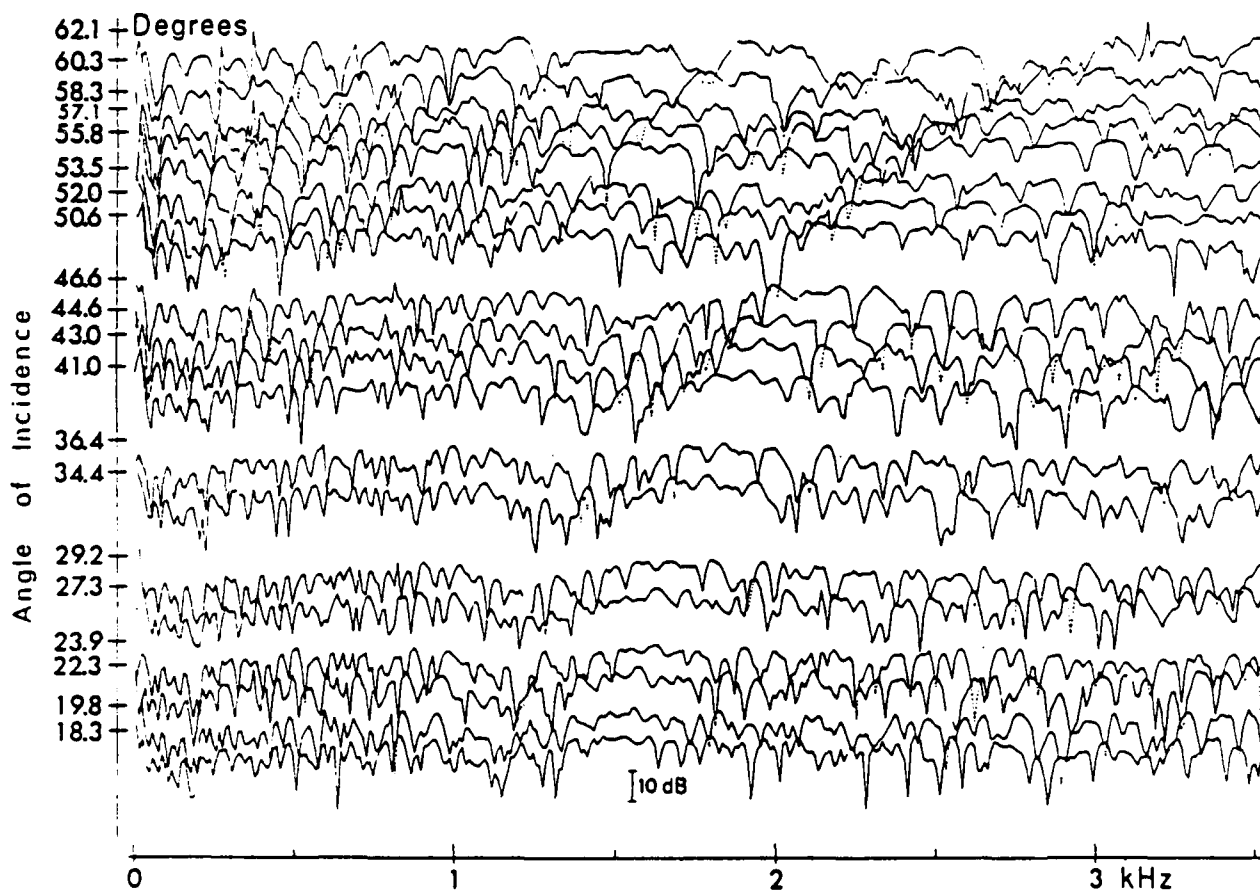Figure 13-4. Reflection Losses as a Function of Frequency for Different Angles of Incidence

Thus, it looks very much as if we were dealing with a system of periodic layers and an inspection of seven bottom cores taken within the reflecting area shows a marked layering. Analyzing the density, we obtain an average wavelength corresponding to a double layer on the order on 54 cm with a standard deviation

of 10 cm. We should, therefore, expect a high-reflectance zone corresponding to a wavelength of 108 cm = 54·2, which again corresponds to a frequency f = 1560/108 = 1450 Hz, an excellent agreement.

Such periodic structures play an important role in other fields of wave propagation. One example is the use of different coatings of optical devices, either to reduce or enhance reflectivity; another, the Bragg reflections of X-rays used in crystallographic research.

CHAPTER 14

MEASUREMENT OF BOTTOM REFLECTIVITY

The experimental determination of the reflection coefficient is not always a simple matter and many different techniques have been applied with varying results. The problem divides itself into two parts: one concerning the experimental set-up and the other concerning the analysis of the experimental data.

In the past some of the techniques used have been standing spherical wave interference methods or correlation techniques with random noise. However, they are not really practical in the true ocean with water depths up to several thousands of meters. The technique we will discuss in detail uses explosive sources and digital processing.

EXPERIMENTAL DETERMINATION OF THE REFLECTION COEFFICIENT

To measure the reflection coefficient over a wide frequency band and for angles of incidence from vertical to close to grazing, the following technique has been used by the SACLANTCEN during the past 20 years.

A receiving ship suspends a 750-meter vertical hydrophone string, while a source ship moves on a predetermined fixed course, launching explosive charges (500-1000 g TNT) set to explode at a depth of about 500 m. The launching schedule is arranged so that bottom grazing angles between 5° and close to 90° are covered.

The direct and reflected acoustic signals are received by the hydrophones in the string and recorded, in digital form, along with a radio pulse that is transmitted from the source ship at the moment of reception of the direct acoustic pulse. Acoustic travel times are computed from the radio signal, and

in connection with radar observations, used to determine the trial geometry. Figure 14-1 shows the experimental set-up.
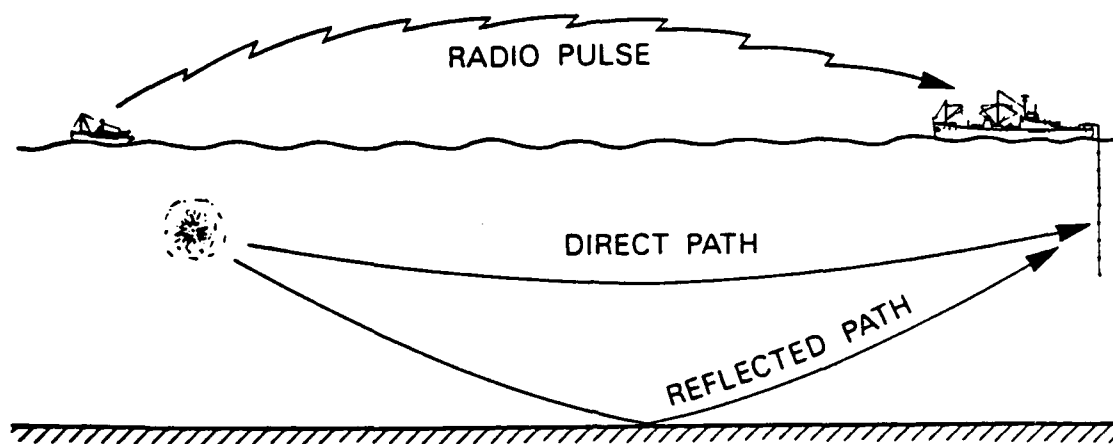
Figure 14-1. Experimental Set-Up

For each station occupied by the receiving ship, the following supporting environmental measurements are made:

a. bathymetry along source ship track

b. sound speed profiles

c. core samples

d. bottom stereo photographs.

REFLECTION-LOSS CALCULATIONS

Since the reflection coefficient at a layered bottom is frequency depen-dent, simple and direct calculations cannot be made and one has to use Fourier analysis techniques. Let $d(t)$ and $r(t)$ be the incident and reflected pulse close to the bottom, as seen in figure 14-2.

Figure 14-2. Ray Geometry

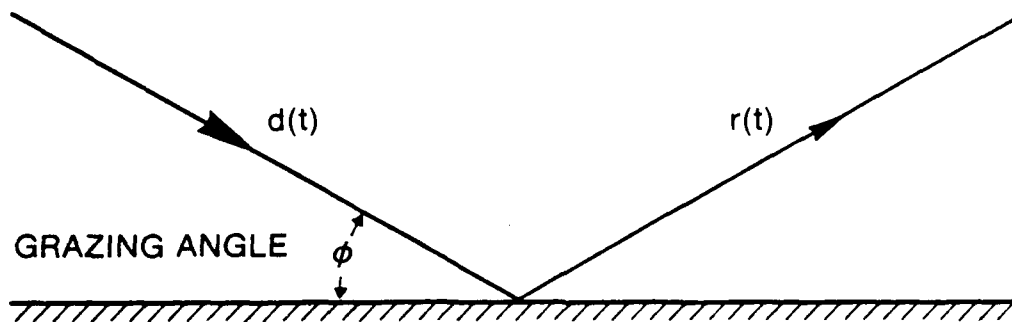The frequency-dependent reflection coefficient $H(\omega)$ is then obtained by deconvolving the reflected spectrum by the incident spectrum as:

$$H(\omega) = \frac{R(\omega)}{D(\omega)}$$

where R and D are the Fourier transforms of $r(t)$ and $d(t)$, as

$$R(\omega) = \int r(t)\, e^{-i\omega t}\, dt,$$
$$D(\omega) = \int d(t)\, e^{-i\omega t}\, dt.$$

The reflection loss is then defined as $L = -20 \log |H|$ dB. The impulse response $h(t)$ is then determined as discussed previously as the inverse Fourier transform of $H(\omega)$,

$$h(t) = \frac{1}{2\pi} \int H(\omega)\, e^{i\omega t}\, d\omega.$$

In the experiment, the direct and reflected pulses were not measured near the bottom but instead measured in the water column after they had both been attenuated along their propagation paths. The attenuation is the combined

spreading loss and the frequency-dependent absorption and is determined by ray tracing based on the measured sound-speed profiles.

Nominating the difference transmission loss in the water for a perfect reflecting boundary as

$$\Delta = TL_{Ref} - TL_{Direct},$$

the bottom loss is $BL = -20 \log \dfrac{R'(\omega)}{D'(\omega)} - \Delta(\omega),$

where $R'(\omega)$ and $D'(\omega)$ correspond to the Fourier transforms of the reflected and direct path of the received signal, for which an example is given in figure 14-3, along with their respective amplitude spectra. By dividing the Fourier transform of the reflected signal by the Fourier transform of the direct signal, the uncorrected reflection loss is obtained as shown on figure 14-4. The impulse response is then calculated from the lowpass filtered deconvolved signal. The result is also shown on figure 14-4 with the noisy nonfiltered impulse response.

Using the same hydrophones and recording channels for both the direct and reflected signals makes this technique self-calibrating, and the use of several hydrophones at different depths gives the capability to separate as many as possible of the received pulses at low grazing angles, down to a few degrees. Henceforth, we will use the grazing angle instead of the angle of incidence when presenting results, a practice common in ASW.

Figure 14-5 shows an example of the measured frequency-dependent losses at low and high grazing angles on a flat and smooth bottom. At high grazing angles, one notices the interference pattern caused by reflections from the different layers. Also, it should be noted that the lowest losses occur at
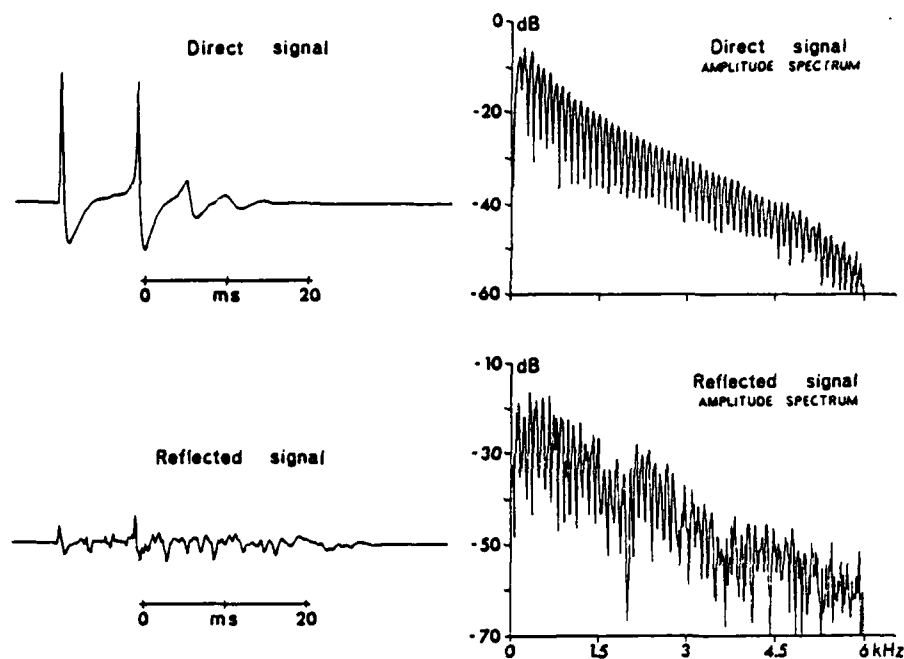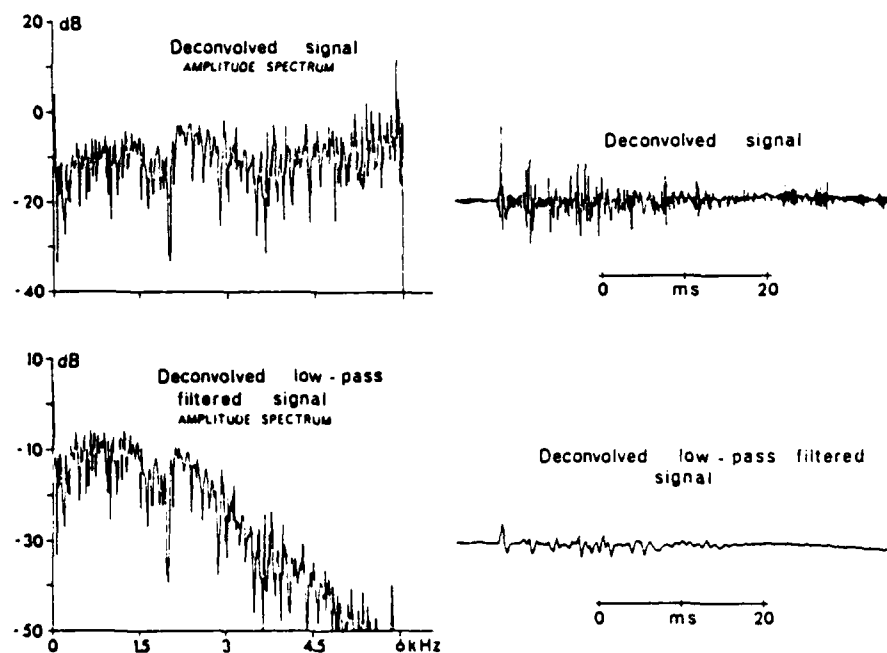
Figure 14-3. Direct and Reflected Signals

Figure 14-4. Deconvolved Impulse Response and

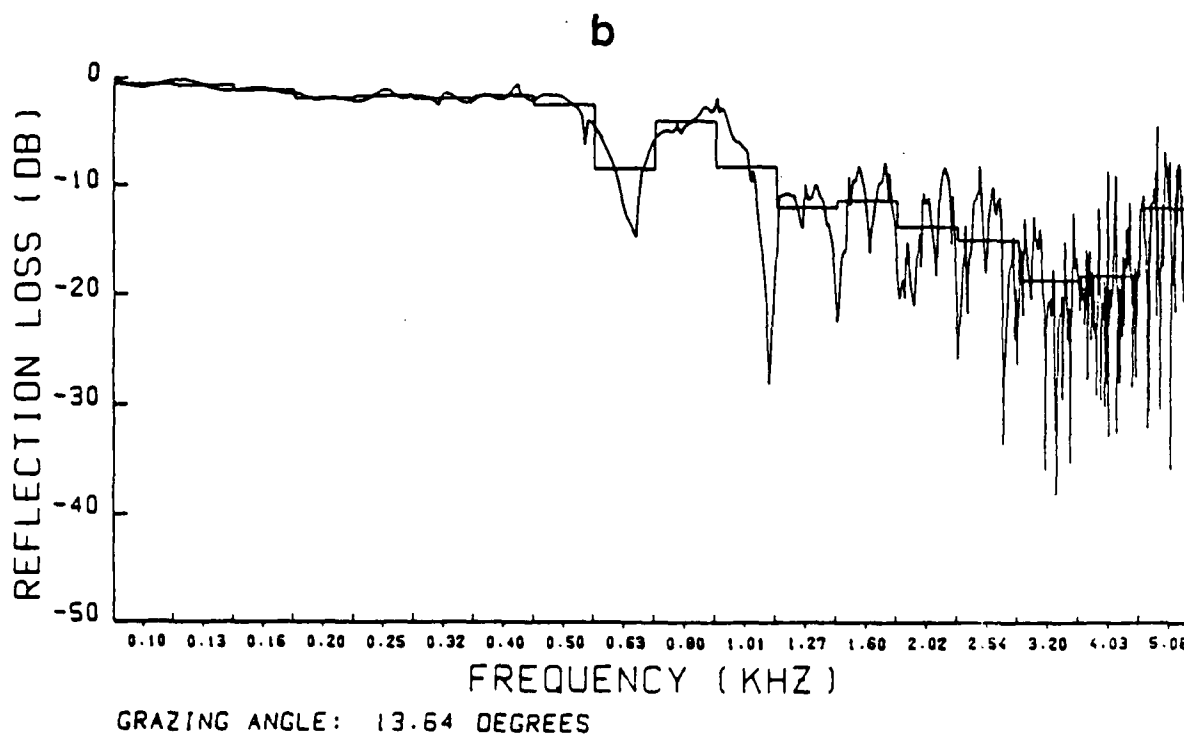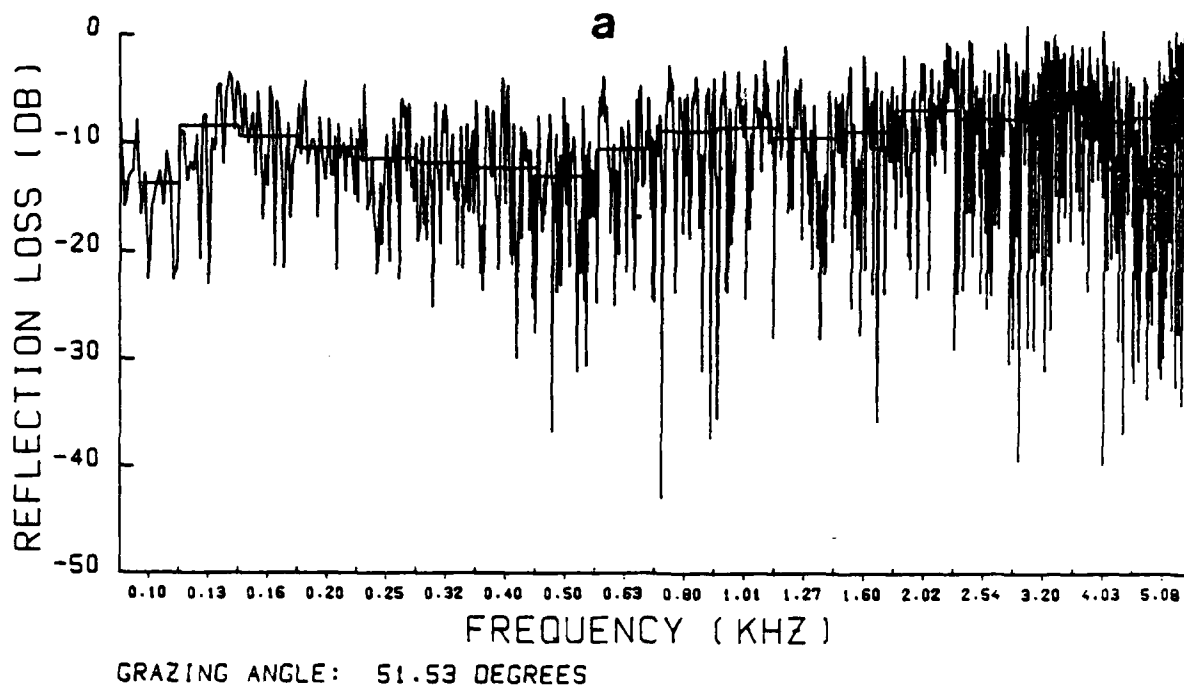Deconvolved Low-Pass Filtered Impulse Response

Figure 14-5.   Examples of the Measured Frequency-Dependent Reflection Loss

at High (a) and Low (b) Grazing Angles

higher frequencies because the reflections from shallow and thin layers are the most dominant. At low grazing angles, the picture changes to an almost perfect reflection of the lowest frequencies, due to one or several critical angles for deeper layers, whereas the high frequency part exhibits large losses due to an intromission angle in the shallower sediments.

The step functions superimposed on the loss curves are the 1/3-octave band levels obtained by mathematical filtering.

SPECIFIC SEA FLOOR ACOUSTIC RUNS

To illustrate the technique, we will take a look at three different cases from the Mediterranean as shown in figure 14-6. Reflections from a bottom consisting mainly of turbidity sediments, from a bottom consisting mainly of soft pelagic sediments, and from a rough bottom in a ridge area. The results are presented in three types of displays:

a. The impulse response with a 500-5000 Hz bandwidth for different grazing angles, using 80 and 20 ms time axes.

b. The reflection losses as isoloss contours in a frequency-angle plane calculated in 1/3-octave bands.

c. The reflection losses as a function of grazing angle calculated in octave bands.
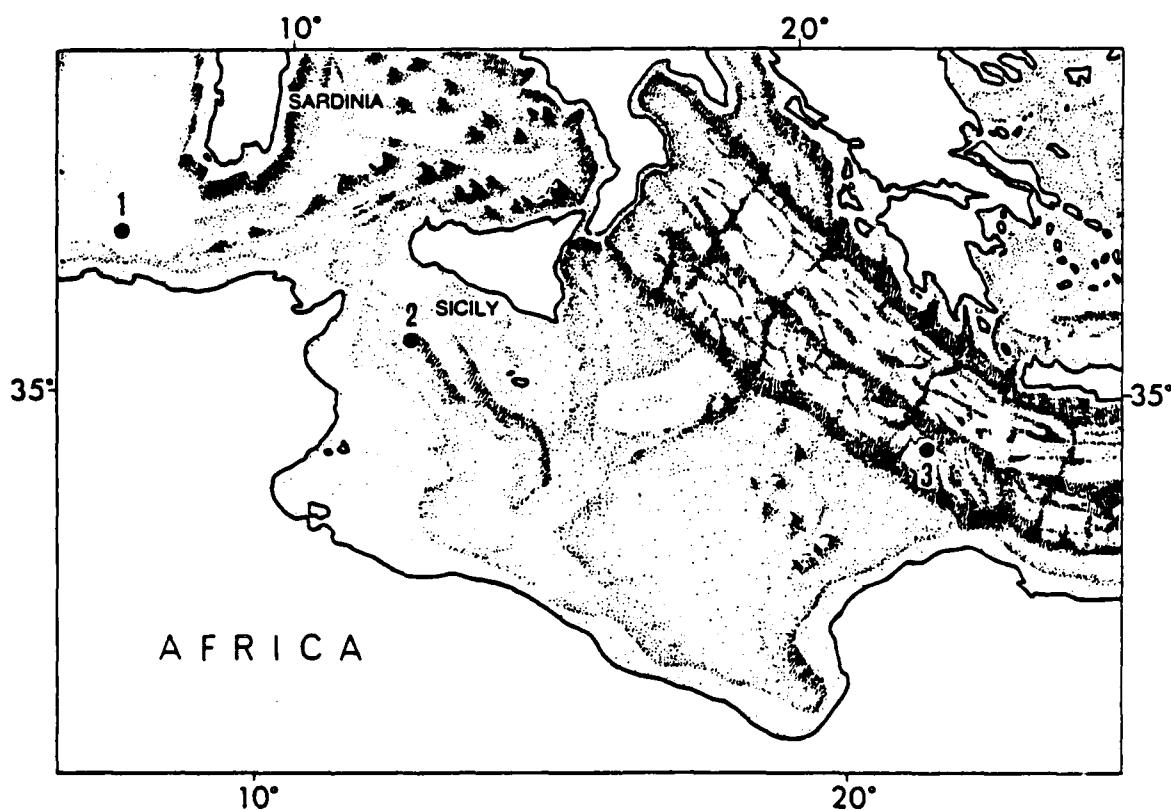
Figure 14-6. Positions of Acoustic Runs

Run 1. Southeastern Balearic Abyssal Plain

The Balearic Abyssal Plain is the most extensive abyssal plain in the Mediterranean. The station where the bottom reflectivity was measured is situated off eastern Algeria, on the southeastern part of this abyssal plain. Along the acoustic run, the water depth varied from 2630 to 2615 m with a flat sea floor. A core was taken at position 1 indicated in figure 14-6. The sediments consisted of fine-grained clays and carbonates interspersed with silt and sand deposits transported by turbidity currents, probably originated by the

steep Algerian continental slope. These turbidity layers are also very evident from the impulse responses shown on figure 14-7.

The reflection losses, as seen in figures 14-8 and 14-9, show a clear critical angle situation for low frequencies, as we would expect from the existence of the high sound-speed sand layer observed in the core. No evidence is seen of high loss due to an intromission angle. Only the first reflection from the water/sediment interface indicates an intromission angle seen from the 180° phase shift of the pulse at 13.5° grazing angle. This value corresponds to a sound-speed contrast of 0.98 and a density contrast of 1.4; such values are typical of unconsolidated sediments and were also observed during the subsequent runs over a flat bottom.

Very marked reflections occur from layers A, B and C, situated at depths of 5 m, 12.5 m and 34 m. As the grazing angle diminishes, the pulse is critically reflected from these layers, forming high-amplitude phase-distorted pulses that dominate the impulse response at small angles. Note also a possible deep-refracted arrival showing at 33° grazing caused by the velocity gradient in the sub-bottom.

Run 2. Pantelleria Basin

This acoustic run was conducted in the Pantelleria Basin, situated southeast of the island of Pantelleria. The basin is approximately 90 km long and 30 km wide with a water depth of about 1300 m. A core (about 7 meters) was taken in the area of position 2 as shown in figure 14-6. It consisted of soft unconsolidated sediments with three layers of silt/sand-type turbidity sequences.
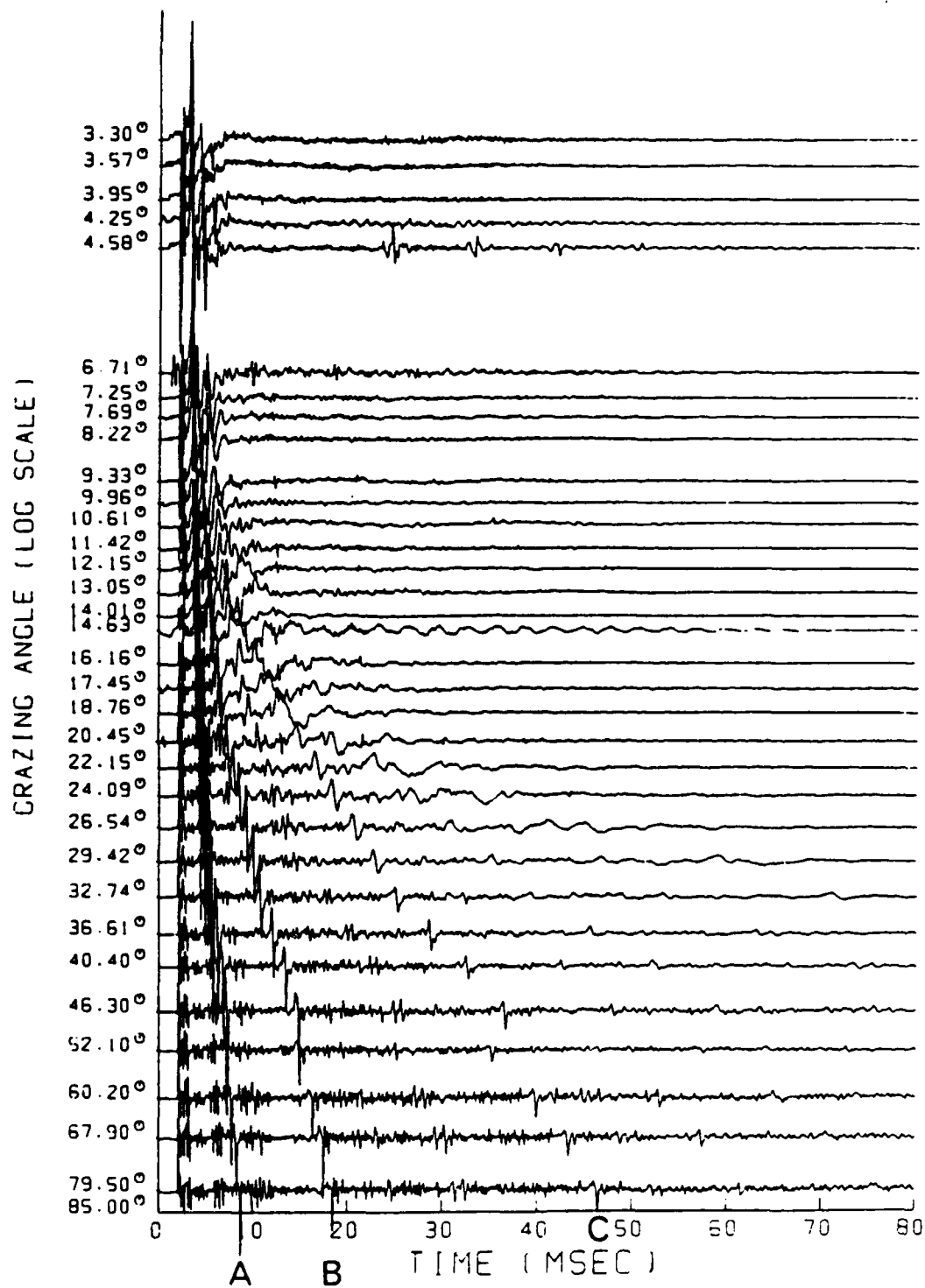
Figure 14-7a. Impulse Response for Station 1
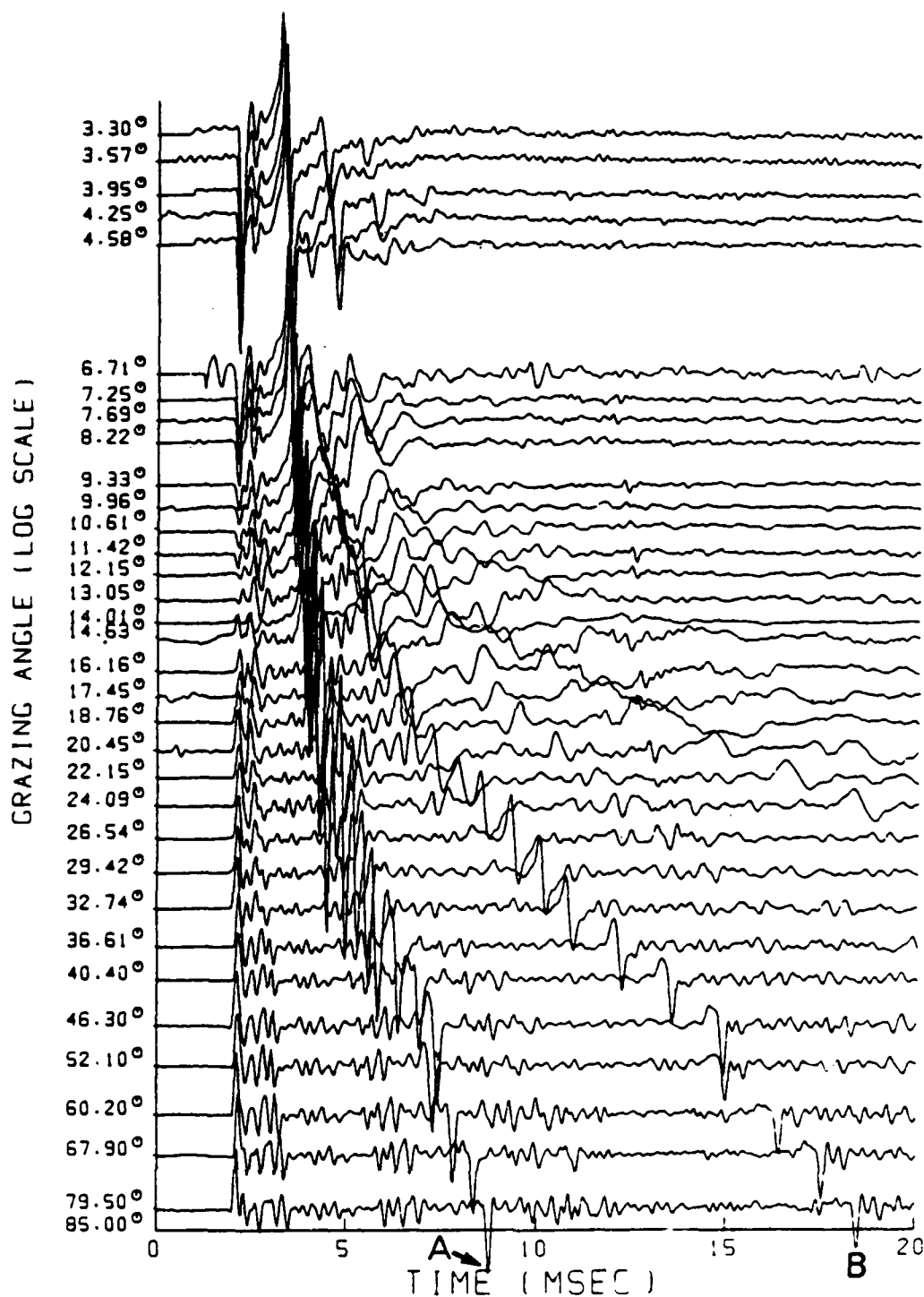
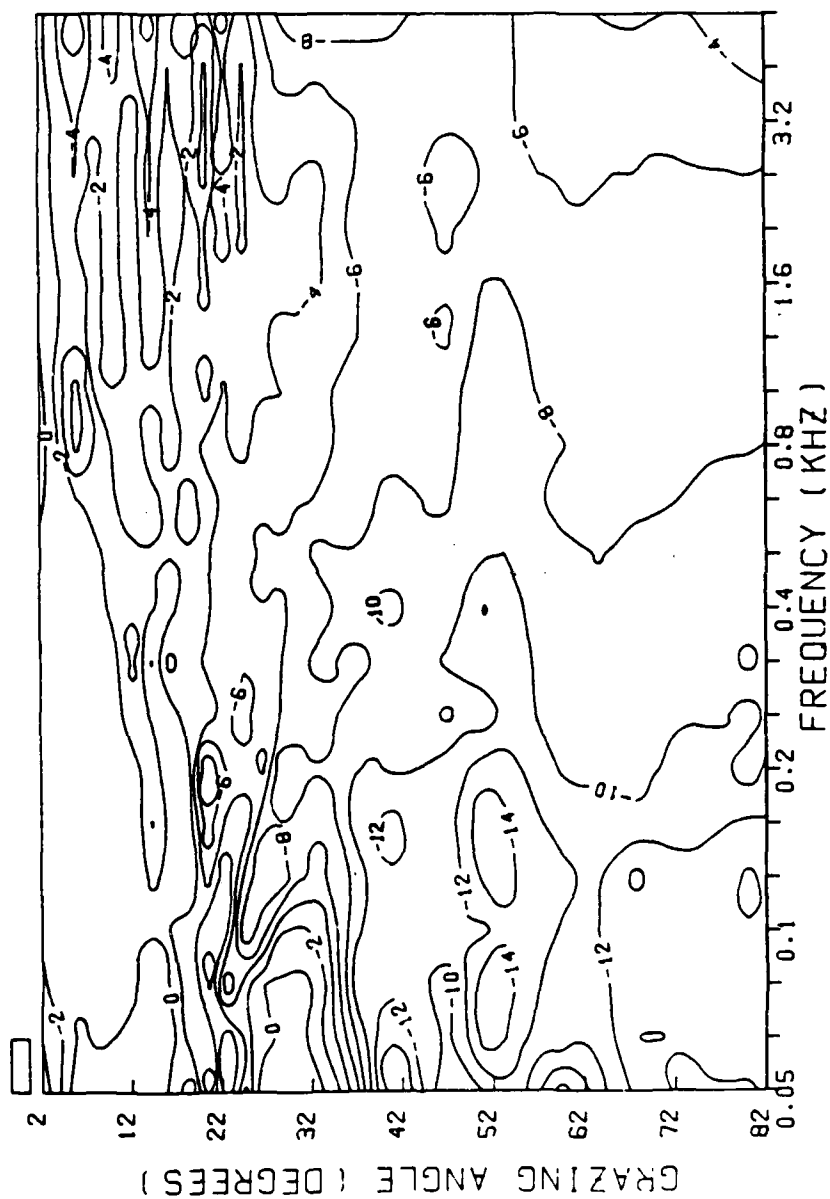Figure 14-7b. Detailed Display of the First 20 ms of Impulse Response

for Station 1

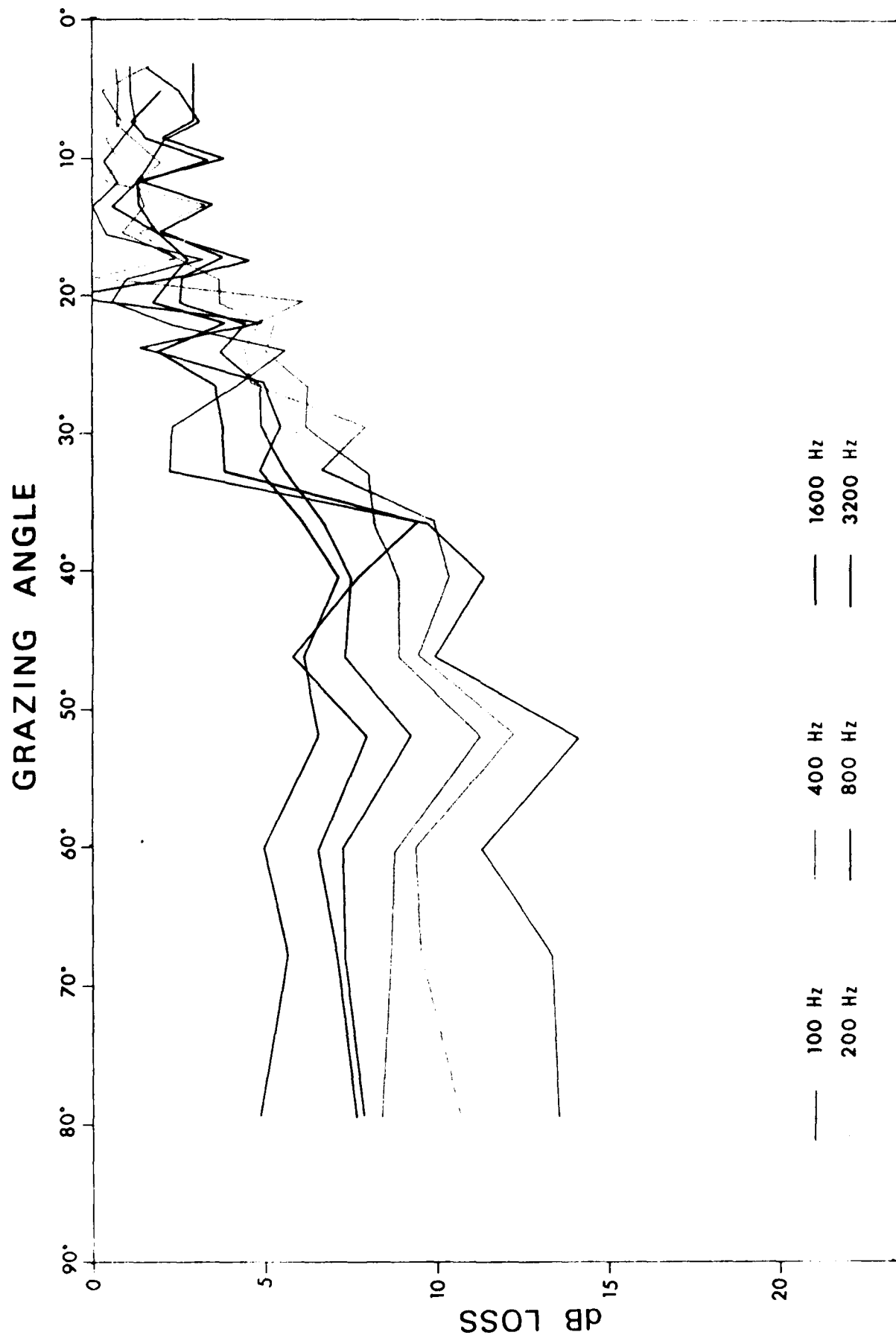Figure 14-8. Isoloss Contours (dB) versus Grazing Angle and Frequency

for Station 1

Figure 14-9. Bottom Reflection Loss Versus Grazing Angle for Station 1

The impulse response seen in figure 14-10 clearly shows that we are dealing with a bottom consisting mainly of soft, unconsolidated sediments with very few hard layers. Only the layer A, which correspond to a depth of about 30 m, is apparently hard enough to have a critical angle.

This is also seen from the loss plots on figures 14-11 and 14-12, where a critical angle of about 10° is seen for frequencies of 100 to 200 Hz and a clearly marked intromission angle occurs for the highest frequencies, with losses of up to more than 20 dB. This means that this area is not suitable for the use of hull-mounted bottom-bounce sonars.

Run 3. Mediterranean Ridge

The Mediterranean Ridge is the dominant physiographic feature of the eastern Mediterranean. It extends from the Italian continental rise between Crete and Libya to Cyprus and is bordered by deep basins to the north and south. Its length is approximately 1800 km and its width varies from 75 to 200 km. The water depth at the run is approximately 2300 m, and the topography in general is very rough with many hills and depressions reaching about 10 to 50 m in height and 1 km or more in wavelength.

This type of structure gives overlapping, hyperbola-type bottom profiles of the sea floor on the normal echo-sounding recordings. These are also clearly observable from the impulse response, shown in figure 14-13. The pulses obtained were of the chaotic type because the Fresnel (reflecting) zone moves along the bottom showing marked focusing and defocusing effects for all frequencies. This is also noticeable from the loss contours, shown in figure 14-14, where a strong focusing is observed for grazing angles around 25°.

Figure 14-10a. Impulse Response for Station 2

Figure 14-10b. Detailed Display of the First 20 ms of Impulse Response

for Station 2

Figure 14-11. Isoloss Contours (dB) versus Grazing Angle and Frequency

for Station 2

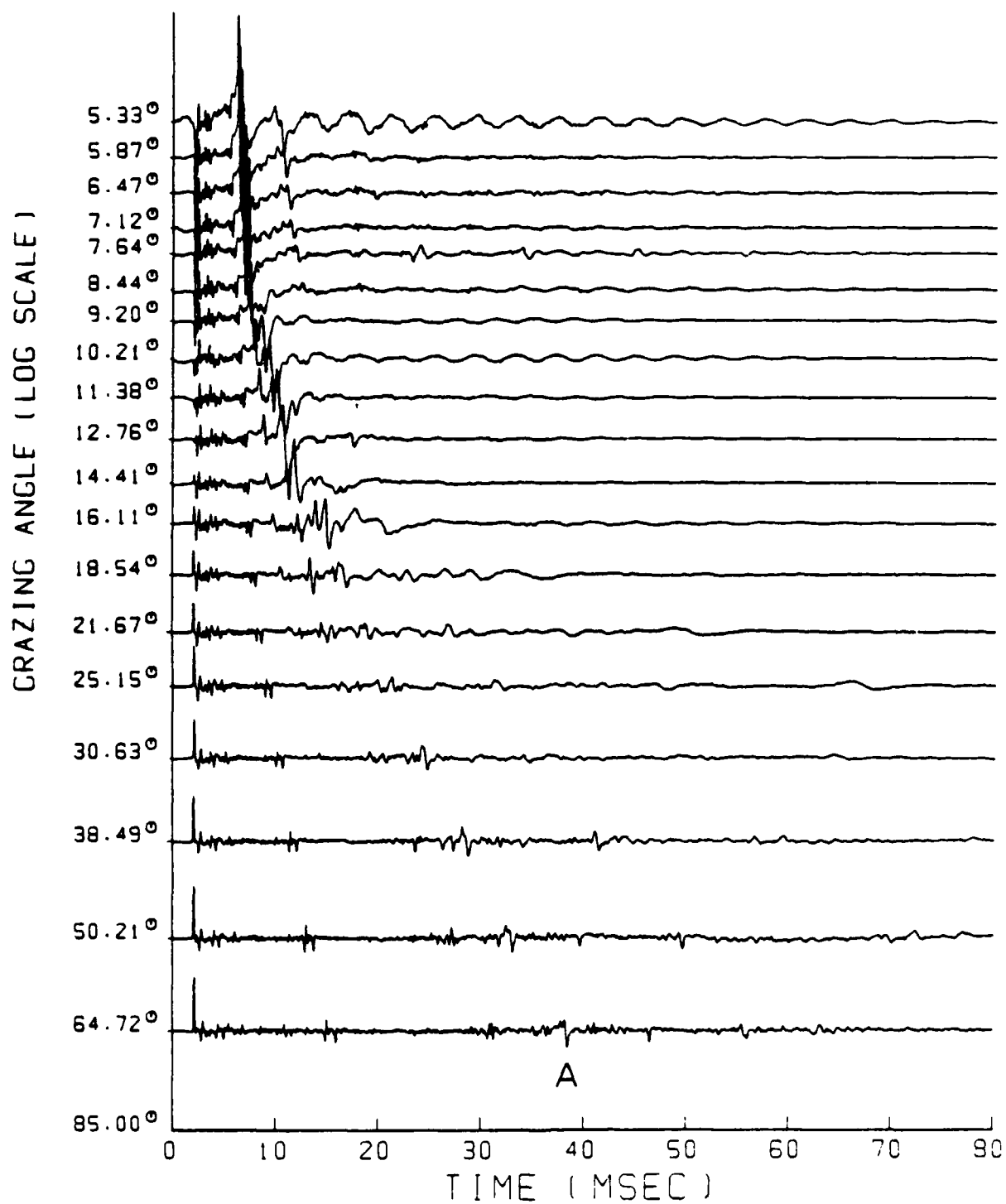Figure 14-12. Bottom Reflection Loss Versus Grazing Angle for Station 2
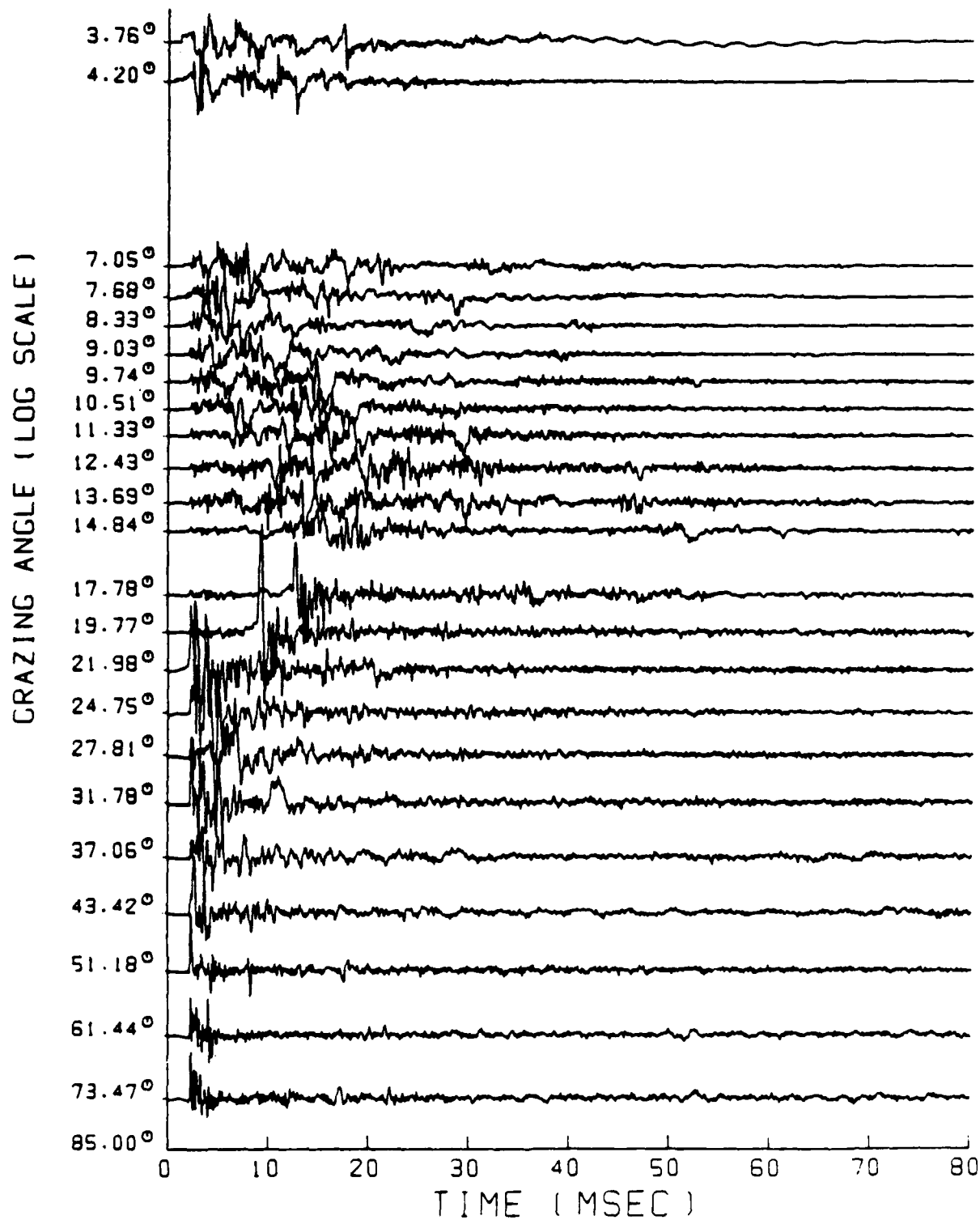
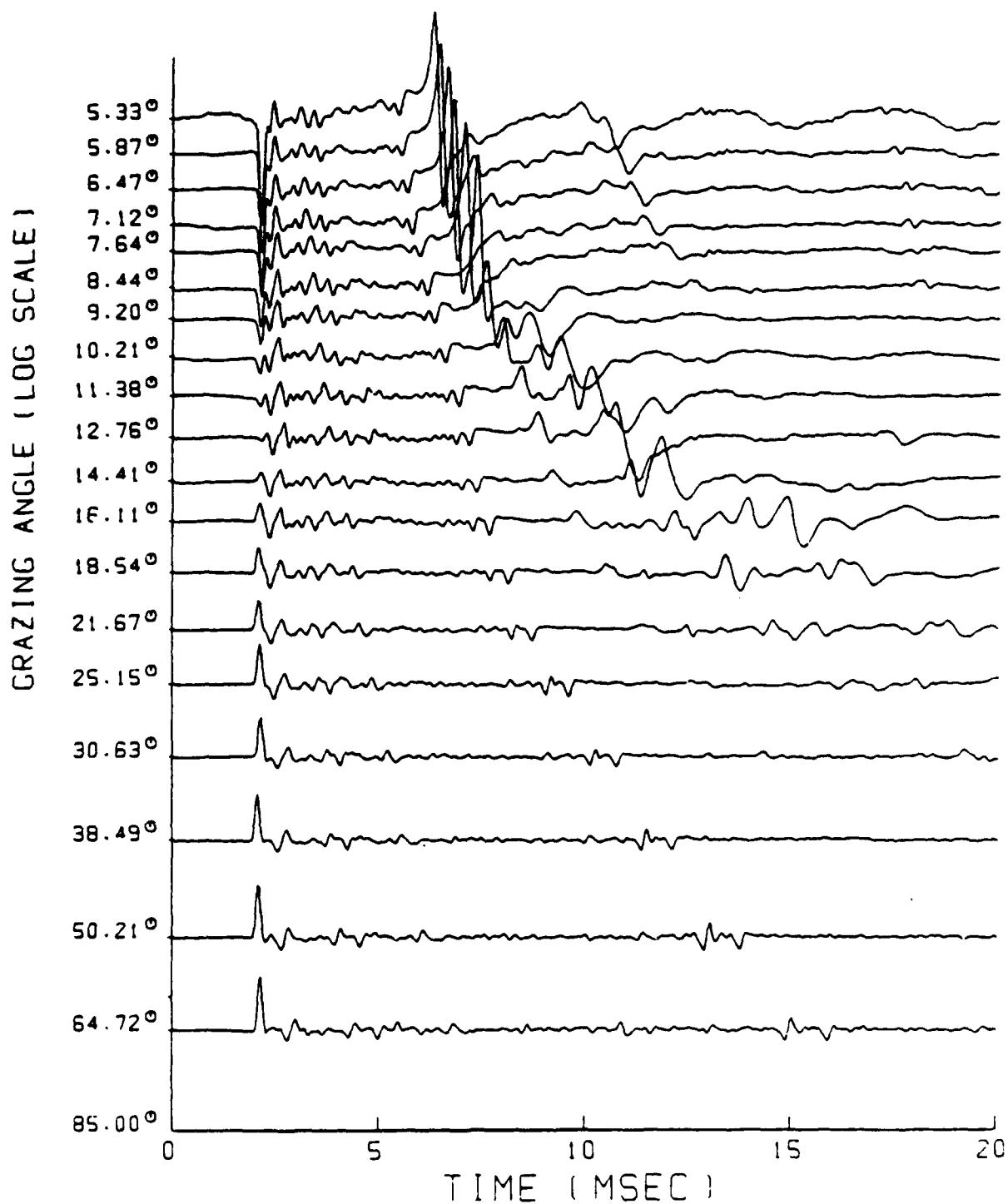Figure 14-13a.   Impulse Response for Station 3
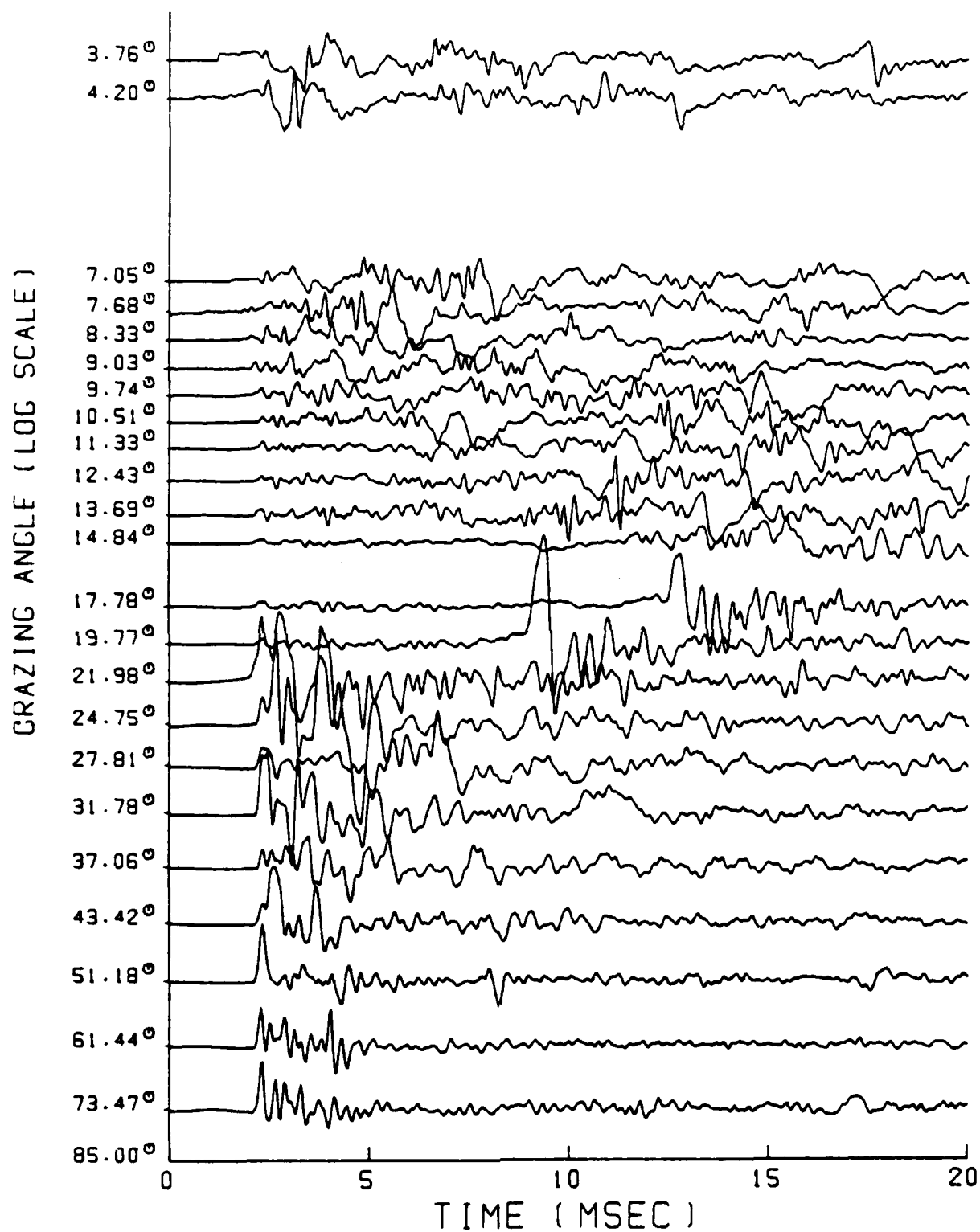
Figure 14-13b. Detailed Display of the First 20 ms of Impulse Response
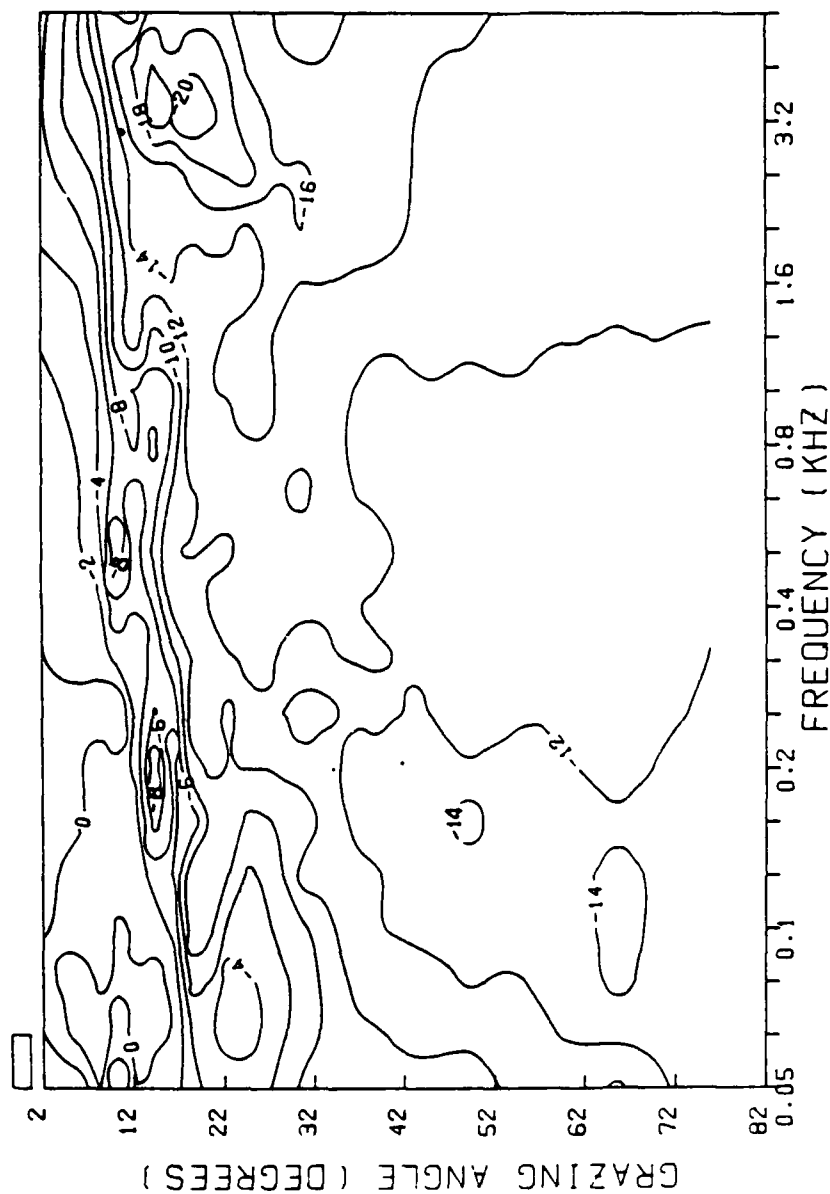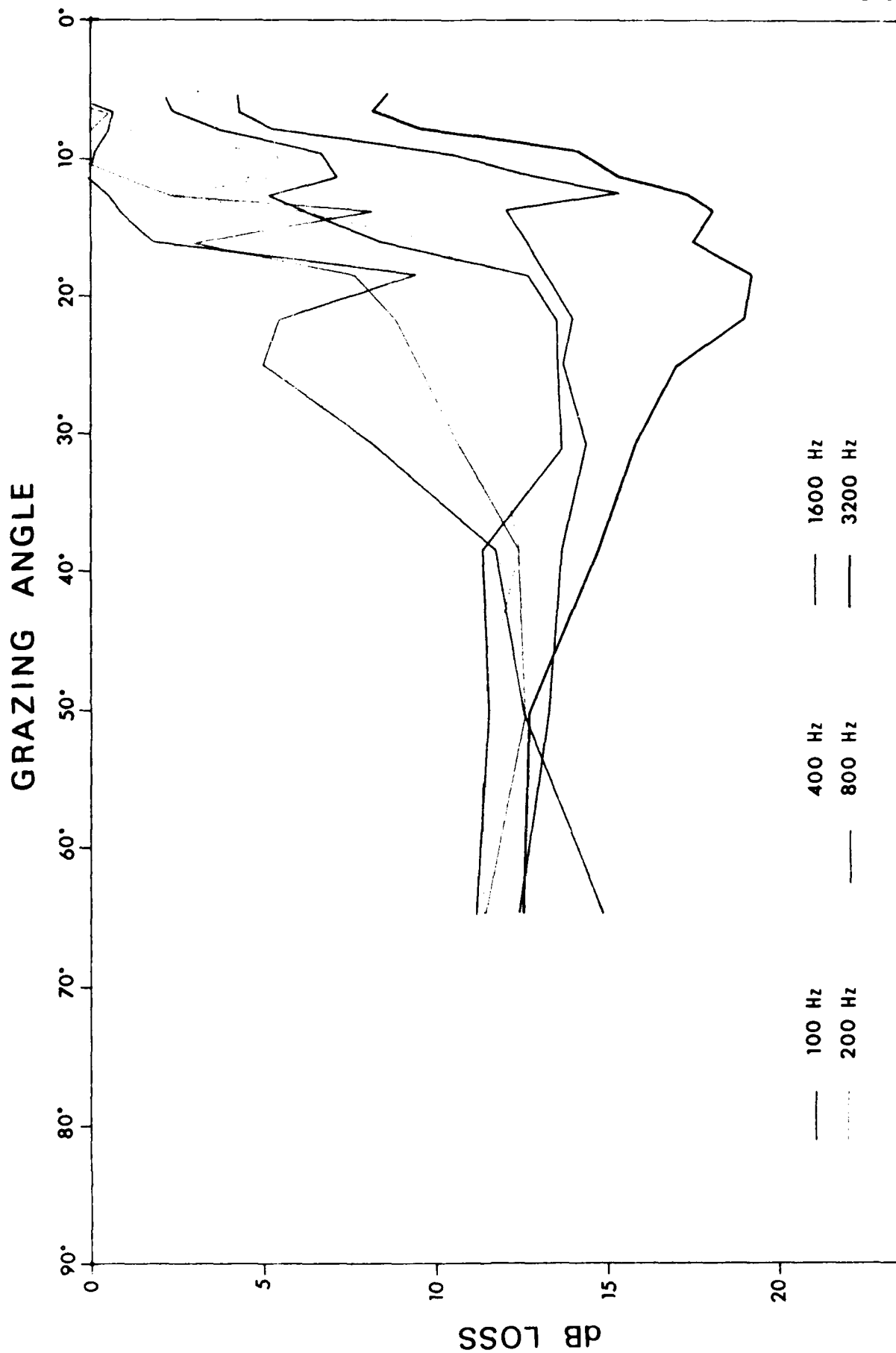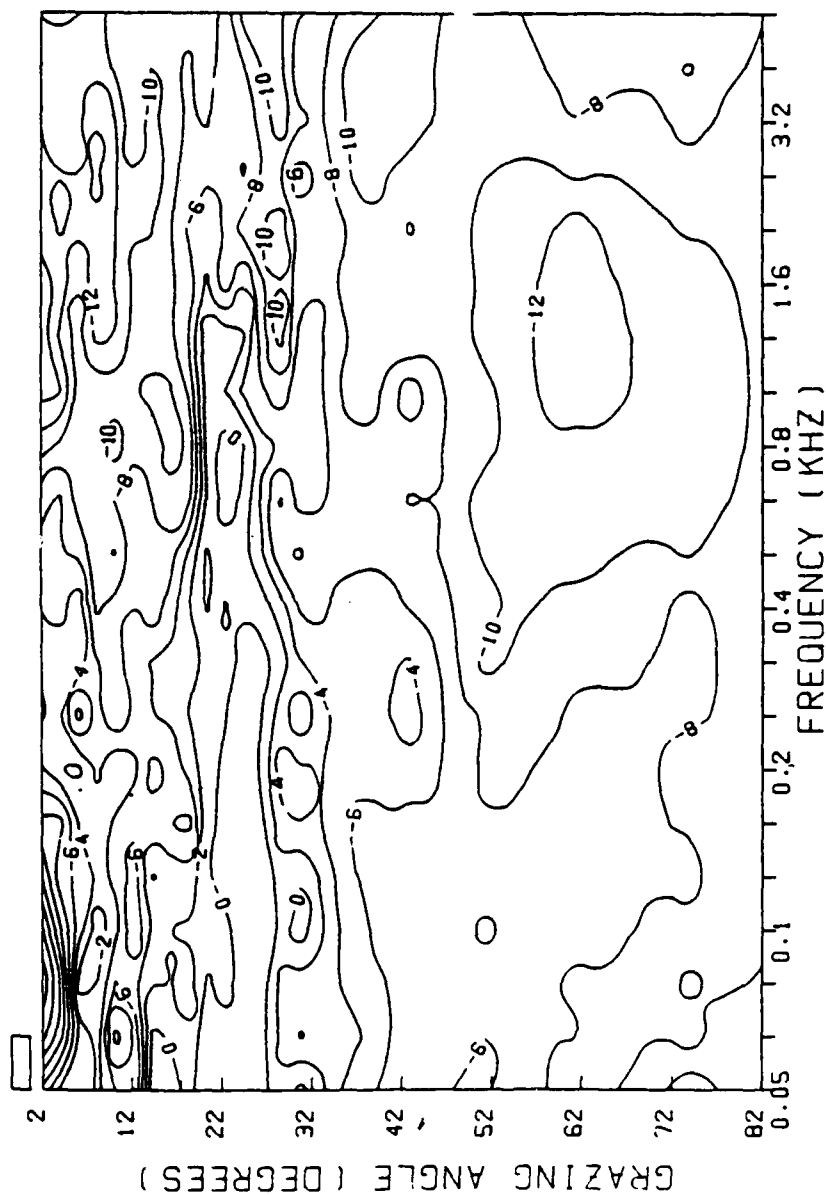
for Station 3

Figure 14-14. Isoloss Contours (dB) versus Grazing Angle and Frequency

for Station 3
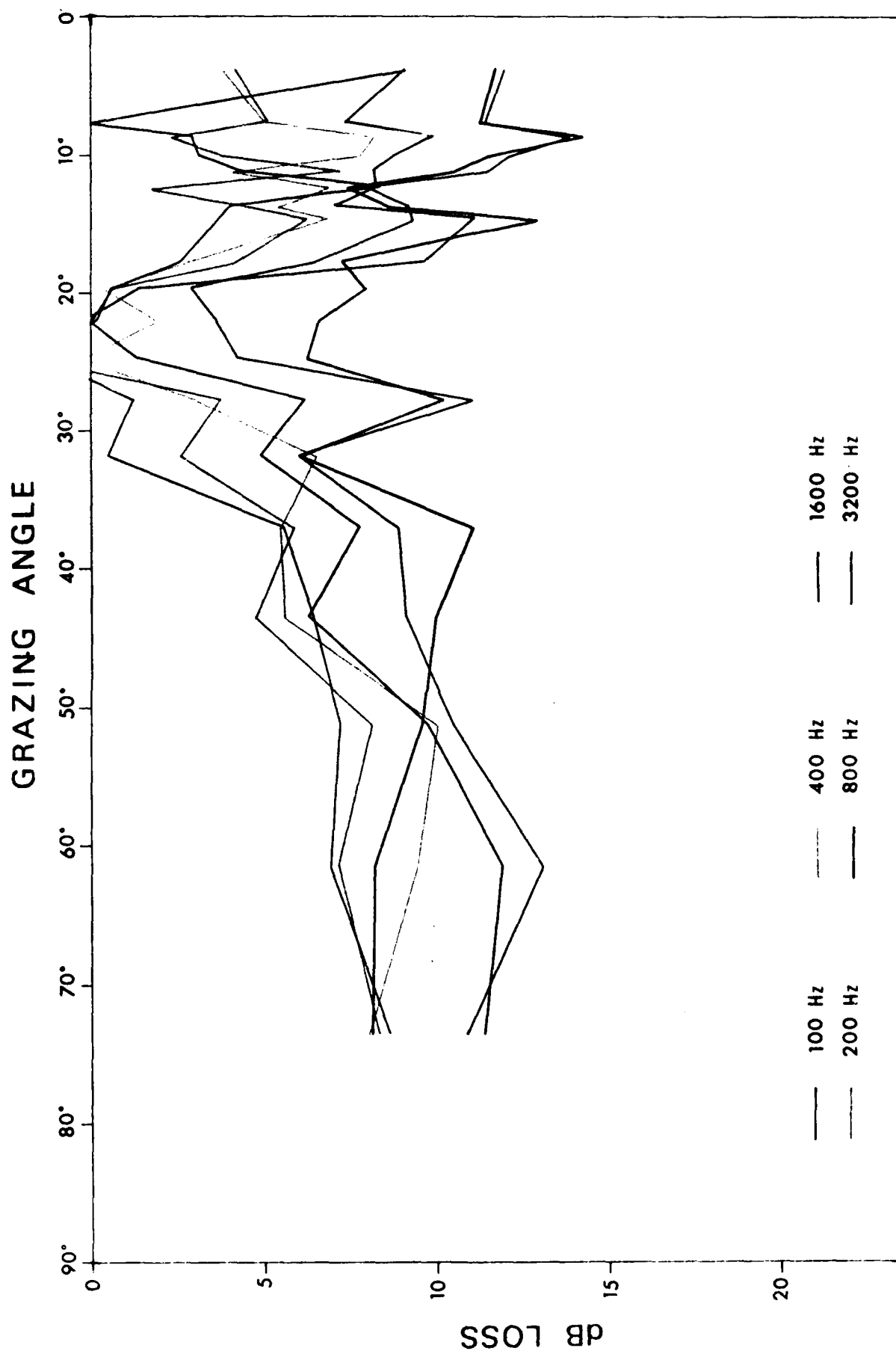
Figure 14-15. Bottom Reflection Loss Versus Grazing Angle for Station: 3

SUMMARY

Summarizing from the above and other measurements, we can conclude that areas with high-porosity, unconsolidated sediments (run 2) in general have an intromission angle at high frequencies and a critical angle at low frequencies, whereas areas with turbidity sediments (run 1) show a critical angle situation for all used frequencies. Even though the bottom material for run 3 creates a critical angle situation, the roughness of the bottom plays the major role in the reflectivity characteristics, showing marked focusing and defocusing effects for all frequencies.

To give an idea of how the reflection losses vary over an area such as the Mediterranean Sea, the results from 30 acoustic runs are shown in figure 14-16 and 14-17, again clearly showing a marked critical angle around a 20° grazing angle. For the higher frequencies, the situation is more mixed with some of the areas showing an intromission angle case and others--even for these frequencies-- showing a critical angle.

The losses for all runs are seen on figure 14-18 which represents some 6000 data points. From this, one will notice that the bottom in the Mediterranean basins is a rather good reflector with losses generally less than 10 dB, even for vertical incidence.
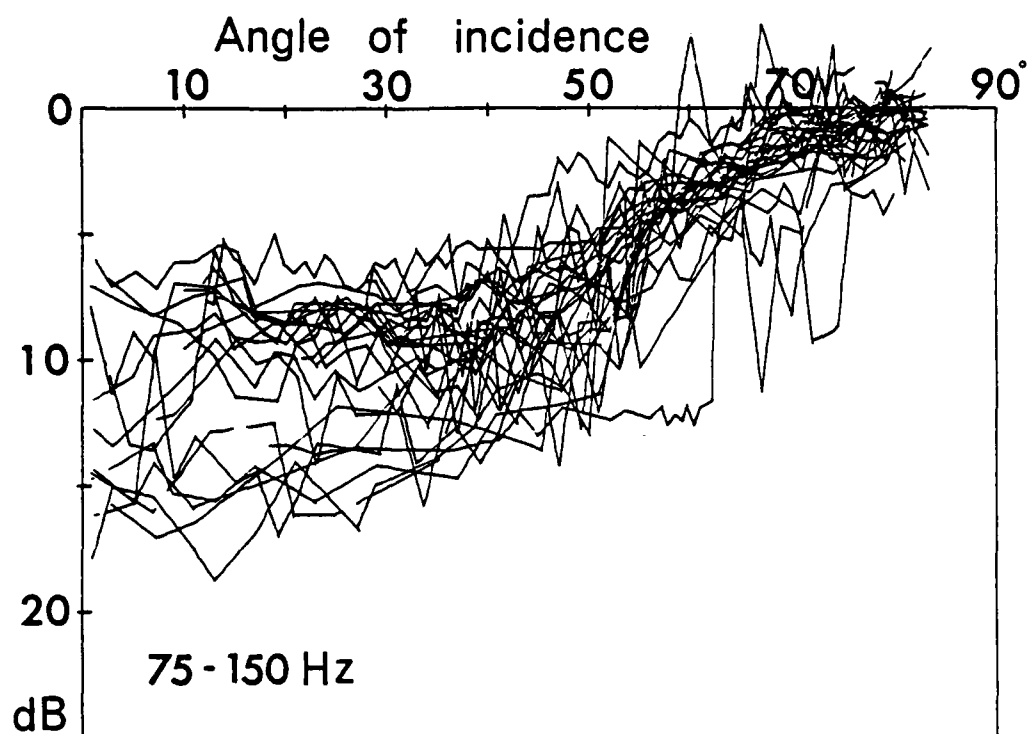
Figure 14-16.   Reflection Loss for all Runs
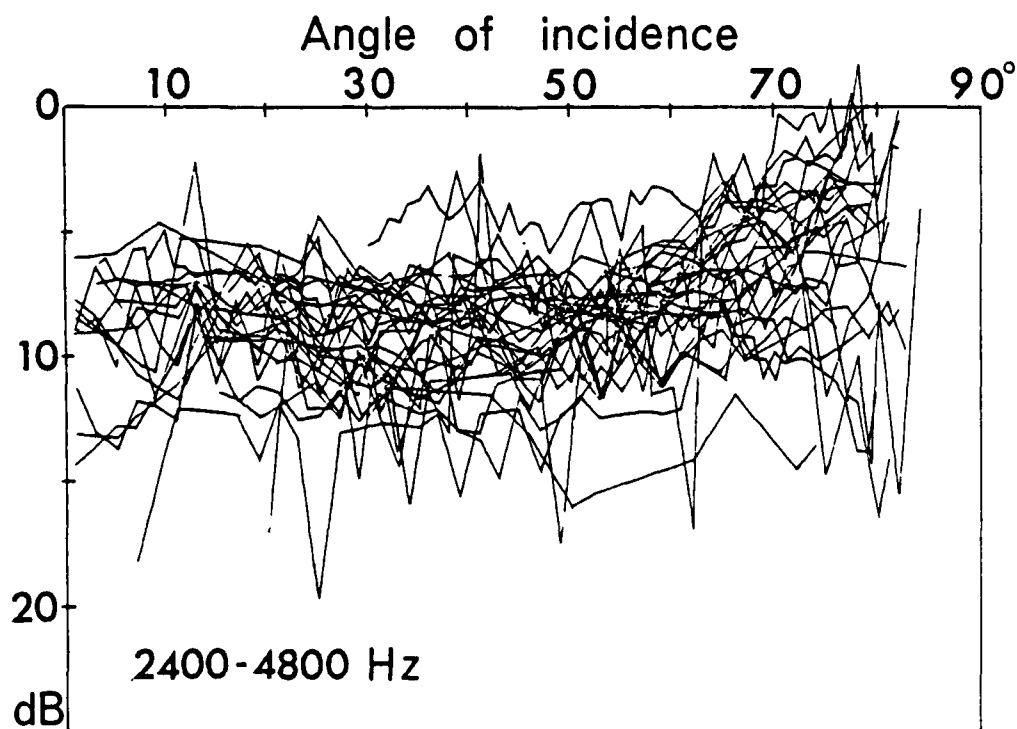
Figure 14-17.   Reflection Loss for all Runs
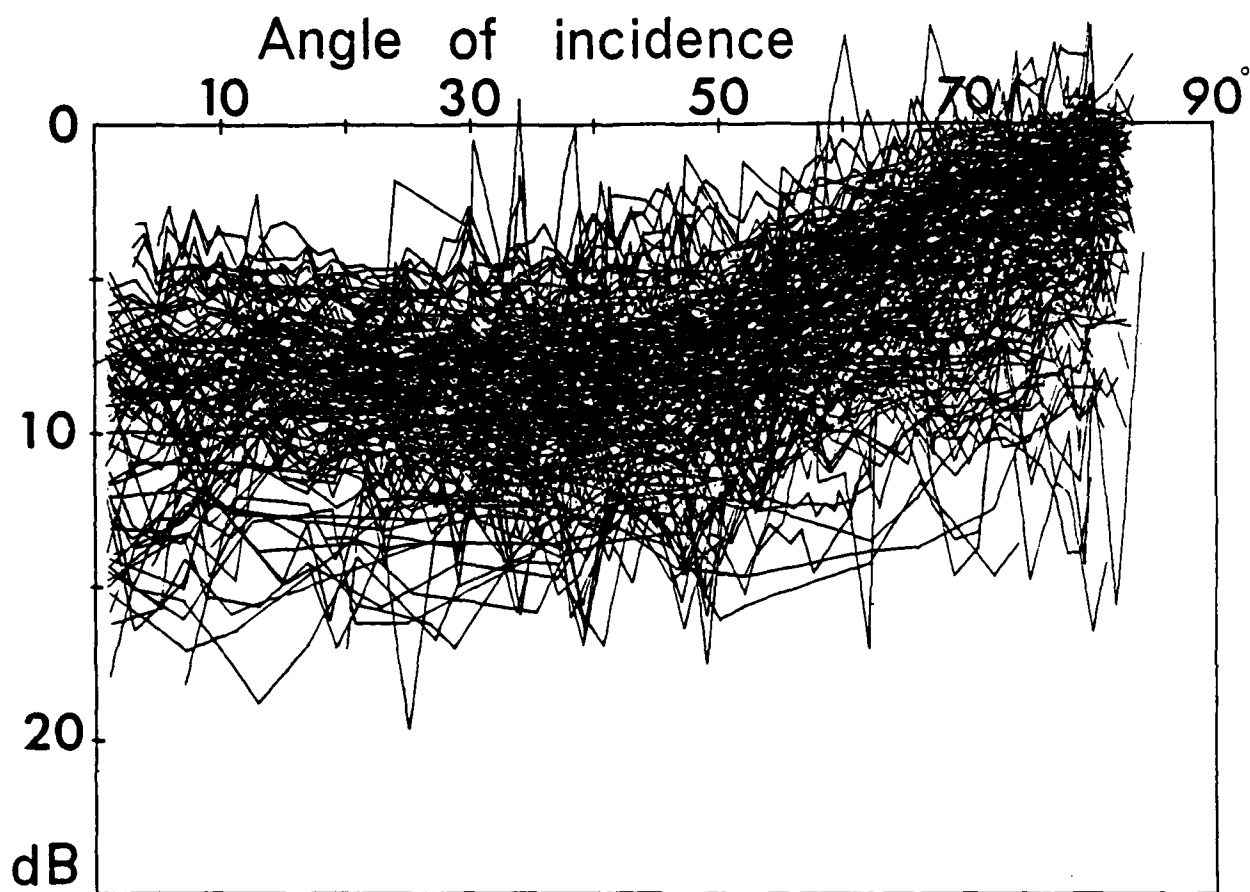
Figure 14-18. Reflection Loss for all Frequencies and Runs

CHAPTER 15

DATA ANALYSIS METHODS

In the previous chapter, we studied techniques to measure the reflection coefficient as a function of frequency for selected angles of incidence in a general way. Unfortunately, this type of representation is often too bulky for certain purposes and one searches for something as an answer to the question: What is the reflection coefficient for this bottom within something like 20° from grazing?

Several analysis and reporting techniques exist. We will look more in detail for a comparison between the following categories, which have been listed in a rather arbitrary manner:

a) Complete transfer function

b) Narrowband losses, long CW pulses

c) Total energy, bandpass filtered

d) Peak amplitude, broadband

e) Peak amplitude, bandpass filtered

f) Peak amplitude, bandpass filtered and time averaged ("sonar simulator").

To choose an exact and unbiased example by which to compare the results of using the different methods of analysis, a large number of deep sea cores taken in the North Atlantic were inspected in order to choose one whose structure seemed to be characteristic in layering, sound velocity and density. To compute the reflection coefficient, the relative sound velocity and density curves were approximated by step functions that converted the bottom into a 19-layer model. The results are shown in figure 15-1, which also shows the original measurement of sound velocity in the sediment.
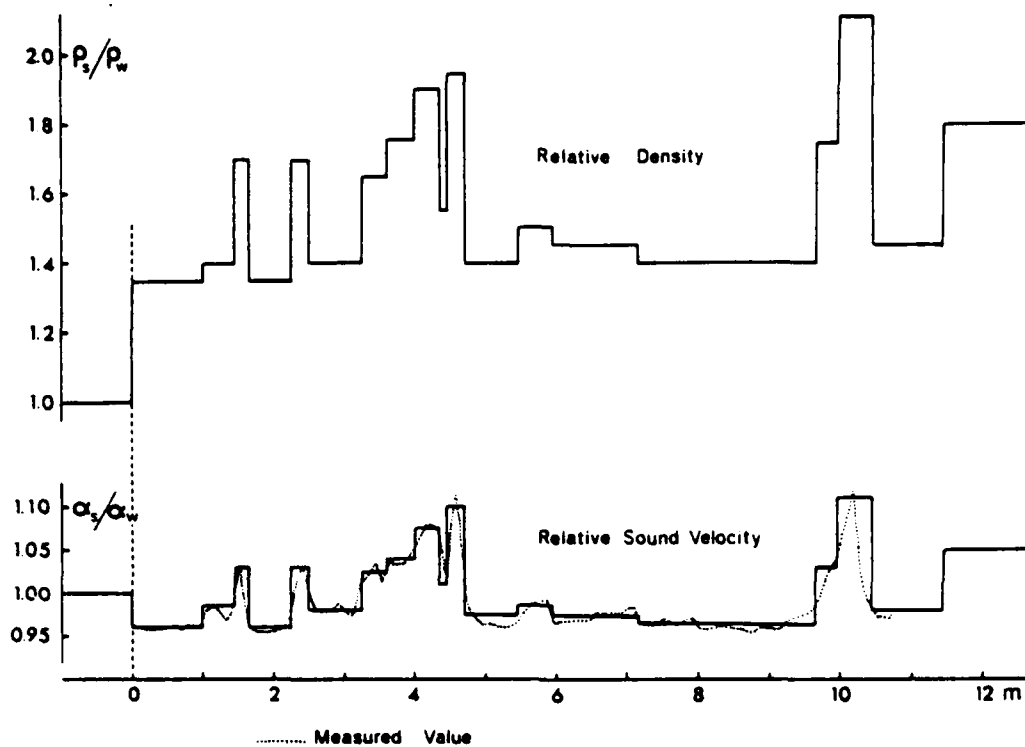
Figure 15-1. Relative Sound Velocity and Relative Density Profiles

(Indices s and w refer to Sediment and Water)

COMPLETE TRANSFER FUNCTION

The calculations for the model are done using the previously described transfer matrix technique. An example of how the reflection loss and the phase shift appear for a 30° grazing angle is given in figure 15-2. As expected and observed from experimental data, the reflection coefficient is a strongly oscillating function with up to about 30 dB between maximum and minimum, whereas the phase shift behaves in a less complicated way.

To represent the reflection loss as a function of both frequency and angle, the contours for equal loss have been plotted in figure 15-3. This type of
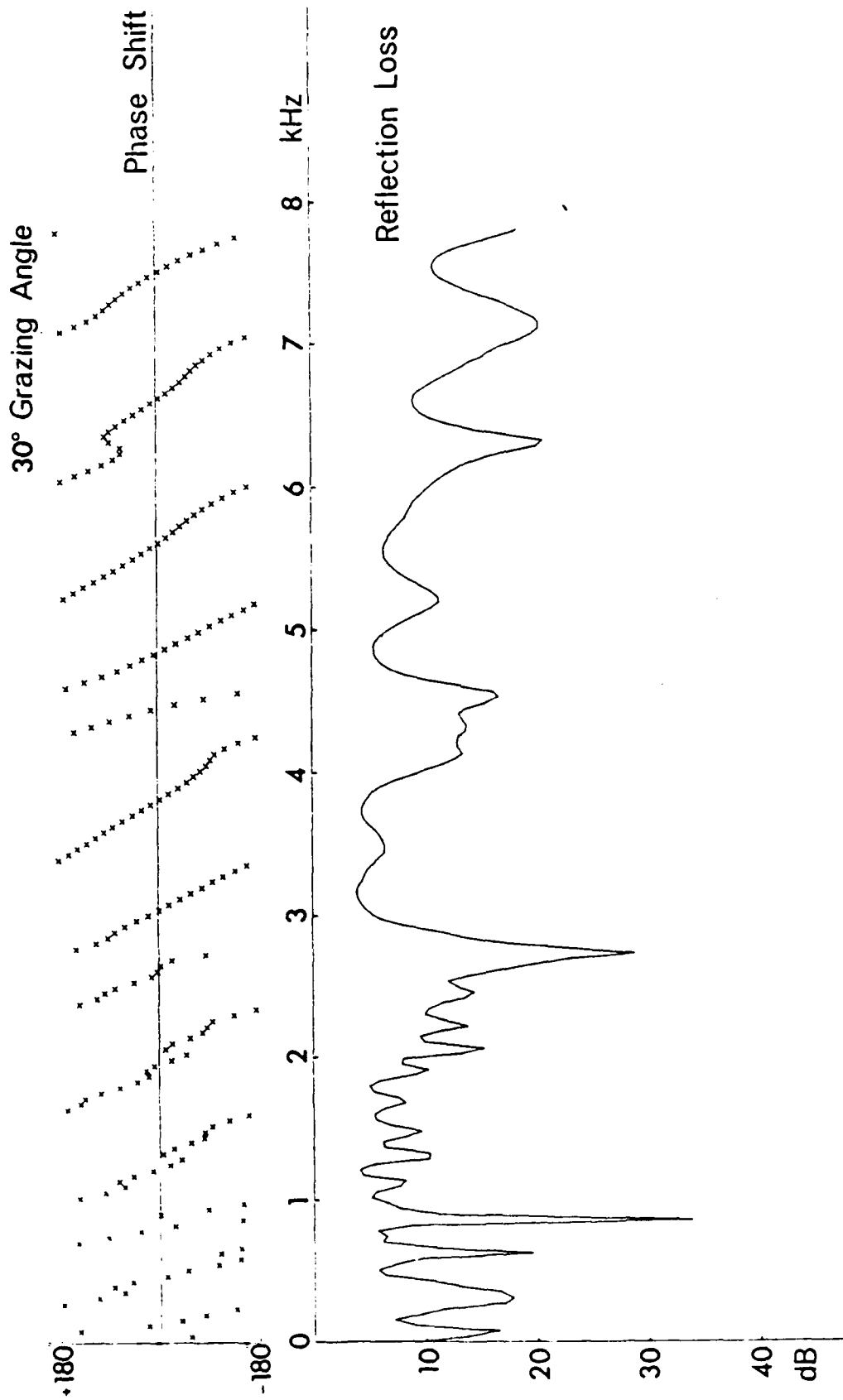
Figure 15-2. Reflection Loss and Phase Shift for 30° Grazing

display represents the full information on reflection losses, corresponding to specular reflections and pure frequencies.

From figure 15-3, it is very clear that it is meaningless to characterize the reflection coefficient by a single number without at least specifying frequency and angle interval.
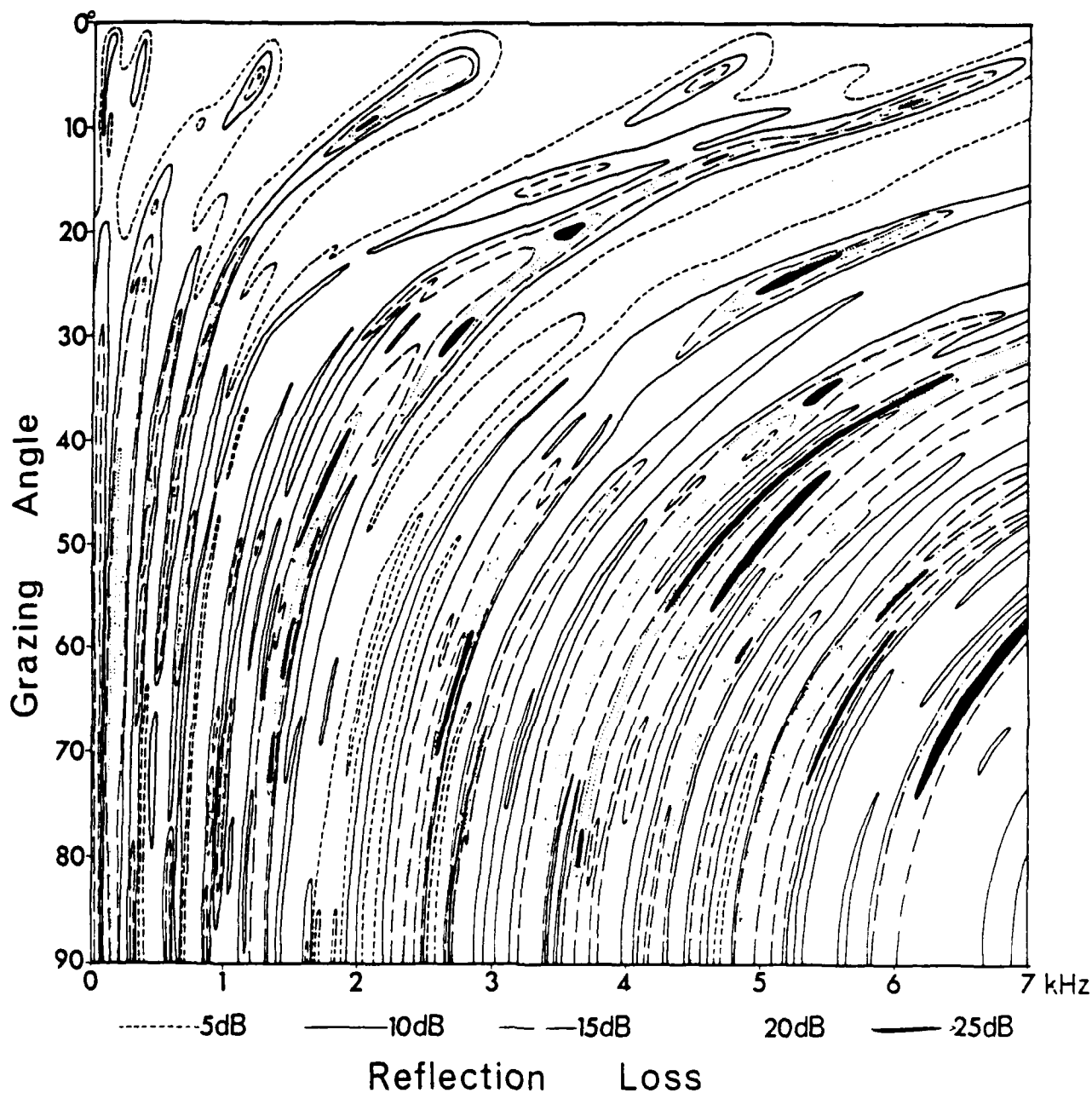
Figure 15-3. Reflection Loss Contours

NARROWBAND METHOD

Bottom-bounce sonars often use long CW pulses, corresponding to a very narrow frequency band. The bottom losses are easily obtained from figure 15-3 by cuts in the surface for constant frequency. Figure 15-4 shows the losses for a 3.5 kHz, 500 ms long, CW pulse.
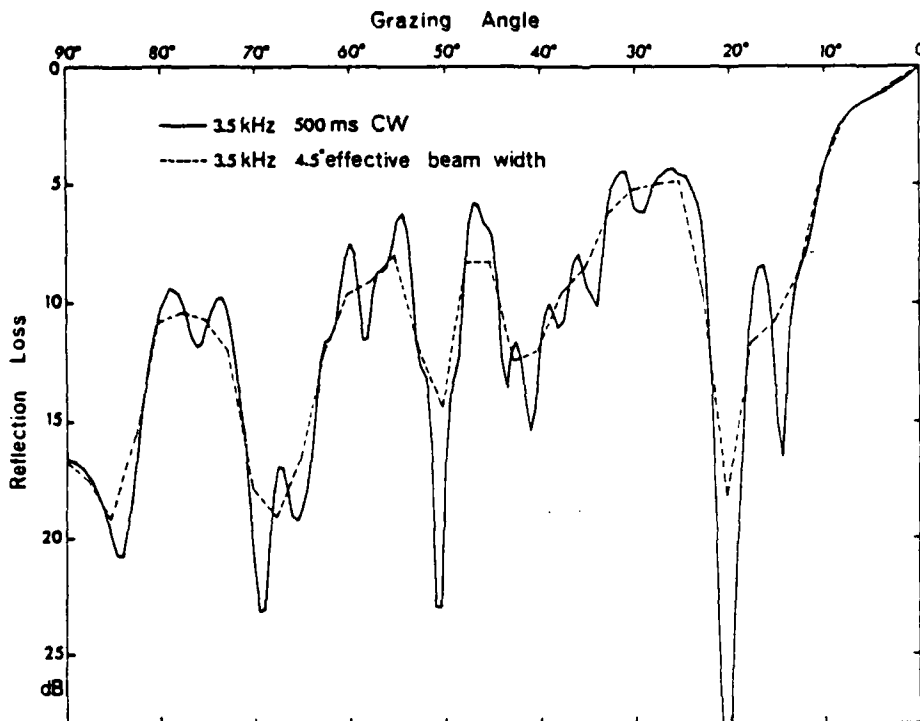
Figure 15-4. 3.5 kHz Narrowband Reflection Losses

Large fluctuations can be noticed, especially near the marked intromission angle caused by the presence of several low velocity sediment layers.

An actual sonar insonifies a finite area on the bottom, but for a flat, smooth bottom the active reflecting area is determined approximately by the size of the first Fresnel zone. This and the movement of the transducer means we have to average the losses over a finite angle interval. In figure 15-4, the reflection losses for a 4.5° effective beamwidth are also drawn. Note that, even after smoothing, large variations in the losses can be observed.

TOTAL ENERGY METHOD

One of the most frequently used analysis methods is to measure reflected energy in different band pass filters--normally octave or 1/3-octave filters. The computation for the losses to be found by this method is rather simple since we only have to integrate the transfer function in the frequency domain using the appropriate filter window.

Figure 15-5 shows the results when using a 3.5 kHz center frequency for computing the losses for octave and 1/3-octave filters. Note how the octave filtering now almost masks the intromission angle, whereas this feature is clearly recognizable for the 1/3-octave filter. As a reference, the pure 3.5 kHz losses are also shown by a dotted line.
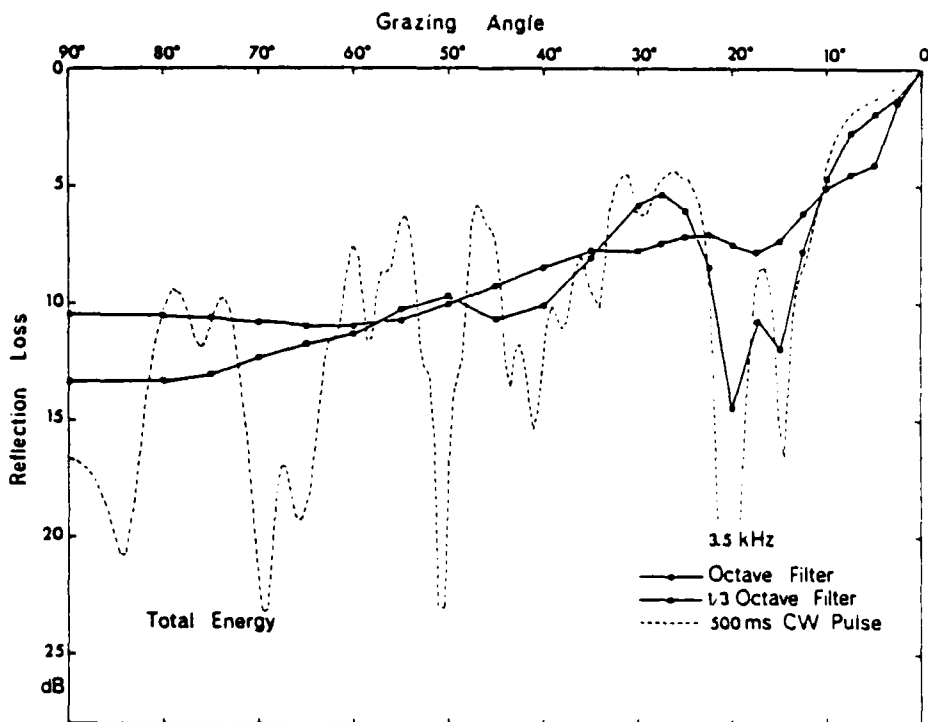
Figure 15-5. Octave and 1/3-Octave Reflection Losses

(3.5 kHz Center Frequency)
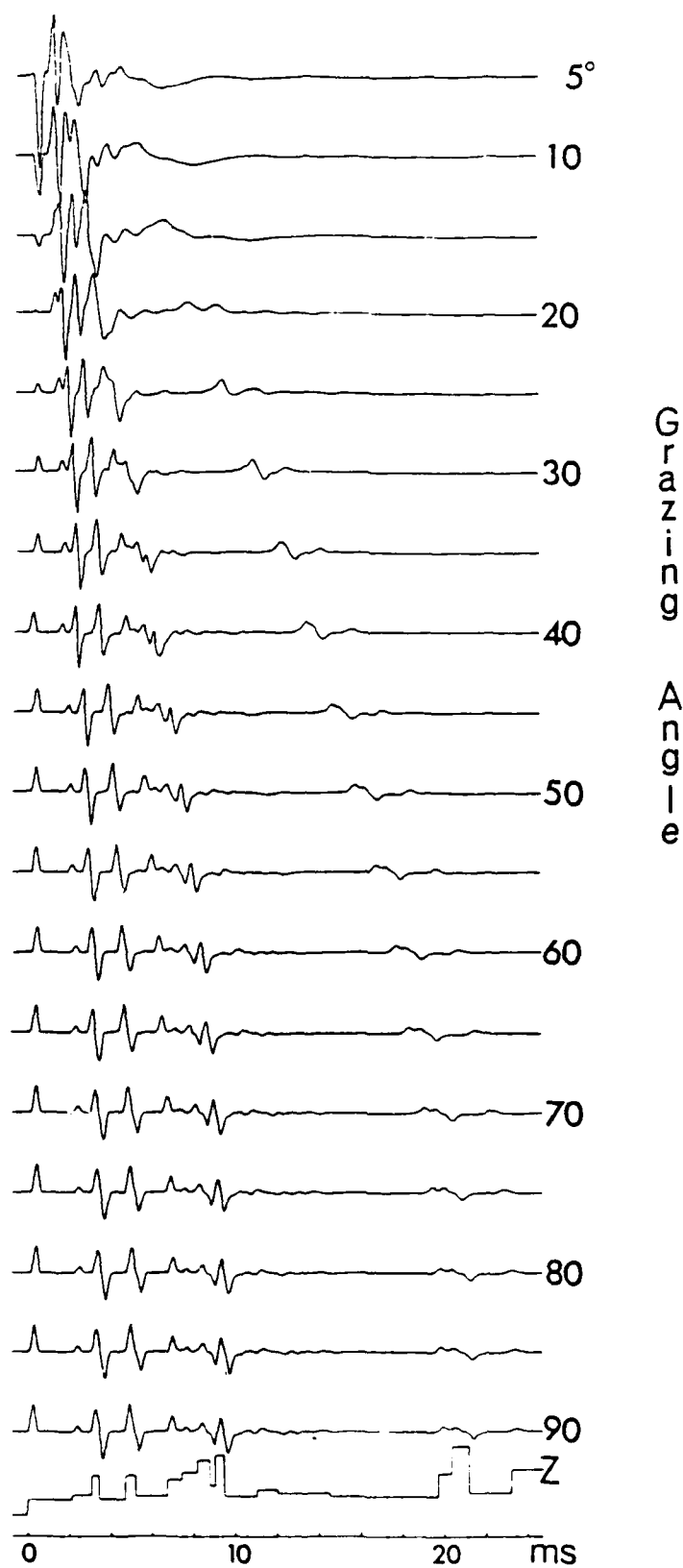
Figure 15-6. Bottom Impulse Response and Layer Impedance

PEAK AMPLITUDE METHODS

One popular method to calculate the reflection coefficient has been to use the ratio between the peak amplitude of the reflected and incident pulses. To investigate the effect of this procedure, we will use the impulse response obtained from the layering in figure 15-1. Figure 15-6 shows the responses calculated for a sequence of angles. Also shown is the vertical layer impedance scaled to travel time. Note the 180° phase shift for the first reflection at an angle near 19° due to the intromission angle for the upper layer. The compression in time with decreasing grazing angle due to the change in the vertical wavenumber is also clearly shown.

If we are dealing with a single reflector, it would be correct to measure the reflection coefficient from the broadband peak values due to the frequency independence. The broadband losses are seen in figure 15-7, where the largest peak has been used.
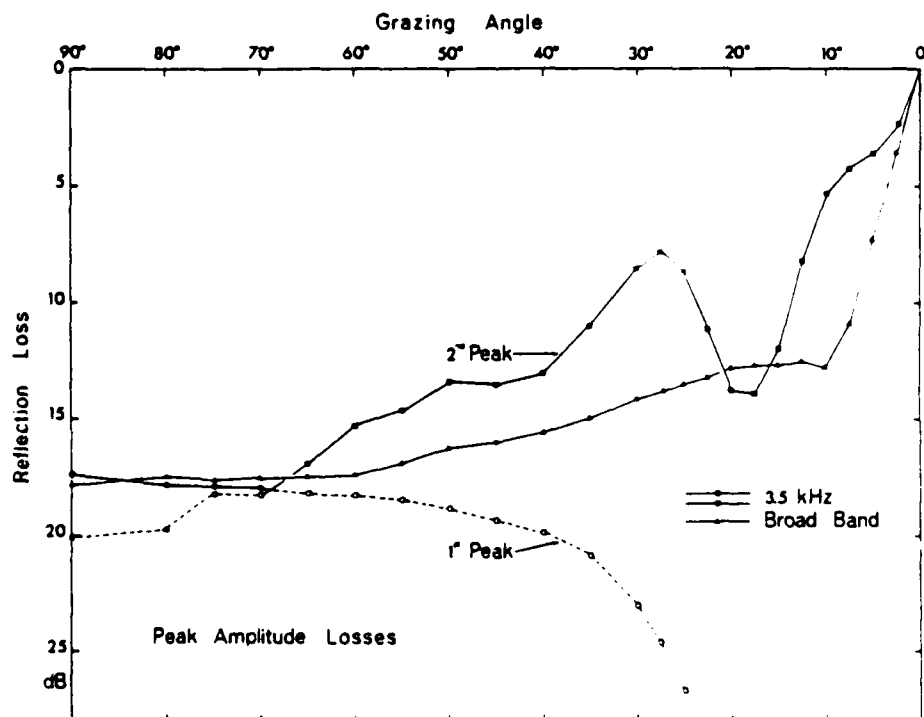
Figure 15-7. Peak Amplitude Reflection Losses

Usually, however, as in our case, the reflection coefficient is frequency-dependent and filtered peak values are used for the loss computations. Figure 15-8 displays the bandpass-filtered impulse responses using a Gaussian 1/3-octave filter centered around 3.5 kHz. The reflection loss is computed from the peak values.

The result has been added to figure 15-7. Contrary to the broadband data, the filtered data again show the intromission angle and, by a comparison between these data and the energy data from figure 15-5, we see that the peak amplitude method, as expected, usually yields much higher losses.

SONAR SIMULATOR METHOD

Some sonars process their data by using reflected energy averaged over a certain time window. For this reason, losses are determined in a similar way using a so-called sonar simulator, an analog device consisting of a bandpass filter, a half-wave rectifier and a lowpass filter. Losses thus obtained can be computed from the impulse response, but due to the nonlinear characteristics of the rectifier, the numerical computation has been done in several steps.

For the computations, Gaussian filters were used with 1/3-octave bandwidths centered around 3.5 kHz and a time constant of 7 ms to 8 ms. The result is shown in figure 15-9, which for comparison also contains the results from the other applied methods. From this figure, we can conclude that, excert for a small angle interval, the loss curves obtained in different ways show considerable divergence, in some cases more than 10 dB. In this particular example, the methods using averaged and total energy yield almost identical results at grazing angles of importance for bottom-bounce sonar applications. However, when deeper interfaces are the important reflectors, one might expect differences in results between the two methods.
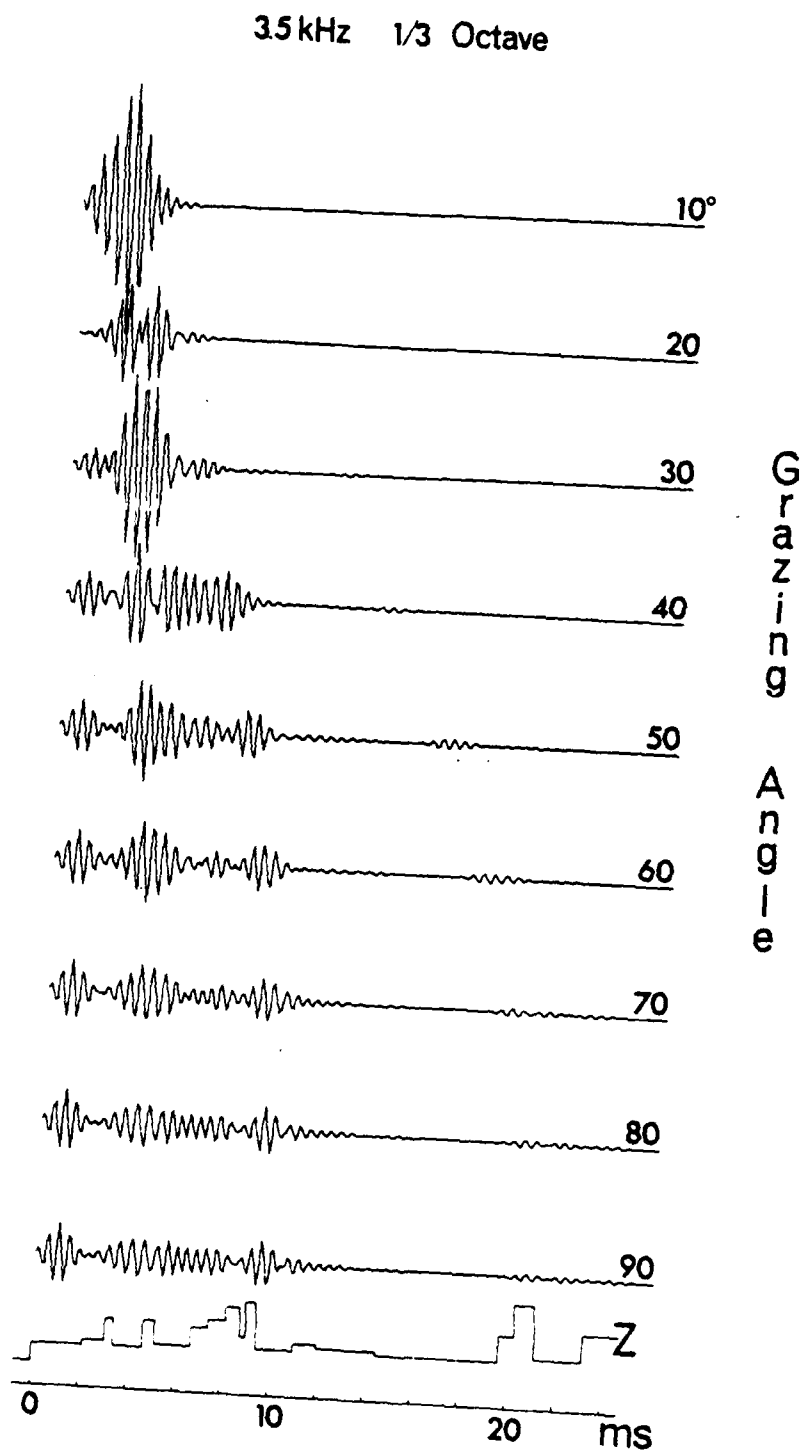
Figure 15-8. 1/3 Octave Reflection Response and Layer Impedance

Grazing Angle
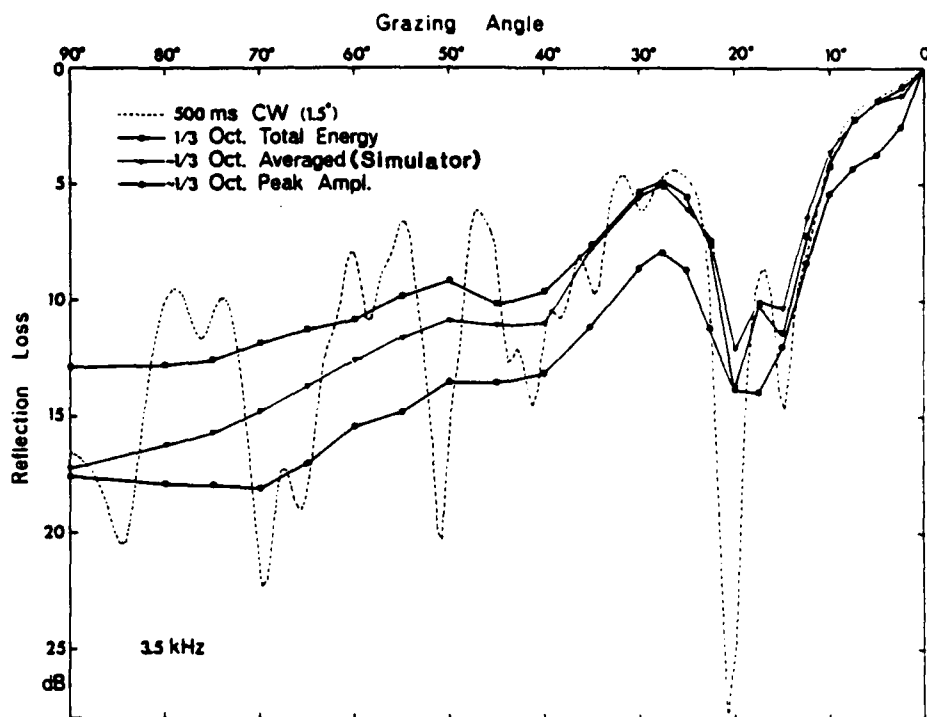
Figure 15-9. Sonar Simulator Reflection Losses

From the above, we can conclude that only the complete transfer function gives the correct solution for both short and long pulses. However, for practical purposes, the use of total energy filtered in 1/3-octave bands seems to be a good compromise between ease of computation and the reporting of a reasonable amount of resulting data.

CHAPTER 16

PREDICTION OF REFLECTIVITY

We have looked at the theory and the measurement of bottom reflectivity; however, our key objective is to establish to what extent the bottom reflectivity can be predicted from knowledge of the acoustical parameters of the bottom. For this purpose, a well controlled experiment was performed in the Naples Abyssal Plain in the Tyrrhenian Sea at the position shown in figure 16-1.
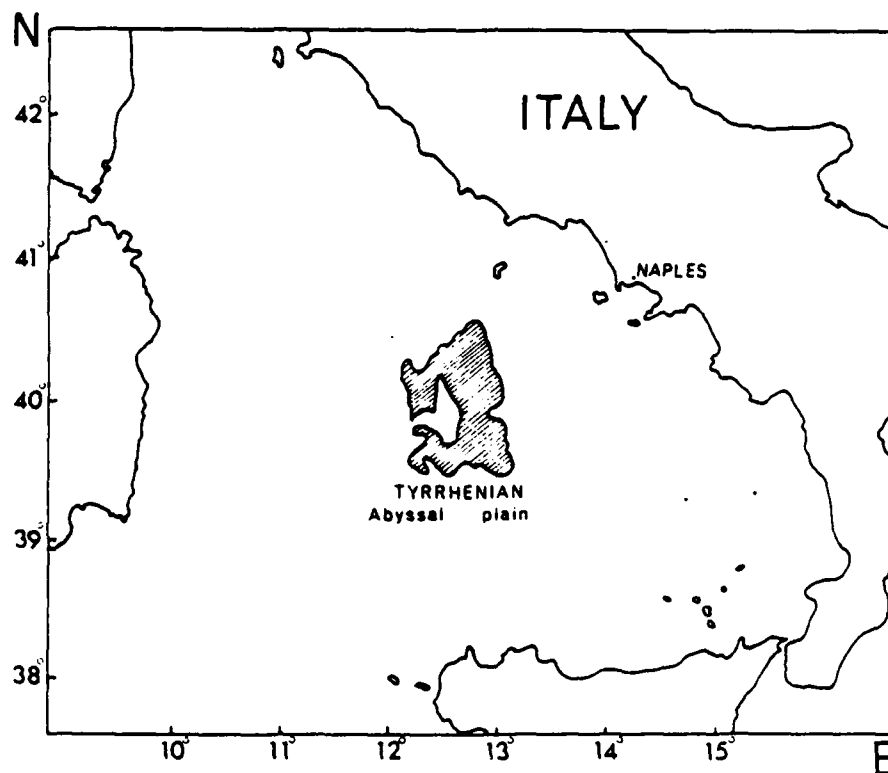
Figure 16-1. Position of Tyrrhenian Abyssal Plain

At this location, the water depth is 3600 m and the bottom consists of a large number of continuous clay and sand layers deposited by turbidity currents, thereby serving as a model for a multilayered deep sea bottom.

The measurements were made using the technique described in chapter 14 except that the receiving hydrophone was kept suspended 150 m above the bottom in order for the layering to be as constant as possible over the isonified part of the bottom. The explosive charges consisted of 500 g TNT with a depth setting of 550 m which creates a bubble pulse period of 10 ms.

Figure 16-2 gives a detailed display of the first 27 ms of both the direct and reflected pulses, showing the characteristic compression of the signals as the angle of incidence changes from vertical incidence to grazing. Note also the intromission angle at about 77° for the reflection from the water interface. This situation was dealt with in detail in chapter 4 and the reflection losses illustrated in figure 4-2.
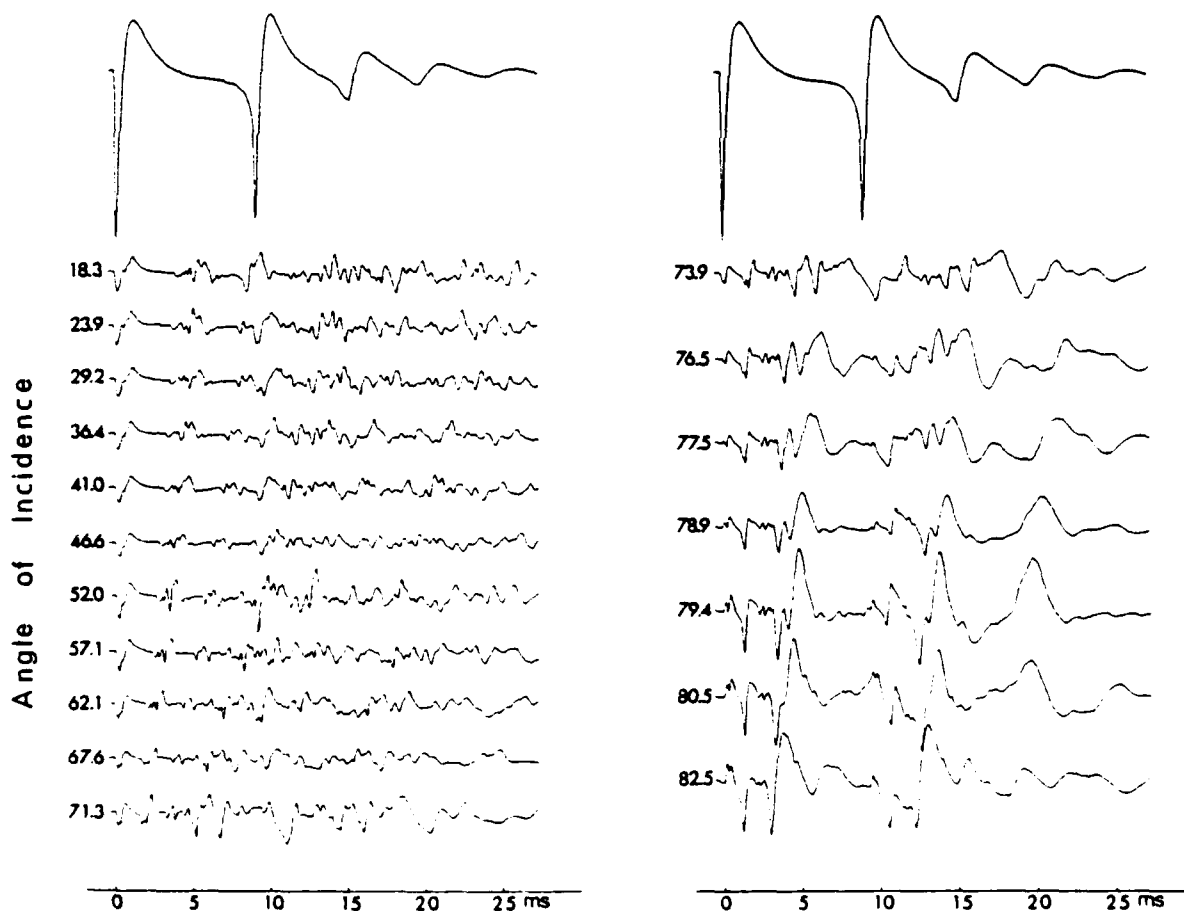
Figure 16-2. Signal Shape as a Function of Angle of Incidence

An inspection of the signals closest to vertical incidence showed that the major part of the reflection happened within the first 55 ms, and this value was therefore used for the truncation of the signals.

Figures 16-3 and 16-4 show examples of the reflection loss and phase shift for 24.4° and 73.9° angles of incidence in the frequency interval 20 Hz - 5000 Hz. As predicted from the theoretical calculations, the loss is a strongly oscillating function with up to 30 dB between the maximum and minimum loss.
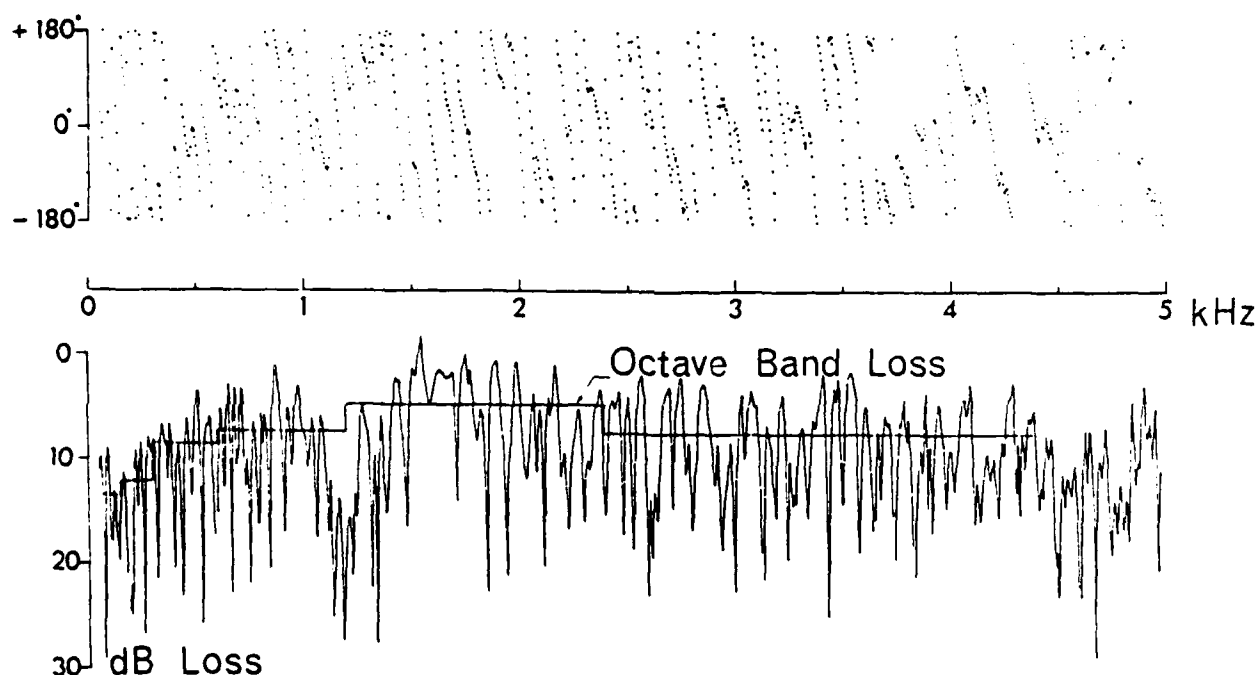
Figure 16-3. Reflection Loss and Phase Shift for 24.4°

The phase shift on the other hand, shows a rather linear frequency dependence, indicating a time delay probably due to reflections from a major reflector. At the higher angles, there is a noticeable smoothing of the loss curve due to the shallower penetration.
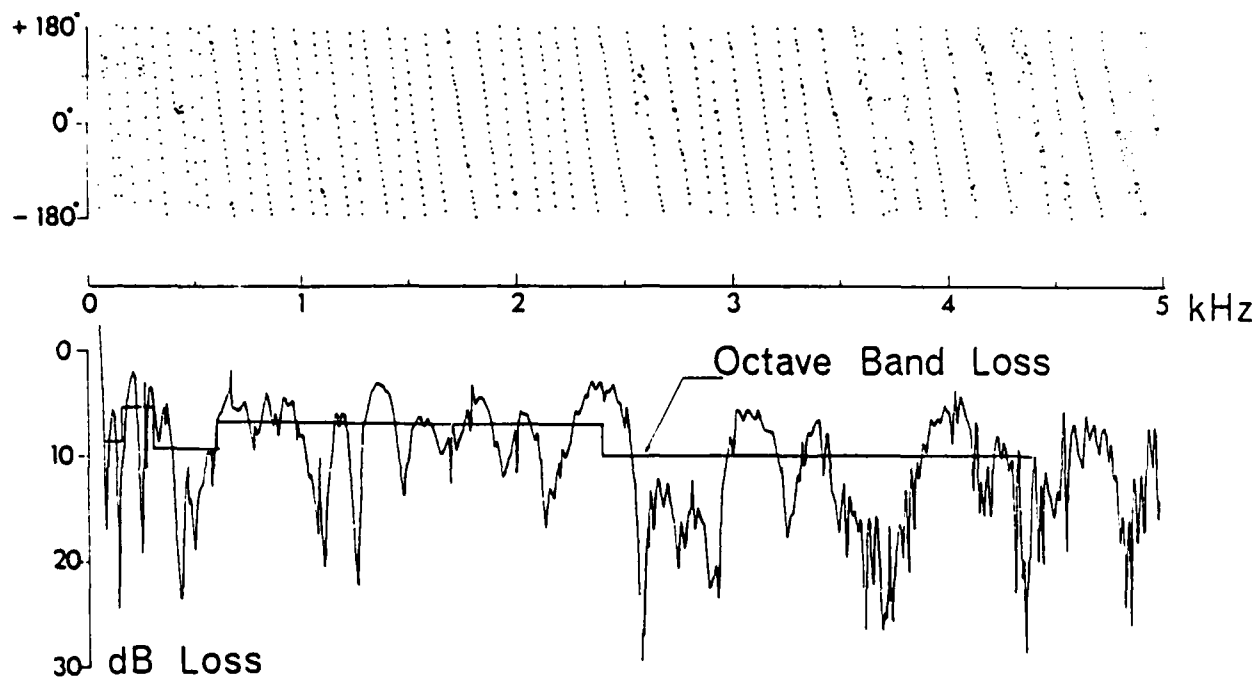
Figure 16-4. Reflection Loss and Phase Shift for 73.9°

Figure 16-5, which shows the losses for a 62° angle of incidence, with respectively 31 ms and 95 ms integration times illustrates the effect of signal length on the shape of the loss curve. As expected, the curve corresponding to 95 ms gives less loss for the lower frequencies and also shows faster oscillations due to the greater effective layer thickness.

Although the picture looks confused, the losses are found to behave in a very systematic way if the angle is taken into consideration. Figure 16-6 displays the losses at different angles of incidence as a function of frequency. We see that the maxima and minima are not randomly distributed but follow a well defined trend with the expected shift toward higher frequencies with an increasing angle of incidence.
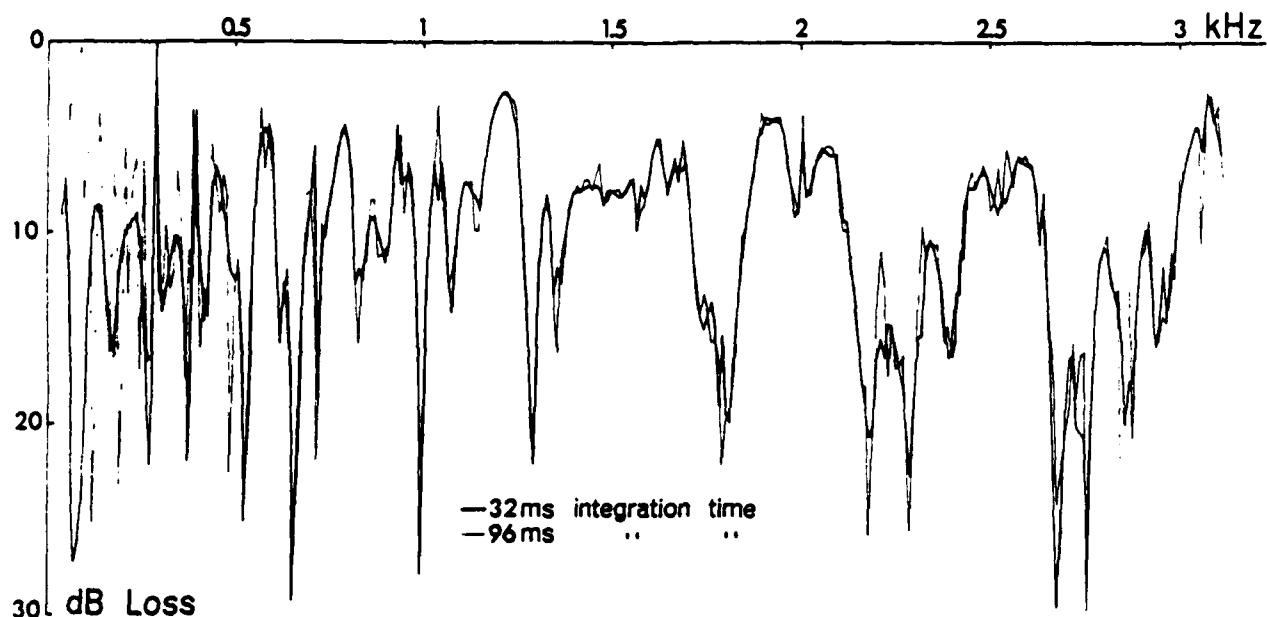
Figure 16-5. Effect of Integration Length on Shape of Loss Curves for 62°

For a better absolute determination of the losses as a function of frequency and angle, the data have been used to construct a map (shown in figure 16-7) giving the reflectivity as isoloss contours for 5 dB, 10 dB, 15 dB and 20 dB. This picture clearly shows that the reflectivity cannot be described by a single parameter without the specification of angle and frequency. A strongly reflecting region is found around 18° incidence and 1500 Hz, with minimum losses of about only 2 dB, and is caused by periodic layering, a subject studied in detail in chapter 13.

The impulse response being the inverse Fourier transform of the complex reflection coefficient has been calculated using a Gaussian filter in order to avoid artificial overshoots and the result is seen in figure 16-8. One will notice a strong reflection occurring for 18° at 14 ms which for vertical incidence is equal to a depth of approximately 10 m, in fact at the depth where most of the bottom cores taken stopped confirming the presence of a hard layer.
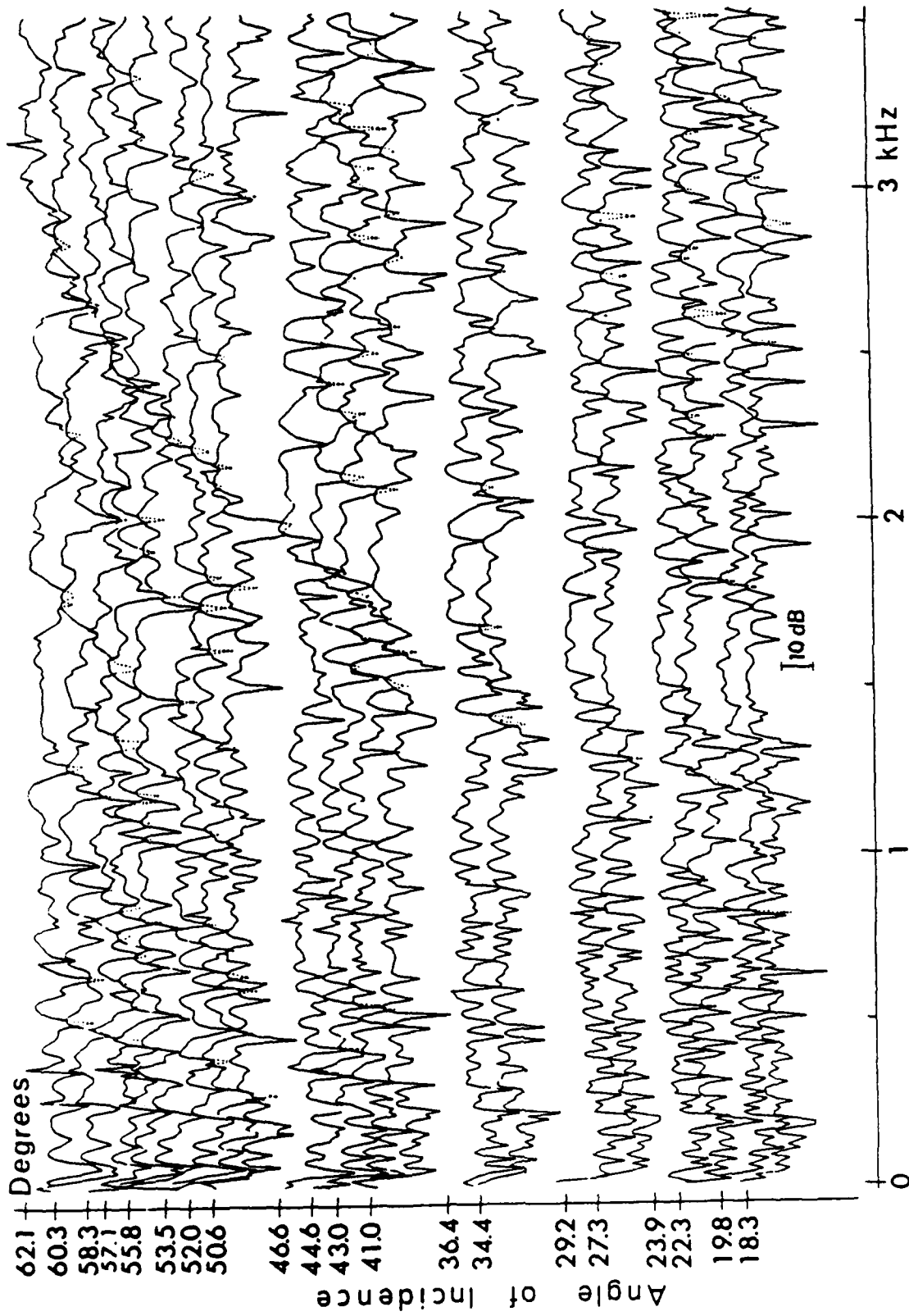
Figure 16-6. Loss Display for Different Angles of Incidence and Frequencies
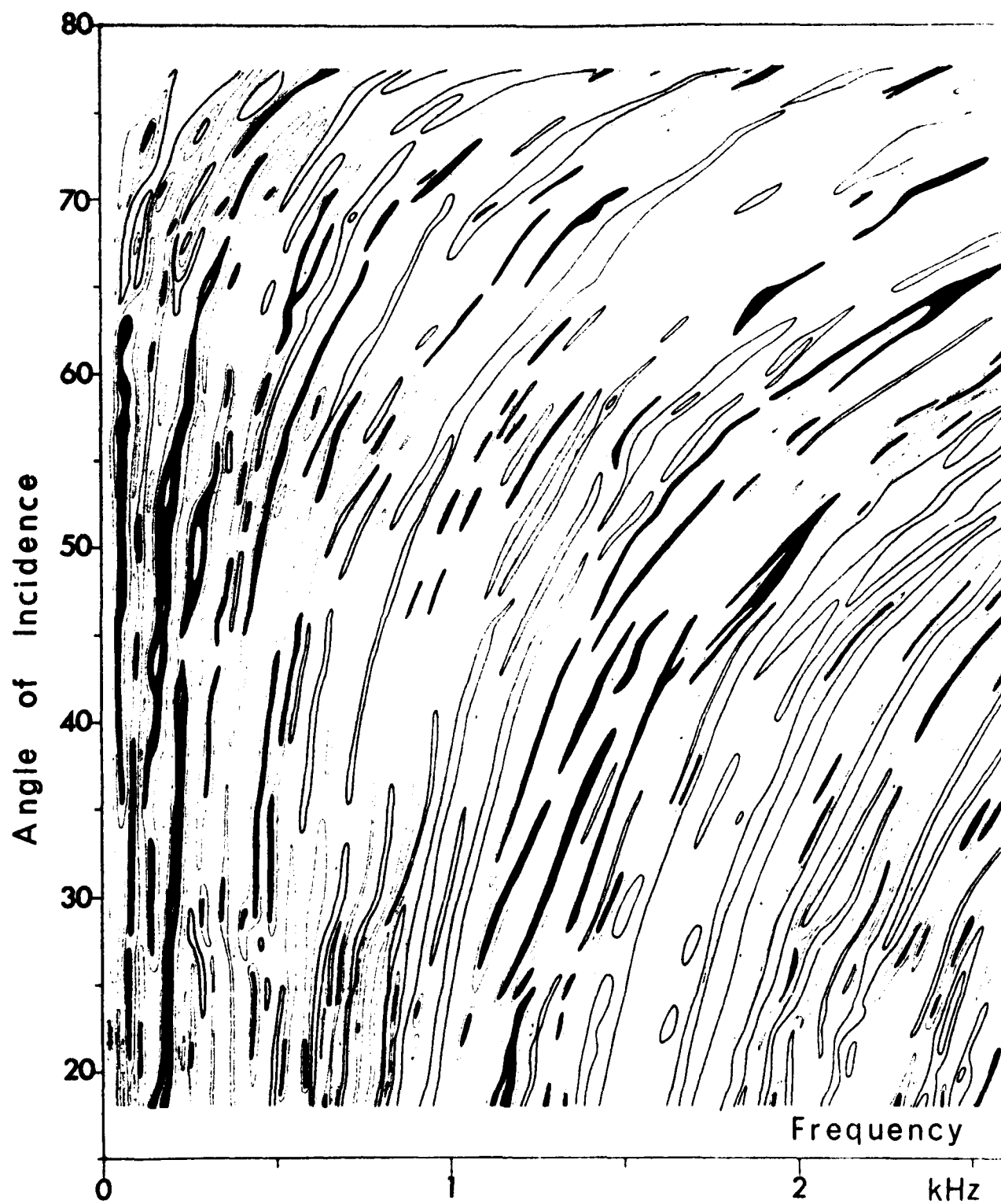
Figure 16-7.   Reflection Loss Contours in the Angle Frequency Plane
Black Contours: 5 dB, Green Contours: 10 dB,
Red Contours: 15 dB, Black Areas: over 20 dB

Bottom Reflections
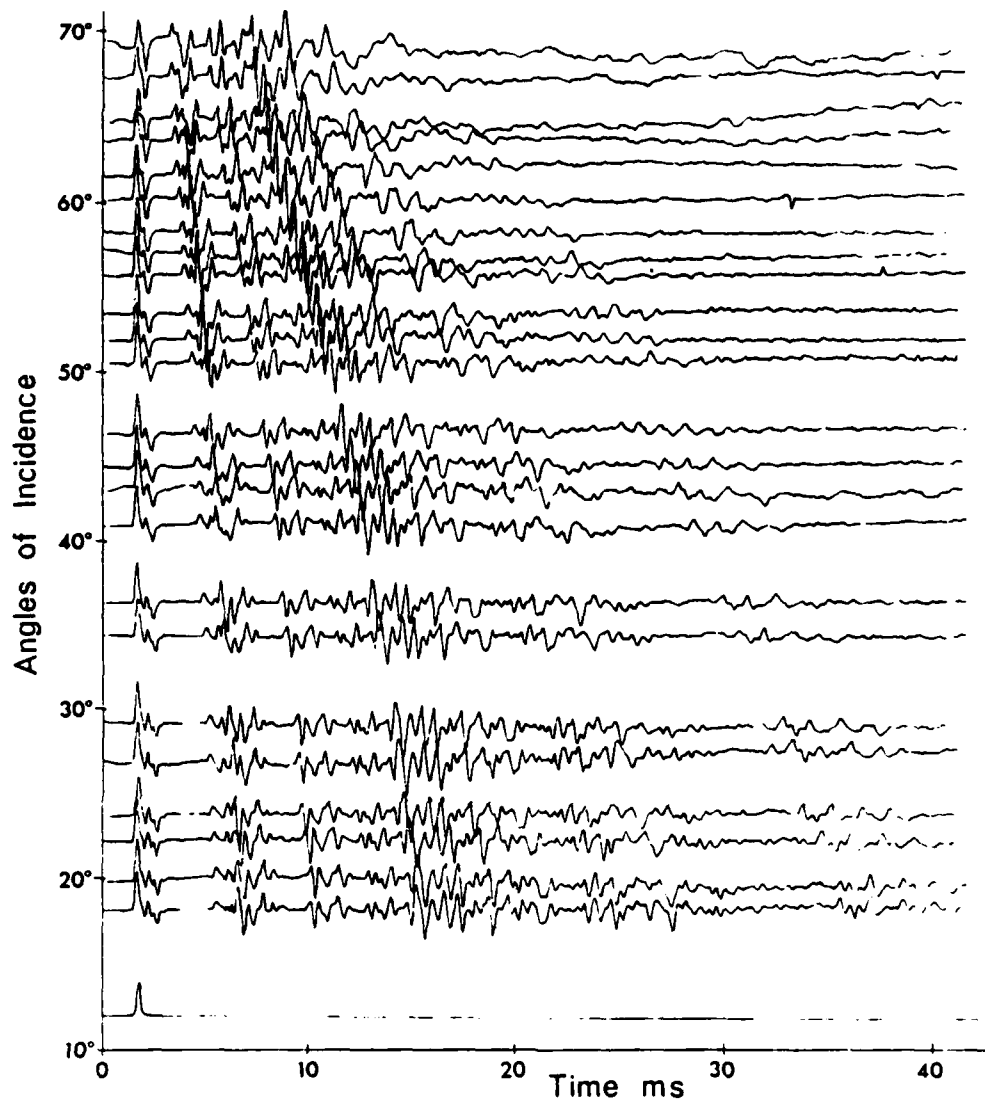
Figure 16-8. Impulse Response for Different Angles of Incidence

So at this stage we have a pretty good description of the bottom reflectivity. Let us now look at the actual bottom layering obtained from cores and echo soundings.

A total of six cores were taken along the isonified area and an inspection of them indicates that the layers are sloping down toward the west; therefore, four characteristic depths, A, B, C and D, were chosen to correspond to marked

141

changes in the layering. The depths are indicated in figure 16-9, which gives the acoustic parameters for the core taken only 1000 m from the reflecting area.
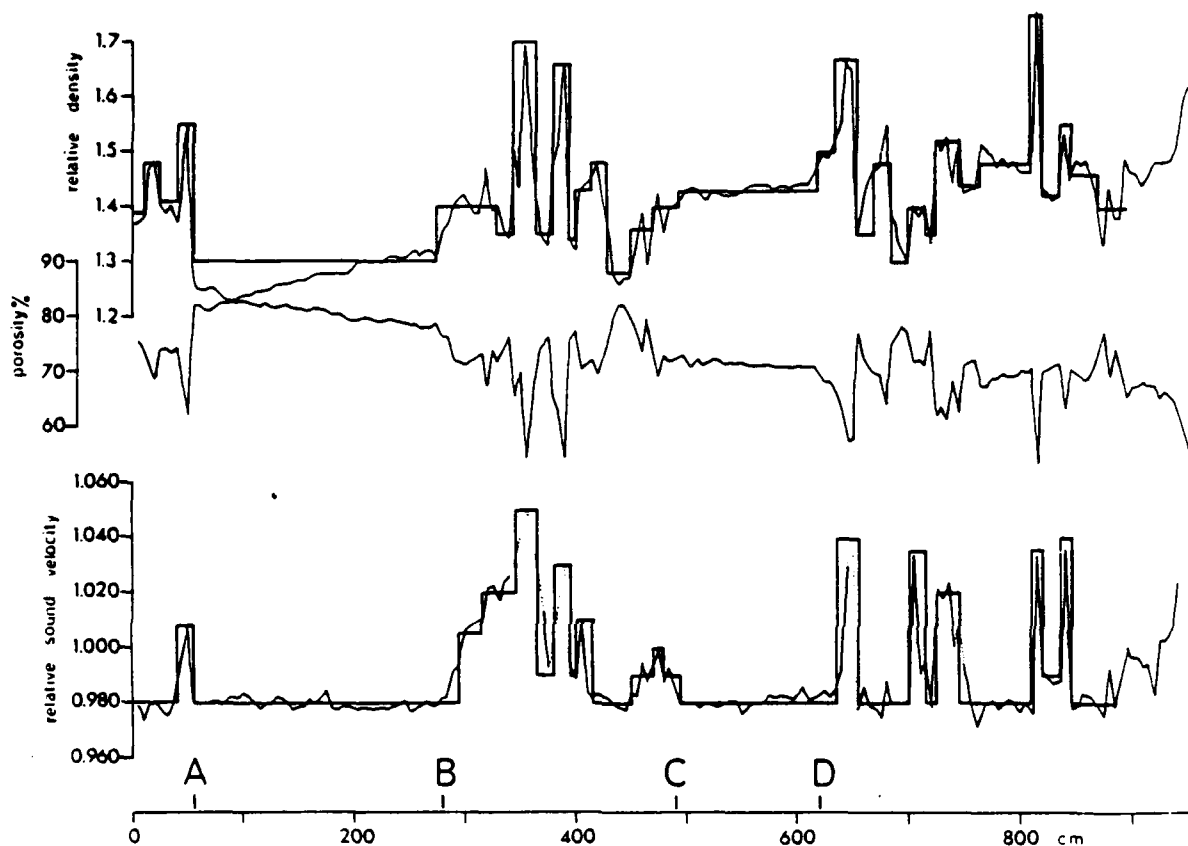
Figure 16-9. Core Parameters

Using these four characteristics from the six close cores, a multiple regression analysis was used to correct the layer depths to obtain the depths at the center of the isonified area and the geoacoustical model, also indicated on figure 16-9. The results, corrected for the sloping of the layers and the esti-mated values of shear wave velocity and attenuation, are given in table 16-1.

Table 16-1. Bottom Acoustic Constants for a 35-Layer Model

ALPHA	BETA	AA	AB	RHO	THICKNESS
1.000				1.00	
.980	.05	.1	.1	1.39	.15
.980	.05	.1	.1	1.47	.21
.980	.05	.1	.1	1.40	.21
1.000	.10	.2	.2	1.53	.21
.980	.05	.1	.1	1.30	2.75
.980	.05	.1	.1	1.40	.21
1.005	.10	.2	.2	1.40	.21
1.020	.10	.3	.3	1.40	.16
1.020	.10	.3	.3	1.35	.16
1.050	.15	.5	.5	1.70	.22
.990	.05	.1	.1	1.35	.16
1.030	.10	.3	.3	1.66	.16
.990	.05	.1	.1	1.34	.05
1.010	.10	.2	.2	1.43	.16
.980	.05	.1	.1	1.48	.16
.980	.05	.1	.1	1.28	.21
.990	.05	.1	.1	1.36	.22
1.000	.05	.1	.1	1.40	.10
.990	.05	.1	.1	1.40	.16
.980	.05	.1	.1	1.43	1.38
.980	.05	.1	.1	1.50	.15
1.040	.15	.3	.3	1.67	.22
.980	.05	.1	.1	1.35	.16
.980	.05	.1	.1	1.48	.17
.980	.05	.1	.1	1.30	.16
1.035	.10	.3	.3	1.40	.16
.980	.05	.1	.1	1.35	.11
1.020	.10	.3	.3	1.52	.22
.980	.05	.1	.1	1.44	.22
.980	.05	.1	.1	1.48	.50
1.035	.15	.3	.3	1.75	.11
.990	.10	.1	.1	1.42	.16
1.040	.20	.3	.3	1.55	.11
.980	.10	.1	.1	1.46	.28
.980	.10	.1	.1	1.40	

Based on the parameters for this model, computations are made to yield both the reflection loss and impulse response for angles of incidence of 0°, 18°, 36°, 54°, and 72°, using the techniques discussed in previous chapters. The results are shown on figures 16-10 and 16-11.

We see that the two reflection loss curves are very similar except for the lack of the high frequency components and higher losses (about 2 dB - 3 dB) for

the theoretical curve, due to the limited depth for which the computations are made. Also the characteristic low-loss intervals can easily be followed over the angles.

PREDICTED   MEASURED
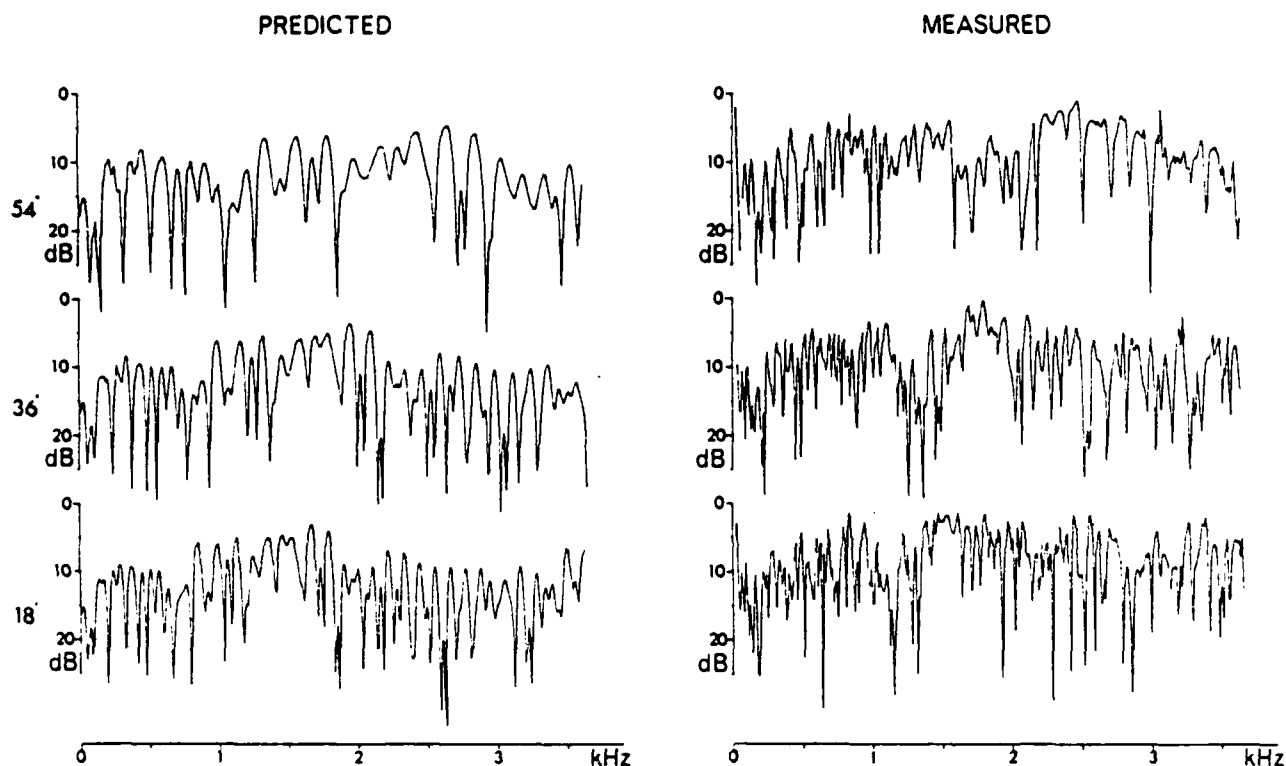
Figure 16-10. Theoretical and Experimental Losses

The theoretical impulse responses are computed using a Gaussian filter to enable a comparison with the experimental data. Within the first part of the signal (where we are representing the bottom with our model), we see that, considering the complicated sub-bottom structure, there is a good agreement between the two groups of curves, both with respect to time and amplitude and over all angles. Some peaks differ in magnitude, which is not surprising, considering that the velocity had to be estimated for some parts of the sand layers where the velocity is very difficult to measure.
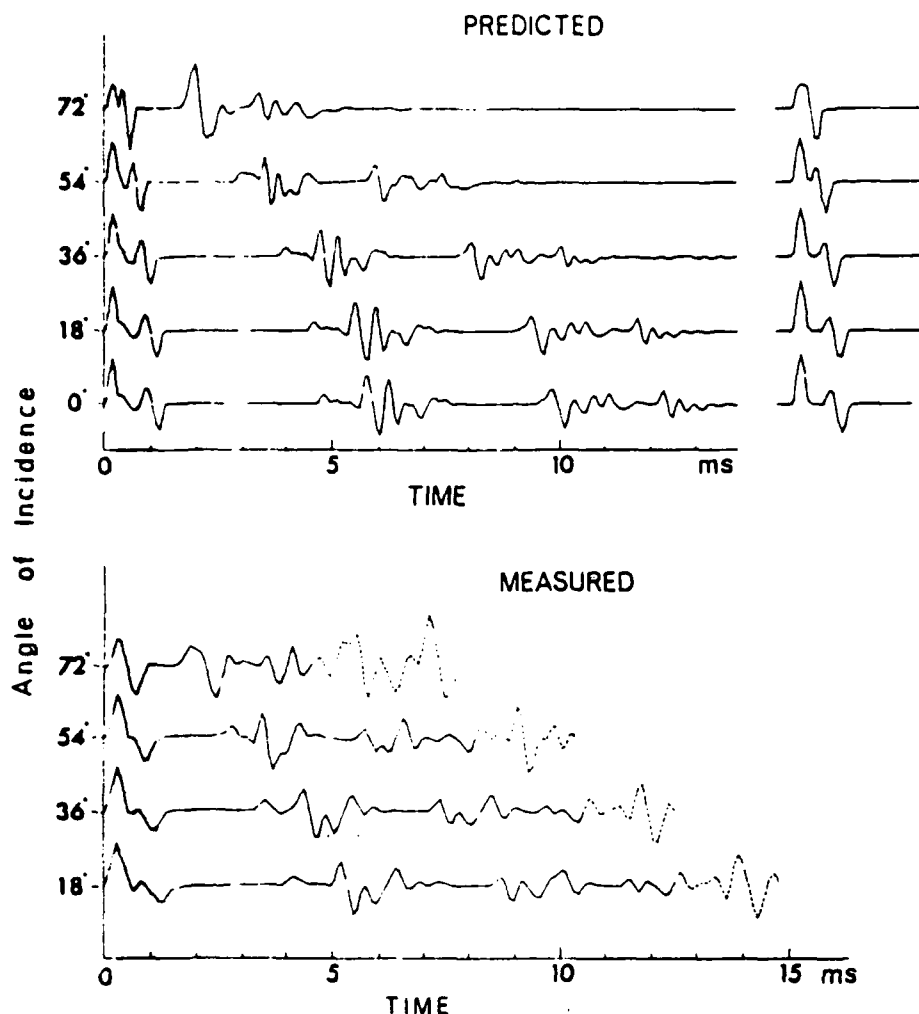
Figure 16-11. Theoretical and Experimental Impulse Response

Only for 72° does there seem to be some disagreement with respect to the first pulse. An inspection of the core data shows that this is probably due to a change in density a few centimeters below the bottom, a change that does not seem to correlate with either the velocity function or the layering. The upper right portion of figure 16-11 also shows the first pulse computed by ignoring this change. One now observes a better agreement between the curves for all angles of incidence.

Therefore, we can conclude that a comparison between the measured losses and impulse responses and the similar quantities computed from a 35-layer model based on actual core data shows good agreement over different angles of incidence with respect to frequency, time and amplitude.

ACKNOWLEDGEMENTS

REFERENCES

1. Twentieth Year Bibliography of SACLANTCEN Publications 1959 - 1979, SB-3, April 15, 1980.

2. SACLANTCEN Publications 1980 -> , SB-4, February 1982.

3. W.T. Thompson, "Transmission of Elastic Waves through a Stratified Solid Medium," Journal Appl. Phys., Vol 21, p. 89 (1950).

4. N.A. Haskell, "The Dispersion of Surface Waves on Multilayered Media," Bull. Seism. Soc. Am., Vol. 43, p. 17 (1953).

5. L.M. Brekhovskikh, "Waves in Layered Media," Academic Press (1980).

6. E.L. Hamilton, "Geoacoustic Modeling of the Sea Floor," J. Acoust. Soc. Am., Vol. 68, p. 1313 (1980).

APPENDIX A

IBM-PC ROUTINES FOR REFLECTIVITY CALCULATIONS

Several computer models have been developed for calculating the complex reflection coefficient for a general multilayered bottom. Unfortunately, the more complete models run only on large mainframe computers and the existing models available for microcomputers are usually too simple for serious studies. For certain applications such as on board ships and aircraft and in research environments where access to large computers is lacking or troublesome, it would be desirable to convert some of the large and general reflection loss programs to run on the popular IBM-PC type of personal computer.

Furthermore, it is often also very useful for the reader to have the opportunity to have an on-line facility to test the influence of the different bottom parameters on reflectivity. Therefore, an existing general multilayer model, which is based on the classical Thompson-Haskell transfer matrix technique and runs on a UNIVAC system, has been rewritten in MICROSOFT FORTRAN. This allows double precision of complex variables (in 16-byte length) to take advantage of the 8087 co-processor to run on IBM-PC family microcomputers. The program will not run without the 8087 co-processor.

The model calculates the reflection loss and the phase shift as a function of angle of incidence and frequency for a multilayered bottom, taking into account shear waves and attenuation. Additional procedures for disk file manipulations and display of results have also been developed.

The model is not an operational one and no special techniques, such as Knopoff's method, have been used to improve numerical accuracy for the matrix operations. Therefore, for higher frequencies and close to grazing, lack of accuracy and floating point overflow can occur. Some of these numerical prob-

lems have been countered by dropping deeper layers when the potentials in a layer were very small. Furthermore, no input data checking or error handling has been included. However, despite these shortcomings it was felt that such a PC facility could be useful and therefore is included.

The following will explain the different procedures and illustrate them by some examples.

THE PROGRAMS

The disk "REFLOSS" contains several programs. The two main ones are LAYER3.EXE and LAYER4.EXE which do the loss calculations: LAYER3 for a variable angle of incidence and fixed frequency, and LAYER4 for a variable frequency and fixed angle of incidence. PL2.BAS and PL4.BAS plot loss and phase as a function of angle of incidence and frequency, respectively. HELP.BAS is the program which displays the different options on the screen.

The input files contain the relative acoustical parameters for the layers and on this disk are usually named such as FLOOR1.DAT, although such nomenclature is not required as long as it is a valid file name with the DAT extension. The output files from LAYER3 and LAYER4 contain the reflection loss and phase shift as a function of either angle or frequency and are on the disk named, respectively, RESV18.DAT or RESF18.DAT, indicating whether the result is a function of angle or frequency.

The programs CREATE.BAT, LIST.BAT, and FILES.BAT are utility programs for editing or creating new input files for the acoustic parameters of the bottom, for listing a file, and for displaying all the FLOOR and RES files on a given disk. Programs PLOTV.BAT, PLOTF.BAT, HELP.BAT, LOSSV.BAT, and LOSSF.BAT are batch programs used to tie it all together.

HOW TO RUN THE PROGRAM

Before using the program, prepare a work disk in the following way. Format a disk using the /S option and copy onto it from your DOS disk the files BASICA.COM, GRAPHICS.COM and EDLIN.COM and finally all the files on the REFLOSS disk. Set aside the original and use the work disk.

To start, boot the disk by pressing simultaneously the following three keys <Ctrl> <Alt> and <Delete>, or from DOS type HELP. The following menu will appear:

HELP MENU

---CREATE 'FILENAME'.DAT---Use to create an layer input file for LOSSV/LOSSF.

---LIST 'FILENAME'.DAT---List a data file. Do not include extension.

--FILES--Lists all data files of the type FLOOR*.DAT and RES*.DAT on the disk.

---LOSSV---Calculates the reflection loss as function of angle of incidence.
---LOSSF---Calculates the reflection loss as function of frequency.

---PLOTV/PLOTF---Plots loss and phase as function of angle or frequency.

---QUIT---

ENTER YOUR SELECTION -->

As an example of how to use the CREATE option, we will consider a bottom consisting of two layers on top of a half-space with the characteristics shown below, where ALPHA is the compressional wave velocity, BETA the shear wave velocity, RHO the wet density, AA the compressional wave attenuation in dB/wavelength, AB the shear wave attenuation in dB/wavelength and DEP the layer thickness.

Water
```
    CW=1520 m/s                    RHO=1.03g/cc
```

```
1.  Layer
    ALPHA=1605m/s  BETA=530m/s  RHO=1.95g/cc  AA=0.4  AB=0.6  DEP=1.0m
         =1.055         =0.35        =1.89        =0.4    =0.6      =1.0
```

```
2.  Layer
    ALPHA=1720m/s  BETA=680m/s  RHO=2.11g/cc  AA=0.6  AB=0.8  DEP=1.5m
         =1.13          =0.45        =2.05        =0.6    =0.8      =1.5
```

```
Half-Space
    ALPHA=2840m/s  BETA=1670m/s  RHO=2.27g/cc  AA=1.0  AB=1.5
         =1.87          =1.1          =2.2         =1.0    =1.5
```

Since the programs LAYER3 and LAYER4 require the relative velocities and relative densities, these must be calculated and the results are shown on the line below the absolute values. Therefore, to create an input file named FLOOR12.DAT, using the above example, type CREATE FLOOR12 <ENTER>. The computer will display:

```
    A>EDLIN FLOOR12.DAT

    New file
    *
```

The program uses the DOS line editor EDLIN, but any preferred editor could be used. "I" starts the insert mode and ^C (same as <Ctrl> C) ends inserting. The "E" ends editing and saves the file to disk. For further details concerning the use of EDLIN to edit an existing file, consult the DOS manual. Enter I and insert values calculated in the example shown, creating the file on screen:

```
        *I

                1:*2
                2:*1.055 0.35 1.89 0.4 0.6 1.0
                3:*1.13 0.45 2.05 0.6 0.8 1.5
                4:*1.87 1.1 2.2 1.0 1.5
                5:*^C

        *E
```

where Line 1: is the number of layers.

To indicate the end of inserting the calculated values as shown above, type ^C and complete editing with E.

To calculate the reflection loss as a function of angle, type LOSSV from the HELP menu. For a hard copy of the results, ready the printer and type <Ctrl> P before <ENTER>. Do not forget to turn the printer off by typing <Ctrl> P again when the listing is terminated.

The program LAYER3.EXE will load and prompt:

LAYER CONSTANTS FROM DISK FILE (Y/N)?

If yes, the program will ask for the name of the file to use. Type the entire filename and extension. When the file data comes on the screen, verify by yes or no that it is the file you want to use. If yes, the program will ask for the minimum angle, the angle increment, and the maximum angle. Type in these angle values. The program will then ask for the frequency. Type in the frequency value.

At the termination of the LOSS program, you have the option to write the results to a disk file for subsequent processing such as for graphic displays. Choose a filename which relates to the input filename and shows the type of calculation (V or F). For the preceding example, the filename could be RESV12.DAT.

The program LOSSF, which calculates losses as a function of frequency, works in the same way as LOSSV.

To plot the angle-dependent results, type PLOTV. The program will ask for the name of the output file (RES*.DAT) which contains the results to be displayed. The filename should match the type of plot selected (V or F) and must include the .DAT extension. For example, to plot angle-dependent results from RESV18.DAT, which is in drive A, enter A:RESV18.DAT.

If the PC is connected to a DOT matrix printer which can produce graphics, print a hard copy of the results by pressing <Shift> <PrtSc>. To continue, press a key. Answer "Y" if you want to leave PLOTV or PLOTF and return to the HELP MENU. A similar procedure to plot results as a function of frequency is contained in PLOTF and works in the same way.

Figures A-1 and A-2 show the results for an 18-layer sample input file, FLOOR18.DAT, giving the reflection loss as a function of frequency and angle of incidence. The phase shift is omitted but could also have been included if required.

Sometimes it is convenient to see what data files of the format FLOOR*.DAT and RES*.DAT exist on a disk. Selecting FILES from system will display them on the monitor. Another facility available to display a data file is LIST, which when used, must contain the file name, but without the extension .DAT (e.g., LIST RESF4).

Figure A-3 shows the acoustical parameters for some FLOOR*.DAT files on the disk corresponding to different numbers of layers.

QUIT does what it says and clears the screen.
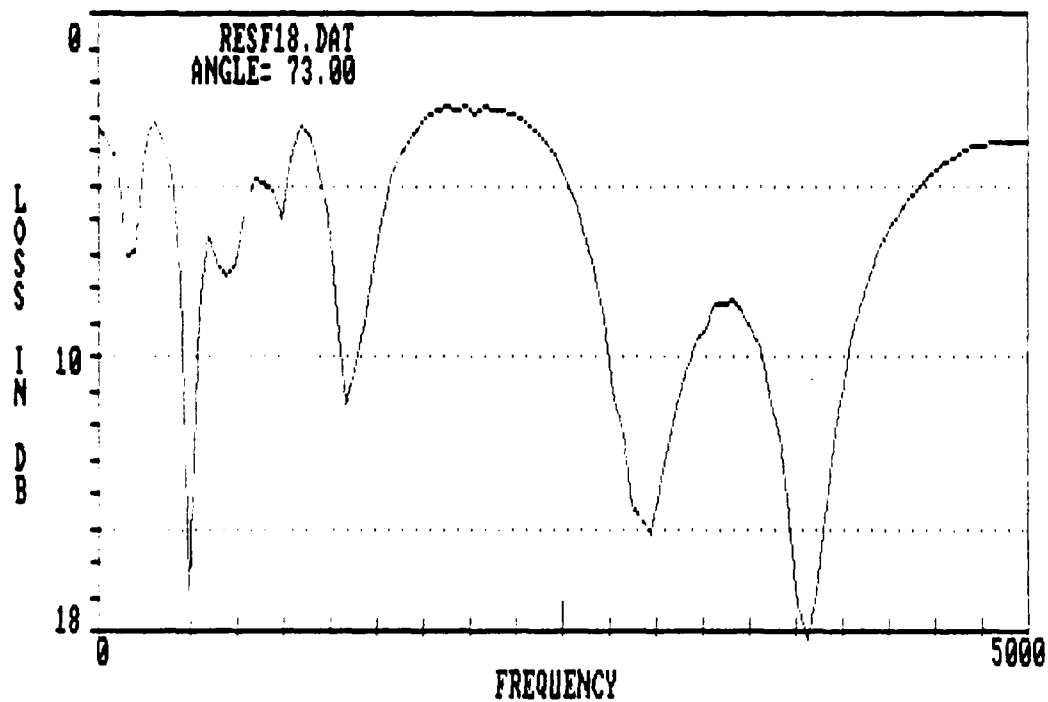
Figure A-1. Reflection Loss as Function of Frequency (18 layers)
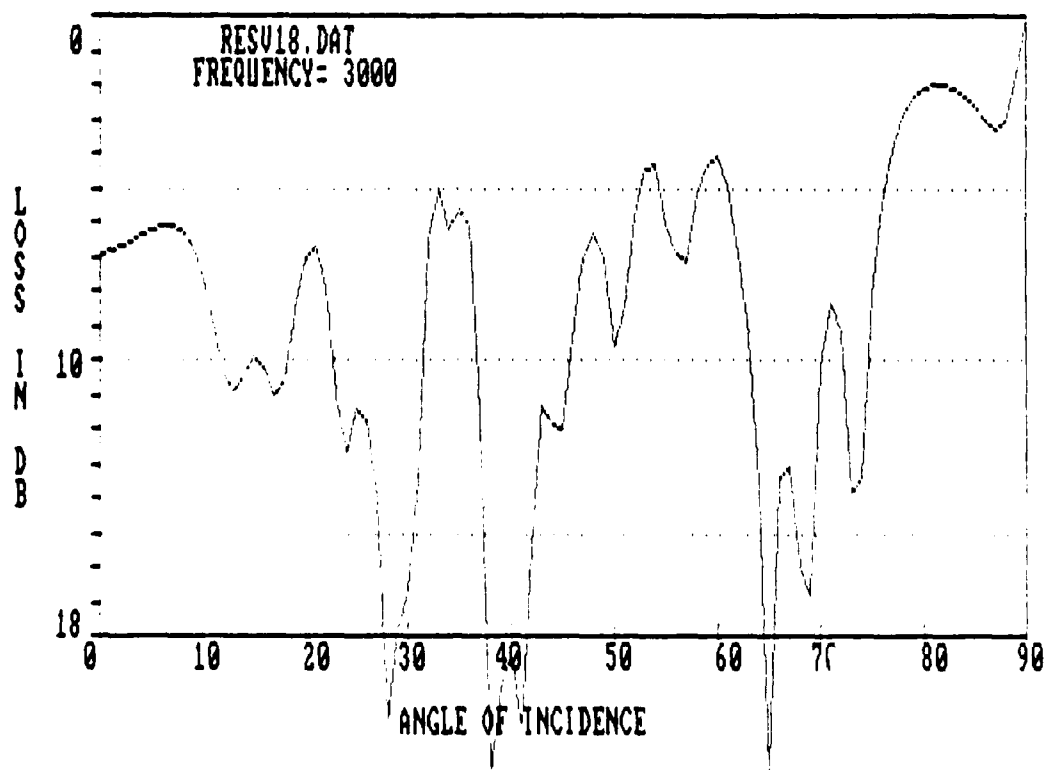
Figure A-2. Reflection Loss as Function of Angle (18 layers)

INPUT FILE NAME -- FLOOR0.DAT

ALPHA	BETA	RHO	AA	AB	DEPTH
1.130	.400	2.050	1.500	2.500	

INPUT FILE NAME -- FLOOR1.DAT

ALPHA	BETA	RHO	AA	AB	DEPTH
1.055	.260	1.890	1.000	1.500	1.000
1.130	.400	2.050	1.500	2.500	

INPUT FILE NAME -- FLOOR2.DAT

ALPHA	BETA	RHO	AA	AB	DEPTH
1.055	.350	1.890	.400	.600	1.000
1.130	.450	2.050	.600	.800	1.500
1.055	1.100	2.200	1.000	1.500	

INPUT FILE NAME -- FLOOR3.DAT

ALPHA	BETA	RHO	AA	AB	DEPTH
.970	.200	1.500	.100	.100	.500
1.040	.400	1.800	.400	.600	1.000
1.130	.600	2.050	.600	.900	1.500
1.870	1.100	2.200	1.200	1.500	

INPUT FILE NAME -- FLOOR4.DAT

ALPHA	BETA	RHO	AA	AB	DEPTH
.970	.010	1.300	.300	.600	1.000
1.050	.100	1.600	.500	.600	2.000
1.130	.300	1.900	.800	1.000	1.500
1.300	.400	2.050	1.200	1.200	.500
1.870	1.100	2.200	1.500	2.500	

Figure A-3. Content of FLOOR*.DAT Files

INPUT FILE NAME -- FLOOR18.DAT

ALPHA	BETA	RHO	AA	AB	DEPTH
.960	.050	1.350	.100	.100	1.000
.985	.050	1.400	.100	.100	.450
1.030	.100	1.700	.200	.200	.200
.960	.050	1.350	.100	.100	.600
1.030	.100	1.700	.500	.500	.250
.980	.050	1.400	.100	.100	.750
1.025	.100	1.650	.500	.500	.350
1.040	.150	1.750	.500	.500	.400
1.075	.200	1.900	.700	.700	.350
1.010	.100	1.550	.500	.500	.100
1.100	.250	1.950	1.000	1.000	.250
.975	.050	1.400	.200	.200	.750
.985	.100	1.500	.200	.200	.500
.975	.100	1.450	.200	.200	1.200
.965	.100	1.400	.200	.200	2.500
1.030	.150	1.750	.500	.500	.300
1.110	.300	2.100	1.000	1.000	.500
.980	.100	1.450	.200	.200	1.000
1.050	.200	1.800	.700	.700	

Figure A-3. Content of FLOOR*.DAT Files (Cont'd)

APPENDIX B

HALF-SPACE PARAMETERS

Information concerning the vertical incidence reflection coefficient and the intromission angle or critical angle can be used to quickly calculate the equivalent density and sound velocity at the water-sediment interface if we assume the bottom to act as a half-space.

From chapter 4 we have for the reflection coefficient this expression:

$$R = \frac{\rho \cos \theta - \sqrt{1/\alpha^2 - \sin^2 \theta}}{\rho \cos \theta + \sqrt{1/\alpha^2 - \sin^2 \theta}}$$

For vertical incidence, it is reduced to:

$$R_{vert} = \frac{\rho \alpha - 1}{\rho \alpha + 1}$$

or

$$\rho \alpha = \frac{1 + R_{vert}}{1 - R_{vert}}$$

The other information we have is from the reflection coefficient as a function of angle. If $\alpha < 1$, we have the intromission angle for which the loss is maximum and a sudden shift in phase from 0° to 180° with the angle being determined by:

$$\sin \theta_B = \sqrt{\frac{\rho^2 - 1/\alpha^2}{\rho^2 - 1}}$$

For $\alpha > 1$, we have a critical angle case where the angle is determined by:

$$\theta_{cr} = \arcsin \left(\frac{1}{\alpha}\right).$$

which enables us to calculate α and ρ if R_{vert} and θ_B or θ_{cr} are observed.

Figure B-1 shows the relationship between the vertical incidence loss $(-20 \cdot \log R)$, relative velocity, relative density and the characteristic angle involved. Also plotted is the curve corresponding to Woods equation, relating density, velocity and porosity. Because of the marked intersection between the

loss curves and the angle curves, a good determination of α and ρ is theoretically possible.

As an example, look at figure 4-2, which has a vertical loss $L = 16.5$ dB and $\theta_B = 76°$. Figure B-1 indicates that $\alpha = 0.975$ and $\rho = 1.38$ fully in agreement with the measured values.
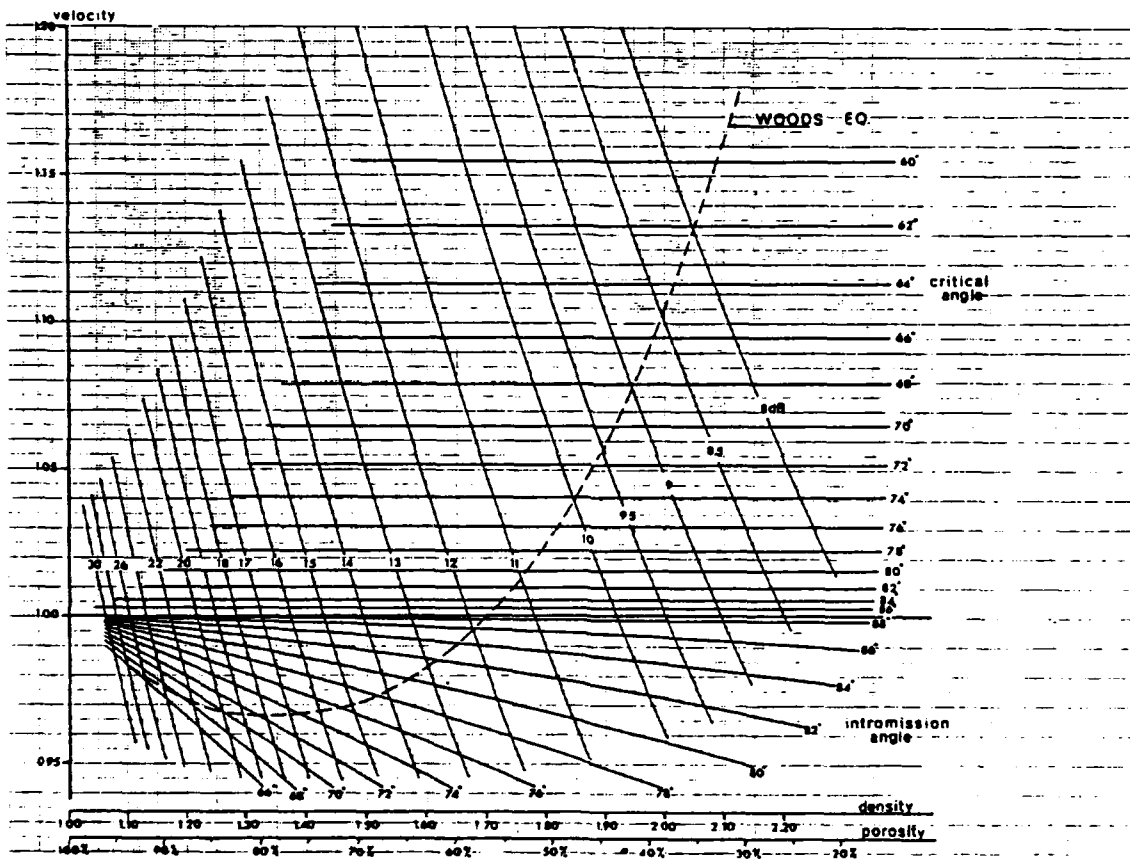

Figure B-1. Relationship between Vertical Incidence Loss, Relative Velocity Relative Density, and Characteristic Angle

APPENDIX C

ACOUSTIC CHARACTERISTICS OF THE SEA FLOOR

No doubt there is little purpose in trying to make predictions of the bottom reflectivity without some a priori knowledge of the layering of the bottom and its acoustical parameters. Several measurements have been made using echo soundings, seismic profiling, laboratory measurements on core and drilling samples, and most important of all in situ measurements. Also inverse methods such as using some knowledge about the bottom and then fitting modelled results to the experimental reflection or transmission loss data have yielded valuable information concerning certain bottom parameters. No attempt will be made to look into the physics of special models such as Biot, since it is the conviction of the author that such refinements are not yet required as long we are missing first order data for a large number of cases for practical requirements in ASW predictions.

Since our knowledge in this field is continually changing, this appendix will only summarize the range of the values of some of the acoustic parameters used for bottom reflection coefficient calculations. Readers are recommended to consult the substantial and recent documentation available.

Let us first list some of the most important geoacoustic values desirable to know:

a)   layer composition

b)   layer geometry including thickness and slope

c)   compressional wave (sound) velocity

d)   shear wave velocity

e)   density

f)   attenuation of compressional waves

g) attenuation of shear waves

h) for all of the above parameters, their dependence on depth.

The depth to which information is required depends on the frequency, the angle of incidence and the impedance of the layers. Usually we are talking of meters for frequencies in the kHz range down to hundreds of meters or even km for infra-sonics.

Unfortunately, the available amount of data are insufficient and probably will stay so, despite a continuing effort in this field caused by an increasing requirement for a better knowledge due to the development of future realistic acoustic prediction models. We are, therefore, faced with the reality of life where we are constrained to use what is available and, supported by marine geology, to make interpolations and extrapolations. We are also required to do some intelligent guessing in order to obtain the needed geoacoustical parameters for the bottom of interest. A large number of measurements on marine sediments have been made in the past years, and to the author's knowledge, the most complete critical review and compilation of these has been made by Edwin L. Hamilton, Naval Ocean Systems Center, San Diego. The following are extracts from his work supplemented by a number of data collected by the SACLANTCEN from measurements made on bottom cores.

It is not the purpose of this report to go into details on the values of the acoustic parameters to select for a given situation, but only to give some guidelines to the user. For more detailed information, one should consult the most recent relevant information available.

Before quoting possible values for the parameters of interest, let us return briefly to the concept of porosity as discussed in previous chapters. Porosity is an extremely practical parameter used to describe a marine sediment

and is defined as the ratio (often in percent) of the void volume to the solid volume of a sample. Furthermore, it can easily be measured by simple techniques using a precession scale and even a normal kitchen stove. Suppose the wet sediment sample weighed W gr before any loss of porous liquid and weighed D gr after being dried at a temperature below which chemical-bound water is not released. From the definition of the porosity n and some straightforward calculations, we arrive at the following expression for the sample's porosity:

$$n = \frac{\rho_s \cdot \dfrac{W - D}{W}}{1 + (\rho_s - 1) \cdot \dfrac{W - D}{W}}$$

with ρ_s as the solid bulk density under the assumption that no decomposition takes place and that the solid bulk density remains constant. In general, by using $\rho_s = 2.7$ good practical results are obtained.

Other important parameters exist to describe marine sediments such as grain size; however, these are not as easily measured as the porosity.

1) Compressional Wave Velocity and Density

Previously, we investigated the use of porosity as the parameter in the Woods equation to relate sound velocity and wet density under the assumption that one could regard a sediment as a two- or three-component mixture and to show that these assumptions are fairly valid. Figures C-1 and C-2 show the relative density and compressional (sound) velocity as a function of porosity based on approximately 15,000 and 8000 samples, respectively, from both deep sea and continental shelf cores.

Table C-1 lists some characteristic values of the ranges of porosity n, density and compressional wave velocity for different sediment types found in certain marine environments important for ASW.
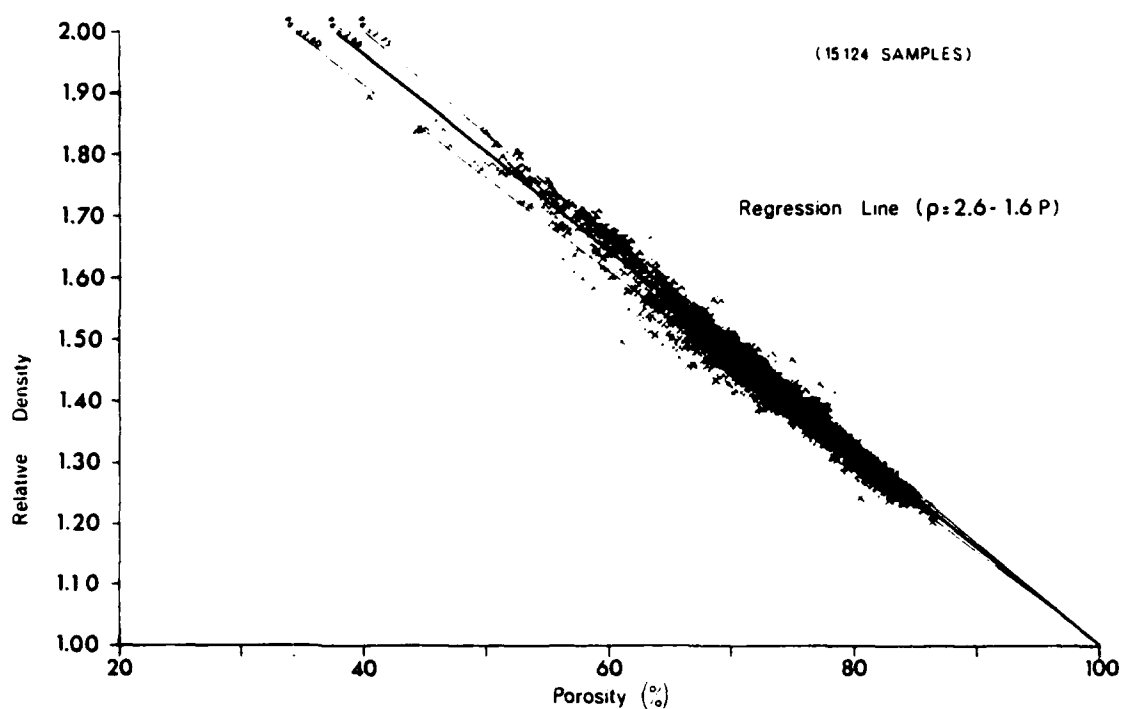
Figure C-1. Relationship Between Relative Density and Porosity
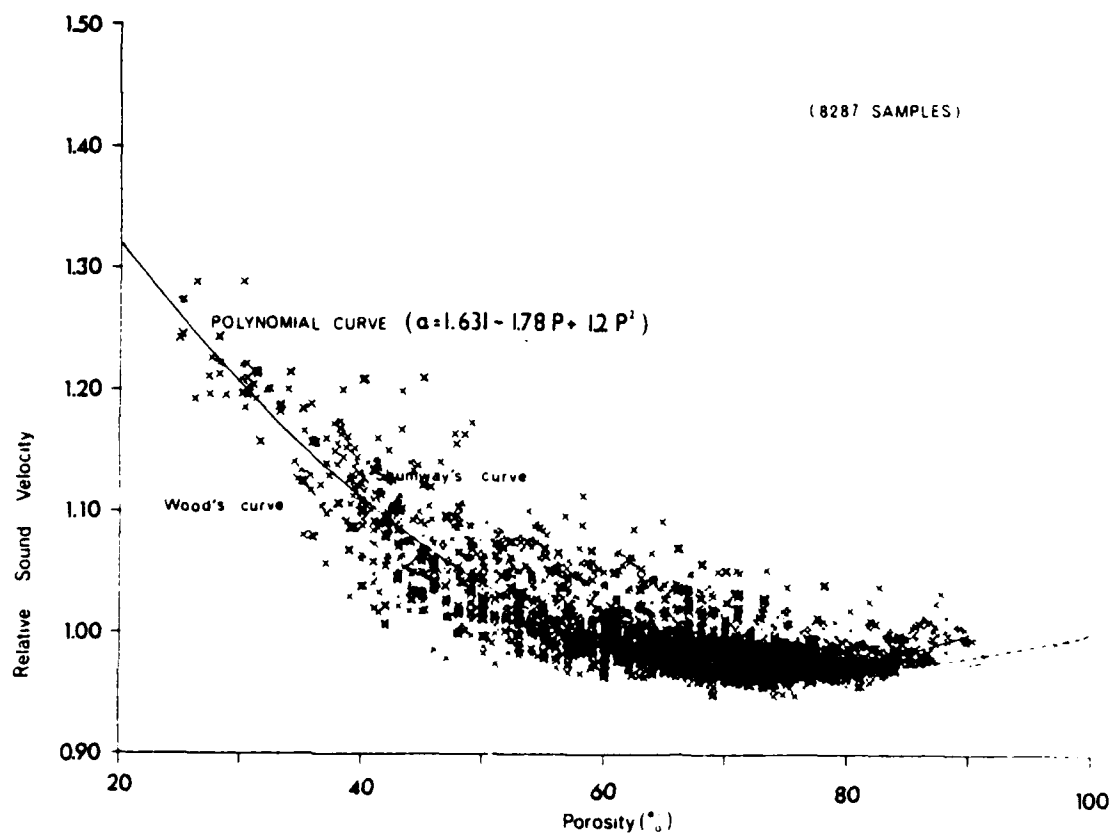

Figure C-2. Relationship between Relative Sound Velocity and Porosity

Table C-1. Characteristic Values for Density, Sound Velocity, and Porosity

for Various Sediment Types

Sediment Type	Relative Density	Relative Sound Vel.	Porosity %
Continental Shelf			
Sand			
Coarse	1.99	1.20	39
Fine	1.90	1.15	46
Very fine	1.82	1.12	50
Silty sand	1.74	1.08	55
Sandy silt	1.74	1.08	54
Silt	1.71	1.06	56
Sand-silt-clay	1.56	1.03	66
Clayey silt	1.46	1.01	72
Silty clay	1.39	0.994	76
Abyssal Plain			
Clayey silt	1.43	0.999	74
Silty clay	1.32	0.991	81
Clay	1.33	0.983	80
Abyssal Hills			
Clayey silt	1.32	0.995	81
Silty clay	1.32	0.986	81
Clay	1.39	0.976	78
Sand-silt-clay	1.41	1.02	75
Silt-clay	1.38	1.00	77
Rocks			
Sedimen. rock	2.55	2.45	
Basalt	2.60	3.47	

In almost all cases, measurements in nature have shown a distinct increase in the compressional wave velocity with depth, with the result that, at smaller grazing angles and low frequencies, the sound energy penetrating into the bottom is not only being reflected but also refracted back into the water column. Examples of such refracted waves are observable in figures 14-6 and 14-9 in chapter 14.

This gradient could be taken into account when preparing input data to the two computer models covered in appendix A by creating a set of thin layers simulating a velocity gradient if required. Good values to use for the gradient of the compressional waves in the upper layers range from 1.1 to 1.5 S^{-1}.

2) Shear Wave Velocity

If our knowledge of compressional wave velocities is somewhat limited, unfortunately much less is available concerning shear wave velocities. Perhaps for two reasons: One is that historically in ASW it was electronic engineers or scientists who were the pioneers. They were little acquainted with the existence and importance of shear waves from the theory of elasticity of solids. More important is the fact that it is much more difficult to measure shear wave characteristics than compressional wave characteristics for several reasons. One problem is to ensure proper coupling between the measuring probes and the sediment. Another is the fact that shear in a sediment to a certain extent is transmitted through its chemical bounds which are easily destroyed either by the sediment sampling or by the insertion of the measuring sensors in the samples. This is very unfortunate, since for consolidated sediments, shear waves can be extremely important because of the role they play in carrying converted incident compressional energy away from the water-sediment boundary and as such are subject to a higher attenuation and may be converted into interface waves

(Scholte type). All these factors result in a softening effect and thereby a reduction of the bottom reflectivity.

Studies have shown that shear wave velocities can be related to compressional waves velocities, but unfortunately not in the same fixed ratio. For practical reasons, three intervals of relative compressional wave velocities α with their associated relative shear wave velocity β dependence have been identified. Let us look at those cases:

a) $0.989 < \alpha < 1.017$
    $\beta = 3.884 \cdot \alpha - 3.765$

b) $1.017 < \alpha < 1.079$
    $\beta = 1.137 \cdot \alpha - 0.971$

c) $1.079 < \alpha < 1.406$
    $\beta = 0.648 - 1.136 \cdot \alpha + 0.719 \cdot \alpha^2$

To obtain an idea of the relative shear wave velocity as a function of depth below the water-sediment interface, the following expression for fine sand can be used:

$$\beta = 0.084 \times D^{0.28}$$

where D is depth of the sediment in meters.

3) Attenuation of Compressional Waves

A large number of measurements of the attenuation of compressional waves in marine sediments have been made covering a frequency range from 10 Hz to 1 MHz. The results show that the attenuation in dB/m varies remarkably well with the first power of frequency, which again corresponds to a constant dB per wavelength as used in the previous calculations. However, in order to be consistent

with attenuation values reported in the literature, we will use for the attenuation the expression:

$$AA = k_c \cdot f$$

where f is in kHz, AA in dB/m and k_c the attenuation coefficient. Also here, as for the densities and compressional wave velocities, we will use porosity as the independent variable. Figure C-3 shows the result of a large number of measurements indicating a maximum attenuation around a porosity of 50 to 55 percent corresponding to silty sand. For solid rocks like limestone or basalt, k is in the order of 0.02 to 0.03.
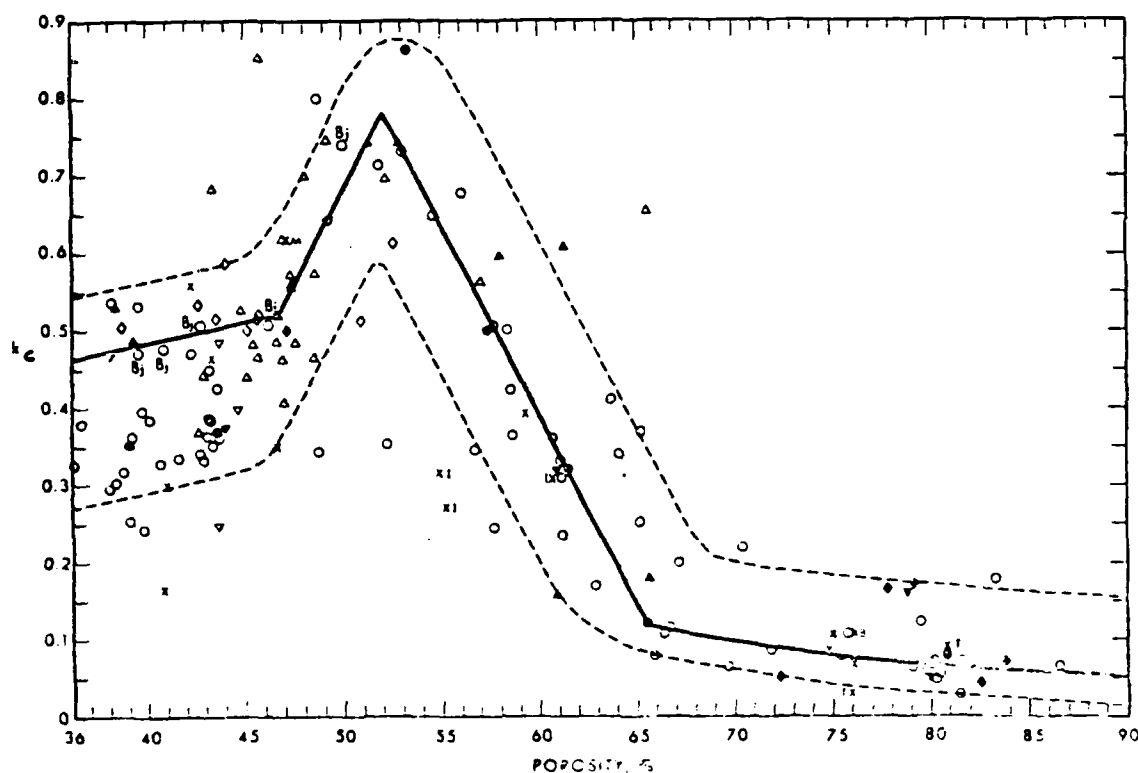

Figure C-3.   Attenuation Coefficients for Compressional Waves
as a Function of Porosity

Very little data are available to determine the depth dependence on the compressional wave attenuation, but some data indicates only a little effect in

the first meters of the sediments. For deeper sediments consisting of silt-clays, the data seems to show an increase with depth, whereas for sand-silt it appears that the attenuation decreases with about the -1/6 power of the overburden pressure.

4) Attenuation of Shear Waves

Similar to measurements for the compressional waves, measurements of the attenuation of shear waves indicate a linear relationship. Again, we can use the expression:

$$AB = k_c \cdot f$$

where f is the frequency in kHz, AB in dB/m, and k_c the attenuation coefficient. Table C-2 gives examples of values for k for different materials.

Table C-2. Characteristic Values for the Attenuation Coefficient

for Various Sediment Types

Material	k_c
Diluvial sand	13.20
Diluvial sand and clay	4.80
Alluvial silt	13.40
Mud (silt-clay)	17.30
Water-saturated clay	15.20
Tertiary mudstone	10.10
Solenhofen limestone	0.04
Chalk	0.10
Basalt	0.07

Concerning the depth dependence of the shear wave attenuation, it can be assumed that it varies proportionally with the compressional wave attenuation.

The above values for the geoacoustical parameters in marine sediments are only given to show within which values they are to be expected in nature. For the purpose of constructing a proper geoacoustical model, readers are referred to the large and detailed amount of information available in the open literature.

END

DATE

FILMED

DTIC

11 - 88